

POLITECNICO DI TORINO

M.Sc. in Mechatronic Engineering

Master Thesis

**Modeling and identification of
wheel-soil interaction for precision
agriculture robotics**



Supervisors

Prof. Alessandro Rizzo

Ing. Antonio Petitti

Candidate

Vito VATTIATA

A.Y. 2019-2020

Summary

This thesis has been developed in collaboration with STIIMA-CNR (Sistemi e Tecnologie Industriali Intelligenti per il Manufaturiero Avanzato - Consiglio Nazionale delle Ricerche) located in Bari.

The adoption of intelligent machines in agriculture has been steadily growing. Intelligent tractors, and specifically agricultural Wheeled Mobile Robots (WMR) are gaining momentum as standard tools to increase productivity and efficiency in the fields.

One of the main limitations to the effective use of WMR in agricultural application is their poor performance in terms of traction control, considering also the rough nature of the involved terrains. In this vein, the identification of the terrain characteristics is key to develop the next generation of intelligent WMRs.

Agricultural terrains have disparate physical characteristics, hence terrain classification using on-board sensors can provide important information regarding tractive efficiency, traction control, traversability prediction and performance optimization.

Therefore, the on-line identification of soil parameters of unknown terrains on which the vehicle is moving can be crucial for controlling the vehicle navigation.

Against this background, a method able to identify soil parameters that may affect traction of vehicle is developed in this thesis. The identification algorithm is based on a decoupled analysis of integral equations of forces and torques acting on the wheel's robot. This allows to recognize terrain parameters useful for predictive traction control systems.

The thesis revolves around the development of a wheel-soil interaction model based on terramechanics theory, which is able to make up for those investigations where field experimental data are not available.

Thus, the first step is to develop a model able to address the dynamic motion behavior of a WMR on deformable soils. To deal with the motion dynamics on soft terrains, suitable models for both longitudinal and lateral direction are analyzed.

A rigid wheel moving on a deformable soil causes soil displacement beneath the wheel, this is due to the normal and shear stress distributions along the contact patch area. By integrating these stresses along with the contact angle between wheel and soil, the forces and torques acting on the wheel can be calculated from

the proposed model.

However, the equations used to calculate the distribution of stresses beneath a wheel are highly non-linear and complex, therefore integral equations cannot be easily solved. Thus, a simplification of the wheel-soil interaction model is performed by means of a quadratic approximation.

Considering that the wheel is traveling on a deformable soil, a wheel portion sinks into the terrain during motion. Thus, a wheel sinkage estimator is also developed by means of numerical iteration method. Wheel-soil interaction model with wheel sinkage estimator form a complete terramechanics model able to calculate the forces and torques.

Then, the motion dynamics behavior of the robot is simulated by means of multibody system dynamics.

Once simulations from the model dynamics are obtained, the soil parameters identification method is applied. The algorithm provides satisfactory performance and the computational time for fitting drawbar pull, vertical force and torque is very short, mean value around 50-100 ms.

Finally, it can be concluded that this method is suitable for on-line identification of unknown agricultural soil parameters.

Future work will deal with optimal control algorithms based on the online recognition of soil parameters.

Acknowledgements

I would first like to thank my supervisor, Prof. Alessandro Rizzo, who has always been available to my request and has shown attention to my work.

I would like to extend my sincere thanks to my supervisor in Bari, Antonio Petitti, for really helping me with very valuable advice during the development of the model and algorithms and with the writing of the thesis.

I also thank Fabio Vulpi for giving me useful tips regarding to Simulink software.

My university experience would not have been so beautiful and full of experiences without the vital aid of my family who always encouraged me and also helped me financially.

I am grateful to my girlfriend, Valentina, she has been always present in the good moments, but especially in the bad ones.

Special thanks to Luigi Sante, he has been always ready to help me out with practical suggestions when I have been in trouble.

Each person I met individually has contributed in some way to my personal growth and I am grateful for that. I also thank the people I have not met, but who still inspired me with their ideas and stories.

Contents

List of Tables	8
List of Figures	9
Nomenclature	11
1 Introduction	14
1.1 Background	14
1.2 Purpose and Approach	16
1.3 Literature review	16
1.4 Outline	18
2 Wheel-soil interaction model	19
2.1 Introduction	19
2.1.1 Assumptions	20
2.2 Contact geometry and kinematic analysis	21
2.2.1 Wheel coordinate system	21
2.2.2 Slip ratio and slip angle	22
2.2.3 Wheel sinkage	23
2.2.4 Wheel-soil contact geometry	27
2.3 Stress distribution analysis	29
2.3.1 Normal stress	29
2.3.2 Shear stress	29
2.4 Forces/torques analysis	32
2.4.1 Drawbar pull (F_x)	33
2.4.2 Side force (F_s)	33
2.4.3 Vertical force (F_z)	36
2.4.4 Roll moment (M_x)	36
2.4.5 Resistance torque (M_y)	36
2.4.6 Yaw moment (M_z)	37
2.5 Stress simplification	37
2.5.1 Closed-form solution	39

2.6	Terramechanics-based model	40
2.6.1	Estimation of entry angle	40
2.6.2	Drawbar pull results	42
2.6.3	Side force results	42
2.6.4	Other forces/torques estimation	43
3	Vehicle Dynamics	56
3.1	Introduction	56
3.2	Target vehicle	56
3.3	Wheeled-mobile robot dynamics model	57
3.3.1	Simplified vehicle model	58
3.3.2	Simulation procedure	59
3.3.3	Simulation results	61
4	Soil parameters identification	68
4.1	Introduction	68
4.2	Soil parameters analysis	69
4.2.1	Discussion and results	70
4.3	Identification algorithm	73
4.3.1	Stress simplification	75
4.3.2	Decoupling of equations	76
4.3.3	Identification method	77
4.3.4	Implementation of identification algorithm	78
5	Identification results	80
5.1	Introduction	80
5.2	Fitting graphs and errors	81
6	Conclusion	91
	Bibliography	92

List of Tables

2.1	Soil parameters for different soil types [21]	32
2.2	Smooth wheel parameters	32
2.3	Operating conditions parameters	33
2.4	Root-mean-square error (RMSE)	39
2.5	Mean-absolute error (MAE)	39
2.6	Parameters used for simulation	41
2.7	F_z mean errors	43
4.1	Soil parameter variations for model sensitivity analysis	70
5.1	Parameters of wheels	80
5.2	Parameters used for simulation	81
5.3	Identified soil parameters for wheel-A	82
5.4	Identified soil parameters for wheel-B	83
5.5	Squared norm of the residual for wheel-A	84
5.6	Squared norm of the residual for wheel-B	84

List of Figures

1.1	Example of intelligent tractor [1].	14
1.2	People employed in agriculture in the US, in millions [12].	15
2.1	Wheel-soil interaction model combined with vehicle dynamics model	20
2.2	Wheel coordinate system [15]	21
2.3	Side view and top view of the wheel [15]	22
2.4	Static and slip sinkages of a wheel [5]	23
2.5	Stress distribution and wheel sinkage under static and traversing wheels	25
2.6	Static wheel sinkage estimated in three different kinds of soil. (W ranged from 25 N to 98 N; $r = 92$ mm, $b = 107$ mm)	26
2.7	Diagram of wheel-soil interaction mechanics (cylindrical surface) [18]	27
2.8	Normal and shear stresses along the wheel-soil contact area [18] . .	30
2.9	Shear stress-deformation curve [15]	31
2.10	Mohr-Coulomb failure criterion [29]	31
2.12	Forces and torques by integrating the stresses along the wheel-soil contact area [18]	33
2.13	Side force model	34
2.14	Identify the side surface contribution	35
2.11	Stress distribution for smooth wheel traveling on different soil types	45
2.15	Bulldozing resistance vs wheel sinkage for three different soil types ($r=92$ mm; $b=107$ mm)	46
2.16	Quadratic approximation of stresses along the contact area	47
2.17	Flowchart of entry angle estimation algorithm	48
2.18	Computed entry angle vs slip ratio	49
2.19	Drawbar pull along the slip ratio for three different soil	50
2.20	Sandy loam: lateral force vs slip ratio simulated at different slip angles	51
2.21	Dry sand: lateral force vs slip ratio simulated at different slip angles	52
2.22	Clayey soil: lateral force vs slip ratio simulated at different slip angles	53
2.23	Results of vertical force for sandy loam terrain	54
2.24	Resistance torque results for sandy loam terrain	54
2.25	Roll moment results for sandy loam terrain	54

2.26	Sandy loam: yaw moment vs slip ratio simulated at different slip angles	55
3.1	Simplified CAD model of a 4WD/4WS mobile robot	57
3.2	Model dynamics of a mobile robot [15]	58
3.3	Simplified model of wheeled-mobile robot [18]	59
3.4	SimMechanics vehicle dynamics model	60
3.5	Terramechanics-based model	61
3.6	Motion simulation of a simplified vehicle model during steering maneuvers (SimMechanics toolbox)	62
3.7	Vehicle position in straight line motion scenario	63
3.8	Vehicle velocities in straight line motion scenario	63
3.9	Wheel slip ratio in straight line motion scenario	64
3.10	Input steering angles applied on each wheel in steering motion scenario	64
3.11	Vehicle position and orientation in steering motion scenario	65
3.12	Wheel's longitudinal velocities in steering motion scenario	66
3.13	Wheel's lateral velocities in steering motion scenario	66
3.14	Wheel slip ratios in steering motion scenario	67
3.15	Vehicle's velocities in steering motion scenario	67
4.1	Model sensitivity to sinkage exponent (n)	70
4.2	Model sensitivity to cohesion stress (c)	71
4.3	Model sensitivity to internal friction angle (ϕ)	72
4.4	Model sensitivity to cohesive modulus (k_c)	72
4.5	Model sensitivity to frictional modulus (K)	73
4.6	Model sensitivity to shear modulus (k_ϕ)	73
4.7	Diagram of coupled wheel-soil interaction model	74
4.8	Identification diagram of a_0, a_1	77
4.9	Identification diagram of K_s, n_0, n_1	78
4.10	Identification diagram of K_s, n_0, n_1	78
5.1	Fitting graphs for wheel-A on sandy loam	85
5.2	Fitting graphs for wheel-B on sandy loam	86
5.3	Fitting graphs for wheel-A on dry sand	87
5.4	Fitting graphs for wheel-B on dry sand	88
5.5	Fitting graphs for wheel-A on clayey soil	89
5.6	Fitting graphs for wheel-B on clayey soil	90

Nomenclature

Abbreviations

DEM Discrete element method

FEM Finite element method

MAE Mean Absolute Error

MBS Multibody system-based approach

RMSE Root Mean Squared Error

TBM Terramechanics-based model

UGV Unmanned ground vehicle

WMR Wheeled Mobile Robot

Subscripts

f, r front, rear region

t, l longitudinal, lateral direction

Symbols

β Slip angle (deg)

γ Specific weight of soil (kN/m³)

ω Angular velocity of the wheel (rad/s)

ϕ Internal friction angle of soil (deg)

σ Normal stress acting on wheel (kPa)

τ Shear stress acting on the wheel (kPa)

τ_{max}	Maximum value of the shear stress ($\tau_{max} = c + \sigma(\theta) \tan \phi$) (kPa)
θ	Generic contact angle of the wheel (deg)
θ_e	Equivalent front region contact angle for points in the rear contact region (deg)
θ_f	Contact entry angle of the wheel (deg)
θ_m	Angle corresponding to the maximum normal stress (deg)
θ_r	Contact exit angle of the wheel (deg)
θ_s	Static contact angle of the wheel (deg)
θ_{fm}	Front medium angle (deg)
θ_{rm}	Rear medium angle (deg)
\tilde{p}	Stress approximation
\mathbf{v}	Mean velocity vector of the wheel (m/s)
a_0, a_1	Coefficients for calculating maximum normal stress angle ($\theta_m = (a_0 + a_1 s) \theta_f$) (dimensionless)
c	Cohesion stress of soil (kPa)
d	Distance between the wheel center and the flat terrain level ($d = r - h$) (m)
F_b	Bulldozing resistance (Force due to the normal pressure acting on the side surface of the wheel during steering) (N)
F_s	Side force ($F_s = F_y + F_b$) (N)
F_x	Drawbar pull (Net force acting on the longitudinal direction of the wheel) (N)
F_y	Lateral force (Force due to lateral shear stress) (N)
F_z	Vertical force acting on the wheel (N)
h_d	Dynamic sinkage of the wheel (m)
h_f	Total wheel sinkage in the front region of the wheel ($h_f = h_s + h_d$) (m)
h_r	Rut recovery (m)
h_s	Static sinkage of the wheel (m)

j	Magnitude of shear deformation (m)
j_l	lateral shear deformation of soil under a rigid wheel (m)
j_t	Tangential shear deformation of soil under a rigid wheel (m)
j_{max}	Shear deformation limit for smooth wheels (m)
K	Shear deformation modulus of soil (m)
k_c	Cohesive modulus of soil (kN/m^{n+1})
K_s	Equivalent lumped pressure-sinkage coefficient of soil ($K_s = (k_c/b+k_\phi)(\text{kN/m}^{n+2})$)
k_ϕ	Frictional modulus of soil (kN/m^{n+2})
M_x	Roll moment acting on the wheel (Nm)
M_y	Resistance torque acting on the wheel (Nm)
M_z	Yaw moment acting on the wheel (Nm)
N	Linear sinkage exponent of soil that reflects slip sinkage phenomenon, ($N = n_0 + n_1 s$) (dimensionless)
n	Sinkage exponent of soil (dimensionless)
n_0, n_1	Coefficients for calculating sinkage exponent N (dimensionless)
n_{tot}	Number of samples
r	Wheel radius (m)
s	Slip ratio of a wheel (dimensionless)
v_x	Longitudinal velocity of the wheel (m/s)
v_y	Lateral velocity of wheel (m/s)
v_{jl}	Lateral shear rate during soil deformation under rigid wheel (m/s)
v_{jn}	Compression speed during soil compaction under rigid wheel (m/s)
v_{jt}	Tangential shear rate during soil deformation under rigid wheel (m/s)
W	Normal wheel load (N)

Chapter 1

Introduction

1.1 Background

Intelligent machines (Fig. 1.1) have been developed for applications in various sectors: planet explorations, military purposes, payload transports, service operations, agriculture, and so on. In the agricultural sector, during the last years, the application of intelligent machines is growing up. This is due principally to the problem of labor shortage, especially the skilled ones, and to the need of improving cultivation monitoring. In fact, with regard to world population explosion, supplying such a



Figure 1.1: Example of intelligent tractor [1].

large number of people with food required an expansion of the current agricultural land and an increase in farm productivity, both of these options required more labor in the agricultural sector [25]. However, due to aging population, job preference and rural urban migration, agricultural labor force is decreasing annually as shown in Fig. 1.2. Thereafter, this problem addressed the researchers to focus on automated tractors for agricultural operations. In agriculture there are several

fields of operations that an intelligent tractor may perform. For example, they can be used for automated harvesting operations, pesticide spraying, fruit classification and plant diseases detection. The benefits derived from those applications are:

- a substantial reduction in downtime
- increased speed of operations
- decreased risk of accidents that may involve human life

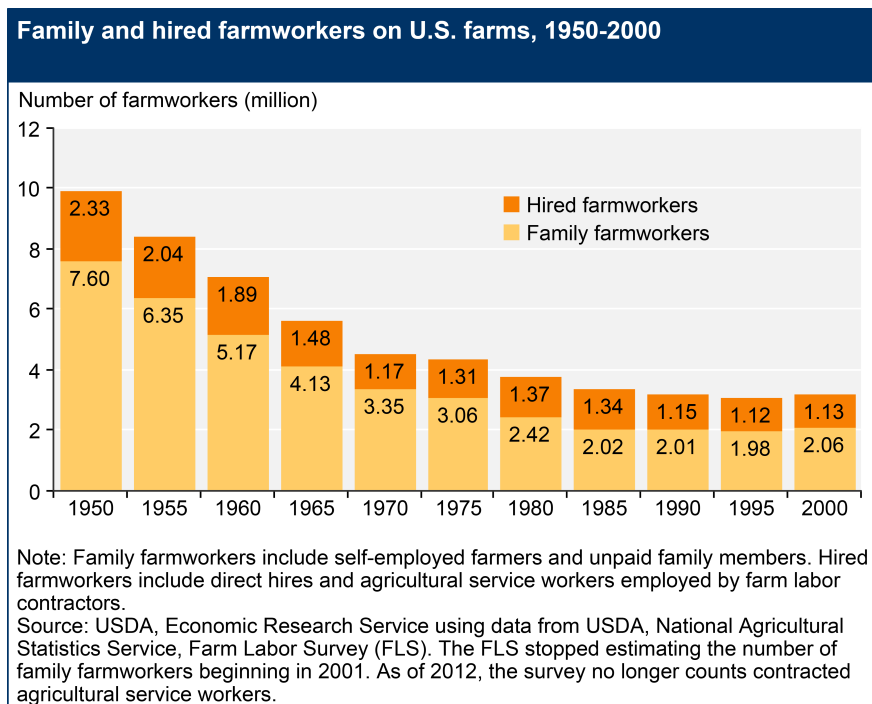


Figure 1.2: People employed in agriculture in the US, in millions [12].

Therefore, by automating the tractors, the overall productivity is ameliorated and substantial resources have been dedicated to the development of automated robots able to satisfy requirements in the agricultural field, save energy, protect the environment, and to improve productivity. For those reasons, studies were conducted to improve the tractive efficiency and power consumption rate optimization of intelligent tractors. Consequently, the research must be focused on topics regarding dynamics. This include analysis of parameters affecting traction, studies on modeling of traction dynamics, traction model parameters estimation, and finally traction control process.

1.2 Purpose and Approach

The main topic of this thesis is to ameliorate the traction performance of intelligent tractors. Thus, the primary focus is the development and the evaluation of an analytical model to address the dynamic motion behavior of an UGV applied to agricultural operations on deformable soils. To deal with the motion dynamics on soft terrains, suitable models for both longitudinal and lateral direction are necessary. This thesis proposes an analytical model based on the terramechanics theory. Then, the motion dynamics behavior is simulated by means of multibody system dynamics approach.

Subsequently, the second purpose of this research is to identify soil parameters that may affect traction. The identification algorithm is based on decoupled analysis of equations and allows to recognize terrain parameters useful for predictive traction control systems.

1.3 Literature review

Agricultural terrain is considered, in a physical manner, a deformable soil. Thus, the interaction between the wheel and the terrain is strictly different from the well-known tire-road interaction, typical for on-road vehicles. In fact, what differentiates these two physical models is that the wheel sinks into the loose soil and strictly affect the traction mobility. In this section, a state of the art analysis is carried out by presenting the different models with particular attention to the advantages and disadvantages that may occur in their application contexts.

In the literature, terrain is usually modeled as an elastic or a plastic material. Elasticity theory allows to model the terrain as an elastic medium. This method has found applications in the study of soil compaction and terrain damage due to vehicular traffic. On the other hand, modeling the terrain as a rigid, perfectly plastic material has found applications in the prediction of the maximum traction developed by off-road vehicles. Both of these physical models have limitations, for example, elasticity theory is valid only for limited vehicle load, so that the soil can be considered elastic. While, the theory of plastic equilibrium can only be used to estimate the maximum vehicle load that the soil can bear, but cannot be employed in calculating the wheel-sinkage. [27].

Following the theory assumptions mentioned before, several approaches have been developed in modeling the wheel-soil interaction. The main four are:

- finite element method (FEM)
- discrete element method (DEM)
- empirical model

- semi-empirical model

Computational techniques advancements in last years allow to model the terrain using the finite element method (FEM) or using the discrete element method (DEM). These methods have the potential capability to investigate dynamic aspects of the physical nature of vehicle–terrain interaction in a detailed way. The finite element method is a numerical technique that, by subdividing complex problems described by partial derivative equations (PDE) into a finite number of small segments, finds approximated solutions. In recent years, studies on the applications of FEM to the analysis of wheel–terrain interaction has proceeded significantly. In order to accommodate different types of soil behavior, an amount of constitutive models have been introduced. Because of the inelastic deformation of the terrain when subject to normal pressure and/or shear stress on the wheel–soil interface, the behavior of terrain materials is performed by means of pressure-dependent elastoplastic models. However, high computational cost still hinders its application in real-time operations.

The discrete element method is another numerical approach that represents soil as a collection of many discrete elements, where each one is described by its size, shape, position, velocity and orientation. In its basic form assumes that each element has stiffness characterized by a spring constant k and has damping denoted by a viscous damping coefficient η . It also assumes that along the wheel-soil patch contact exists a friction in the tangential direction denoted by coefficient μ . Anyway, computational cost is of paramount importance for real-time applications, therefore, even this approach is onerous to adopt because of high computational requirements [24].

The empirical model is generally obtained by interpolating a large amount of experimental data. Cone penetrometer and bevameter are typical instruments able to measure and to derive soil parameters. However, in most cases the mathematical relations obtained by means of interpolation data do not have physical significance and are strictly specific to the studied environment.

The theory about semi-empirical models treats physical dynamics under few assumptions. Bekker was the pioneer in the formulation of terramechanics models [3],[2]. Later on, Wong [29] and Reece [22] developed another model, widely used in straight-line and steadily motion. These models consider the wheel as a rigid undeformable soild that travels on a soft deformable terrain by combining both elastic and plastic theory. However, during years several researches were conducted to improve these models. Semi-empirical models are derived from theoretical analysis as well as experimental data. They are most commonly used due to their high fidelity and physical significance and in addition they are suitable for real-time application.

1.4 Outline

This thesis consists of six chapters. This chapter introduces purpose and approach of this research.

Chapter 2 addresses the development of the wheel-soil contact model. The investigation on the contact geometry and traction mechanics of the wheels on deformable soil is also described. A second order polynomial model is developed to fit the non-linear stress of the model. A numerical estimator is also developed to calculate entrance angle on the wheel.

Chapter 3 deals with the multibody system approach to analyze the motion behavior of the wheeled mobile robot. Simulation procedure using the proposed model is performed. Further, steering characteristics of the mobile robot is addressed, and then, a simplified full vehicle dynamics is simulated.

Chapter 4 presents an identification method based on decoupled analysis able to identify on-line the soil parameters. The terramechanics model sensitivity to soil parameters is also addressed and discussed.

Chapter 5 shows the results obtained by adopting the identification algorithm for three kind of deformable soils.

Chapter 6 summarizes the quality of results of this thesis and then provides recommendation for future work.

Chapter 2

Wheel-soil interaction model

2.1 Introduction

In this chapter the classical model approach is presented. Firstly, a kinematic analysis of a rigid wheel rolling on a soil surface is conducted by explaining all the parameters affecting wheel-terrain interaction mechanics. Subsequently, stress distributions are discussed and, then, equations of wheel forces and torques in a 3-axis reference frame are obtained. Due to the non-linearity of stress equations, an accurate closed-form solution capable of real-time implementation is developed. However, there are few studies that deeply explore the lateral characteristics of a wheel on deformable soil, which are important requisites in a study of the vehicle's motion dynamics. In fact, the majority of models existing in literature derive a closed-form solution by simplifying the stress equations through the linearization method. Although this method is easy to apply and does not require large time-consumption to solve equations, the model accuracy could not be guaranteed because the stresses are mainly nonlinear, especially for soils with low sinkage exponents, and also it can only be used for straight-line driving scenarios. This is due to the simplification technique performed by using polynomial approximation of stress distributions beneath the wheel. In addition, the explicit-form solution of the bulldozing resistance exerted by the wheel's side surface during steering maneuvers is also developed, based on the stress distribution equations proposed by Bekker [3] and Hegedus [11].

To calculate the forces/torques, it is necessary to determine the wheel-soil contact geometry, i.e., the entry angle, according to the normal wheel load. Thus, in order to achieve a complete terramechanics-based model (TBM), an iterative method is performed to find the entry angle.

Finally, a mobile robot locomotion model is developed by combining the TBM model with a vehicle dynamical model, which is used to simulate motion dynamics of the vehicle's body according to wheel contact forces. To accomplish this task, a multibody system (MBS)-based approach, where the robot is modeled as an

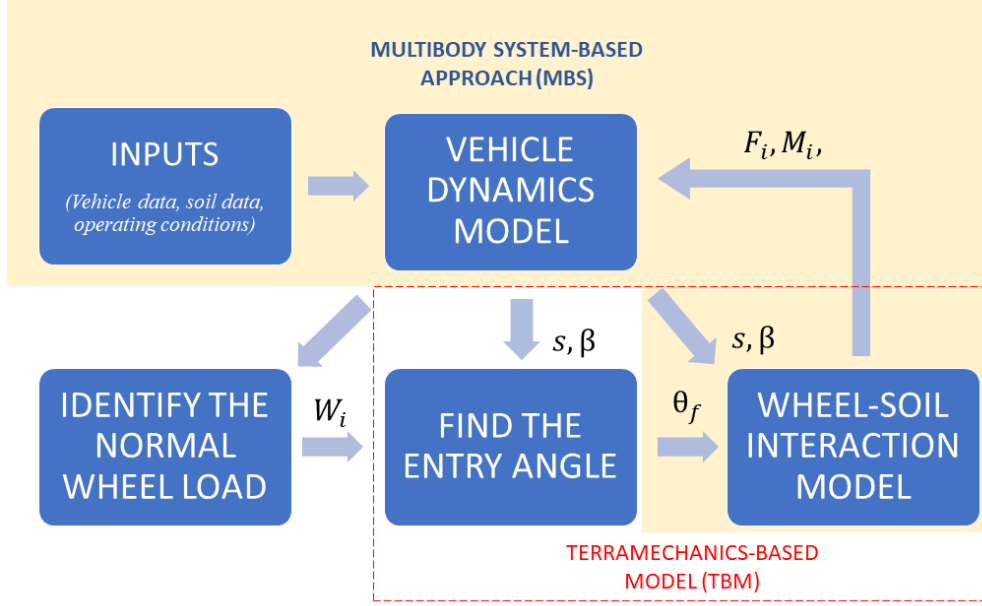


Figure 2.1: Wheel-soil interaction model combined with vehicle dynamics model

articulated multi-rigid-body system, while the wheel contact forces are identified by the wheel–soil interaction model. As shown in Fig. 2.1, the normal force of each wheel W_i is obtained by the classical vehicle dynamics. Once the normal load is computed, then it is possible to find the contact entry angle θ_f by means of numerical iterations, and therefore to determine the longitudinal force, lateral force, and moments acting on each wheel of the vehicle.

2.1.1 Assumptions

In this thesis, the following assumptions are made.

- Rigid wheel on deformable soil.

Classical terramechanics theory is based on assumptions that wheel is composed by rigid materials, while the terrain is considered as a plastic/elastic medium. This has found many applications in several fields, first among them certainly are planet exploration missions, where the rovers are usually equipped with rigid wheels. However, mobile robots operating in agriculture often are equipped with pneumatic tires. This could lead to some slight inaccuracies in modeling. Anyway, the terramechanics approach still remains a good compromise due to its easy application in fast prototyping and because the effects of pneumatic tires in the traction analysis can be neglected at operating conditions considered in this research.

- Slow velocity.
The general speed of the UGV is relatively slow so that the load transfer due to acceleration can be ignored. The aerodynamic effect can also be neglected.
- Flat terrain.
The motion is considered only in the horizontal plane.
- The center of mass coincides with the geometrical center of the body's robot.

2.2 Contact geometry and kinematic analysis

2.2.1 Wheel coordinate system

As mentioned in the previous section, a rigid wheel rotating on a flat deformable terrain is considered. As shown in Fig. 2.2, the wheel reference frame is determined using a right-hand frame.

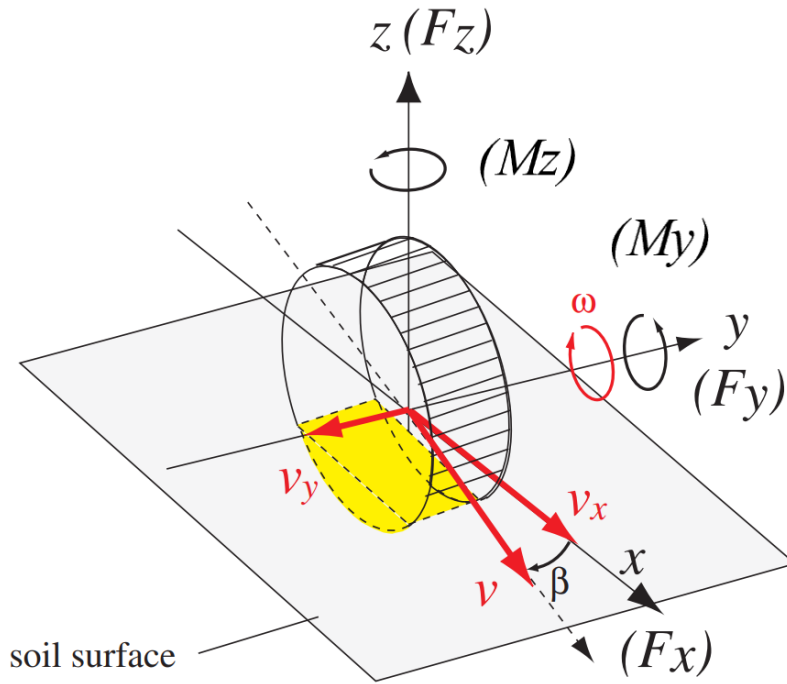


Figure 2.2: Wheel coordinate system [15]

Frame xyz is a coordinate system attached to the wheel carrier with the origin coinciding with the wheel center, the longitudinal direction is denoted by x , the lateral direction by y , and the vertical direction by z . The coordinate frame rotates according to the steering action of the wheel (the yaw rotation around the z axis), while it does not rotate with respect to the driving motion of the wheel (the pitch

rotation around the y axis) and neither with respect to the rolling motion (roll rotation around the x axis). This is due because both drawbar pull F_x and side force F_y must be parallel to the horizontal plane.

2.2.2 Slip ratio and slip angle

In Fig. 2.3 are illustrated both side and top view of the wheel coordinate system with kinematic variables involved in wheel rotation.

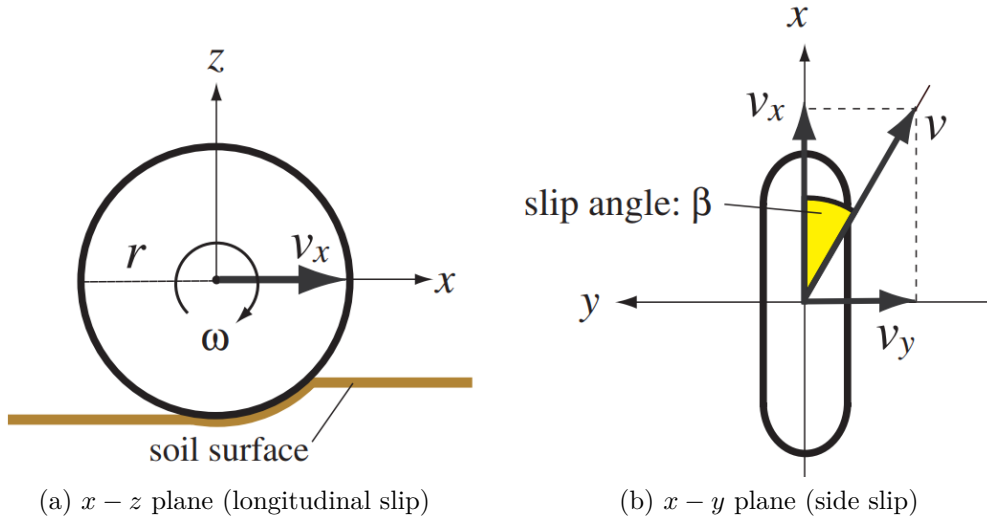


Figure 2.3: Side view and top view of the wheel [15]

The slip in the longitudinal direction is expressed by the slip ratio s , which is defined as:

$$s = \begin{cases} (r\omega - v_x)/r\omega & (r\omega \geq v_x, \quad 0 \leq s \leq 1) & : \text{driving} \\ (r\omega - v_x)/v_x & (r\omega < v_x, \quad -1 \leq s \leq 0) & : \text{breaking} \end{cases} \quad (2.1)$$

where v_x is the longitudinal velocity of the wheel, r is the wheel radius, ω is the wheel angular velocity.

From equation (2.1), the slip ratio can assume values from -1 to 1. Specifically, when the slip ratio is in the range (0,1) the wheel is in driving condition; while when the slip ratio is in the range (-1,0) the wheel is in breaking condition (skidding).

The slip angle β in the lateral direction is defined as follows:

$$\beta = \tan^{-1} v_y/v_x \quad (2.2)$$

where, as shown in Fig. 2.3b, it is a function of v_x and lateral velocity v_y which determines the mean velocity vector (\mathbf{v}) of the wheel.

2.2.3 Wheel sinkage

When wheel interacts with loose terrain, part of it sinks into the soil and this phenomenon in the literature is referred as wheel sinkage. This is considered as the distance between the lowest point of the wheel in the soil and the horizontal flat terrain. The wheel sinkage is divided into static and dynamic sinkages. The static sinkage depends on the vertical load of the wheel, while the dynamic sinkage is caused by the wheel rotation. In Fig. 2.4 is represented the difference between static and dynamic sinkage and how it is influenced by the slip/skid ratio.

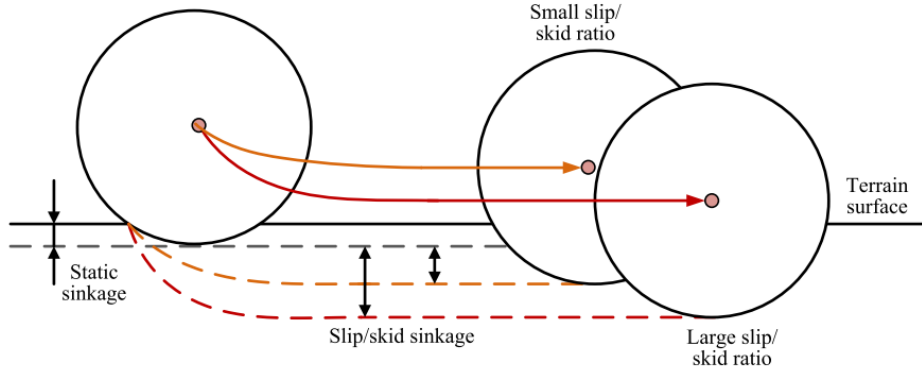


Figure 2.4: Static and slip sinkages of a wheel [5]

Static sinkage

The static pressure on homogeneous terrain $\sigma(h)$, generated under a flat plate, was formulated by Bekker [2] in this way:

$$\sigma(h) = \left(\frac{k_c}{b} + k_\phi \right) h^n \quad (2.3)$$

where h is the sinkage of the plate and b is the smaller width of the plate; k_c is the cohesive modulus, k_ϕ is the frictional modulus and n is the sinkage exponent. These last three parameters are dependent on the soil type.

As shown in Fig. 2.5a, the wheel sinkage $h(\theta)$ at an arbitrary wheel angle θ is geometrically given by the following formula:

$$h(\theta) = r(\cos \theta - \cos \theta_s) \quad (2.4)$$

where r is the wheel radius and θ_s is the static contact angle. At this point, one can obtain the following equation by substituting Eq. (2.4) into Eq. (2.3):

$$\sigma(\theta) = \left(\frac{k_c}{b} + k_\phi \right) r^n (\cos \theta - \cos \theta_s)^n \quad (2.5)$$

For a towed wheel without shear stress, the normal force that balances the vertical load is exclusively caused by the normal stress. The normal load equation is expressed as follows:

$$W = r b \int_{-\theta_s}^{\theta_s} \sigma(\theta) \cos \theta d\theta \quad (2.6)$$

By combining Eq. (2.5) and Eq. (2.6), it is obtained an analytical equation that relates the vertical load W to the static angle θ_s stated as:

$$W = r^{n+1} (k_c + b k_\phi) \int_{-\theta_s}^{\theta_s} (\cos \theta - \cos \theta_s)^n \cos \theta d\theta \quad (2.7)$$

Therefore, by providing vertical load W , the static entrance angle θ_s of the wheel can be obtained by solving Eq. (2.7). However, this equation is not easy to solve, so it is needed an explicit form solution that allows to estimate static sinkage directly from wheel load.

In literature different solutions have been proposed, among them the Bekker's one [2, 3] expressed as:

$$h \approx \left[\frac{W}{\sqrt{2} r b K_s (1 - n/3)} \right]^{1/(n+1/2)} \quad (2.8)$$

where K_s is the equivalent lumped pressure-sinkage coefficient, and it is equal to:

$$K_s = \left(\frac{k_c}{b} + k_\phi \right) \quad (2.9)$$

Eq. (2.8) is intended as an approximation that allows to estimate wheel sinkage as function of vertical load. Bekker's model has many limitations due to the simplification error. According to Bekker [2, 3] and Wong [29], acceptable estimations may be obtained for moderate sinkage ($h_s \leq r/3$ or $\theta_s \leq 48$ deg).

However, estimation accuracy for sinkage based on Eq. (2.7) is low for dry, sandy soil if there is significant slip sinkage.

In fact, the normal stress distribution in Bekker's model is not accurate. Experimental results have revealed that the actual normal pressure beneath a rigid wheel is different from that assumed. The maximum normal stress occurs at an angle ahead of the bottom-dead-point and then gradually decreases to zero [5].

Therefore, on the basis of those limitations, Eq. (2.7) is not acceptable to estimate the dynamic wheel sinkage of a rotating wheel, but it still remains a good model to approximate the static sinkage because it is not affected by slip ratio and shear stress.

In Fig. 2.6 are shown static sinkages as function of wheel vertical load for three different soil types according to Bekker's formula (2.7).

Then, the relation between the static sinkage h_s and static wheel contact angle θ_s can be derived as follows:

$$h_s = r(1 - \cos \theta_s) \quad (2.10)$$

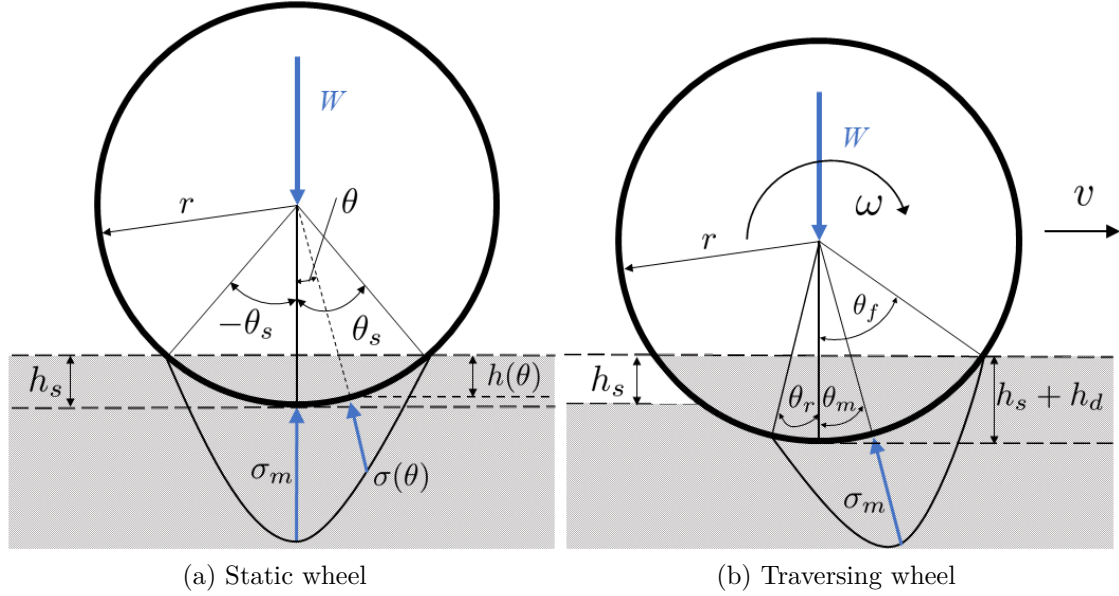


Figure 2.5: Stress distribution and wheel sinkage under static and traversing wheels

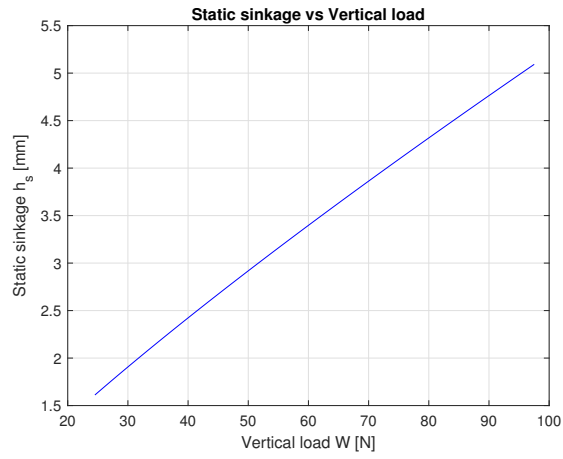
Dynamic sinkage

Once the wheel starting to move, as illustrated in figure 2.5b, wheel sinkage starts growing up due to many factors. Therefore, the dynamic sinkage is a complicated phenomenon depending on functions, such as the slip ratio of the wheel, the wheel surface pattern, and the soil characteristics.

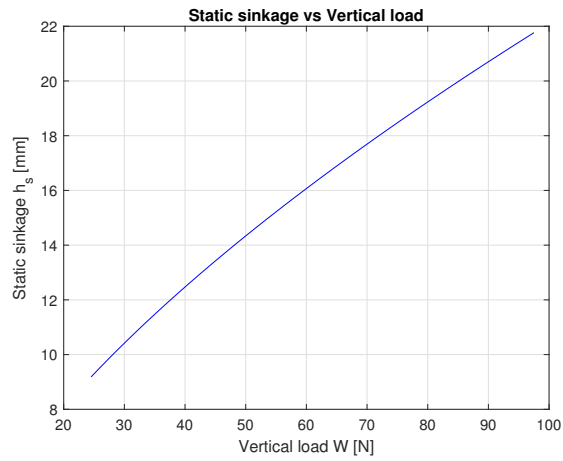
It is not easy to obtain an analytical solution for the dynamic sinkage, thus several approaches to estimate it have been used in literature. For example, Ding [5] has proposed an analytical model based on stress simplification and an improved sinkage exponent ($N = n_0 + n_1 s$) which takes into account slip ratio effects, where n_0 and n_1 are soil parameters.

Another approach proposed by Jia [18] directly estimate the contact entry angle θ_f instead. It is based on a non-iterative method considering the stress distribution along the contact area as a sinusoidal function.

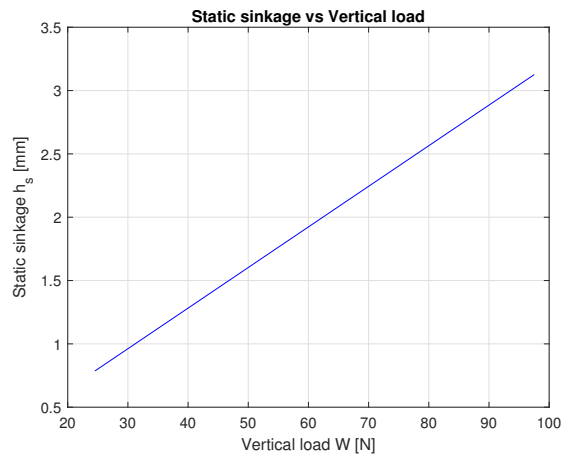
In this thesis it was chosen to calculate dynamic sinkage by means of numerical evaluation. The numerical procedure is outlined in section 2.6.1.



(a) Sandy loam



(b) Dry sand



(c) Clayey soil

Figure 2.6: Static wheel sinkage estimated in three different kinds of soil. (W ranged from 25 N to 98 N; $r = 92$ mm, $b = 107$ mm)

Total wheel sinkage is then defined as the sum of the static and dynamic sinkages:

$$h_f = h_s + h_d \quad (2.11)$$

2.2.4 Wheel-soil contact geometry

Figure 2.7 shows a driven rigid wheel traveling over a flat soil surface, where r is the wheel radius; b , the wheel width; ω , the wheel angular velocity; v_x , the longitudinal velocity; θ_f , the entrance angle; θ_r , the exit angle; θ_m , the angle of maximum stress; h_f , the wheel sinkage relative to the uncompacted soil in front of the wheel, while h_r represents the rut recovery.

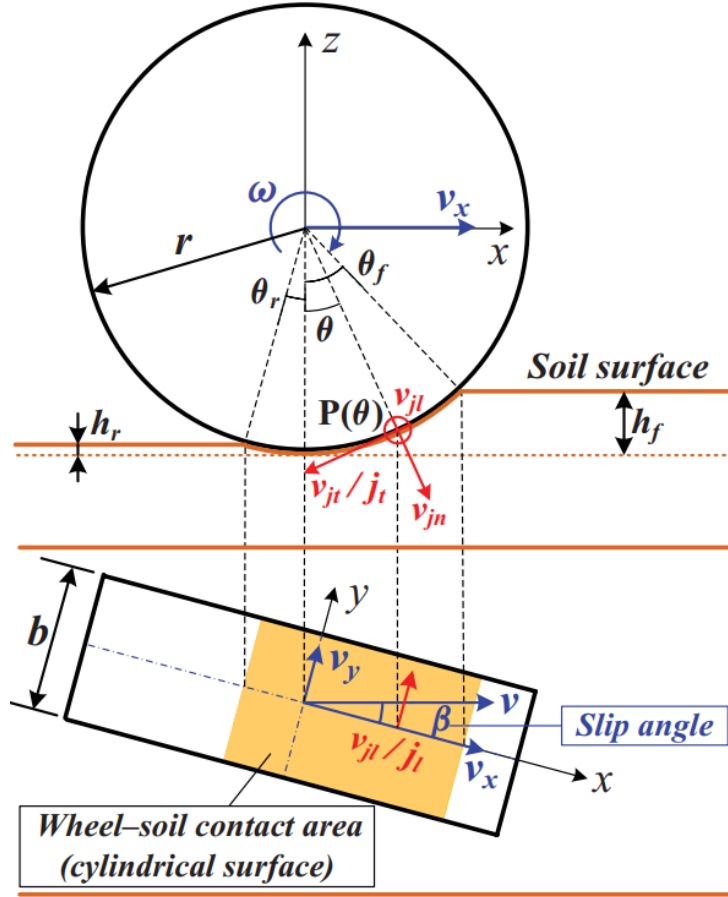


Figure 2.7: Diagram of wheel-soil interaction mechanics (cylindrical surface) [18]

Contact angles

Once the wheel sinkage h_f is obtained, the wheel contact angles can be calculated. The angle from the vertical to where the wheel begins to contact the soil is defined as the entry angle. The angle from the vertical to where the wheel loses the contact with soil is defined as exit angle. Thus, the wheel contact patch on deformable soil is defined by the region from the entry angle to the exit angle.

Contact angles are geometrically expressed as function of wheel sinkage:

$$\begin{cases} \theta_f = \cos^{-1}(1 - h_f/r) \\ \theta_r = -\cos^{-1}(1 - h_r/r) = -\cos^{-1}(1 - \lambda h_f/r) \end{cases} \quad (2.12)$$

where $\lambda = h_r/h_f$ and it can be determined by means of sensors or vision-based measurement system.

Shear rates

As shown in Fig. 2.7, $P(\theta)$ denote a point on the cylindrical wheel-soil contact patch with a contact angle θ . Hence, from geometry it is possible to derive the tangential shear rate v_{jt} , the lateral shear rate v_{jl} , and the compression speed v_{jn} corresponding to $P(\theta)$ as:

$$\begin{cases} v_{jt}(\theta) = -v_x \cos \theta + r \omega \\ v_{jl}(\theta) = v_y \\ v_{jn}(\theta) = v_x \sin \theta \end{cases} \quad (2.13)$$

Shear deformations

Shearing forces may cause shearing deformation, in fact an element subject to shear does not change in length and orientation but undergoes a change in shape.

Shear deformations of $P(\theta)$ can be identified by integrating corresponding shear rates. By using a quasi-static approach (Jia [18]), the shear deformations (positive directions are given in Fig. 2.7) in the tangential and lateral directions can be obtained as follows:

$$\begin{cases} j_t(\theta) = r[(\theta_f - \theta) - (1 - s)(\sin \theta_f - \sin \theta)] \\ j_l(\theta) = r(1 - s)(\theta_f - \theta) \tan \beta \end{cases} \quad (2.14)$$

and the magnitude of the overall shear deformation of $P(\theta)$:

$$j(\theta) = \sqrt{j_t(\theta)^2 + j_l(\theta)^2} \quad (2.15)$$

In addition, for purely smooth wheels, there exist certain limits for the shear deformation $j(\theta)$ due to the absence of wheel lugs which generate wheel–soil interlock mechanism. Therefore, for such circumstances, the shear deformation should be computed as:

$$j(\theta) = \min(j(\theta), j_{max}) \quad (2.16)$$

where j_{max} is the shear deformation limit.

2.3 Stress distribution analysis

2.3.1 Normal stress

Based on terramechanics models, stresses beneath a rotating wheel can be modeled as shown in Fig. 2.8. There are various approaches to model the normal stress underneath the wheel. Wong’s formulas in ref. [22] are extended to calculate stress distributions along the wheel–soil interface.

The normal stress can be expressed by the following formula:

$$\sigma(\theta) = \begin{cases} r^n \left(\frac{k_c}{b} + k_\phi \right) (\cos \theta - \cos \theta_f)^n & (\theta_m \leq \theta \leq \theta_f) \\ r^n \left(\frac{k_c}{b} + k_\phi \right) (\cos \theta_e - \cos \theta_f)^n & (\theta_r \leq \theta \leq \theta_m) \end{cases} \quad (2.17)$$

where k_c is the cohesive modulus of the soil, k_ϕ is the frictional modulus and n is the soil sinkage exponent; while θ_e is the equivalent front region contact angle for points in the rear contact region and θ_m is the angle corresponding to the maximum normal stress.

These two angles are expressed as:

$$\theta_m = (a_0 + a_1 s) \theta_f \quad (2.18)$$

$$\theta_e = \theta_f - \frac{\theta - \theta_r}{\theta_m - \theta_r} (\theta_f - \theta_m) \quad (2.19)$$

where a_0 and a_1 are soil-dependent constant parameters.

2.3.2 Shear stress

As shown in Fig. 2.8, the shear stress distribution is subdivided in tangential shear stress and lateral shear stress.

This thesis refers equation for shear stress proposed by Janosi and Hanamoto [17]. Based on the their formula, the magnitude of the overall shear stress is:

$$\tau(\theta) = [c + \sigma(\theta) \tan \phi] (1 - \exp^{-|j(\theta)|/K}) \quad (2.20)$$

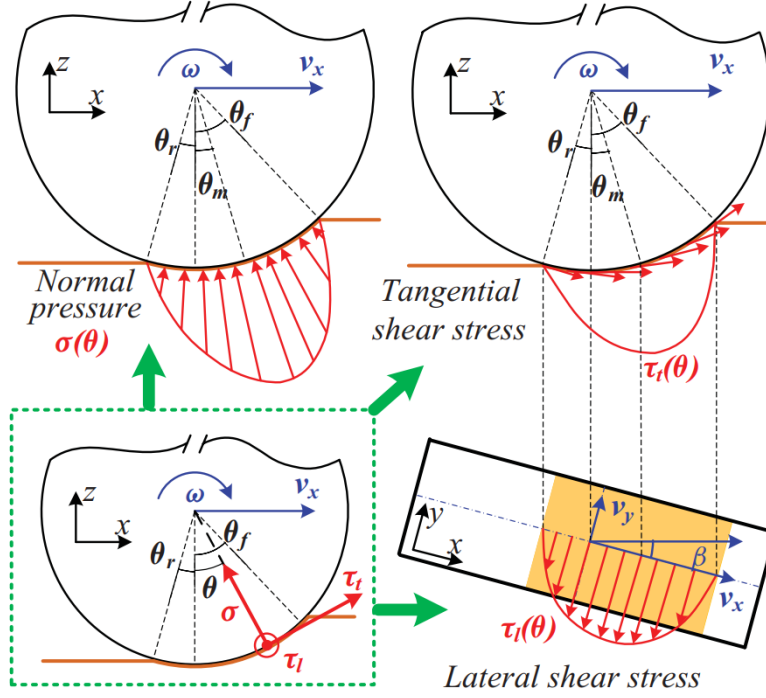


Figure 2.8: Normal and shear stresses along the wheel-soil contact area [18]

where, c is the cohesion stress parameter, ϕ is the internal friction angle of the soil, j is the soil deformation, and K is the shear deformation modulus of the soil.

In accordance with Eq. (2.20), the shear stress can be modeled by a stress-deformation curve as shown in Fig. 2.9, where τ_{max} is the maximum value of the shear stress, j is the shear displacement and K , in this case, is equivalent to a time constant. Therefore, when $j(\theta) = K$, the magnitude of the shear stress corresponds to the 63% of τ_{max} value. The maximum shear stress is obtained from the Coulomb-Terzaghi shear strength equation [3] expressed as:

$$\tau_{max} = c + \sigma(\theta) \tan \phi \quad (2.21)$$

The shear strength is then equal to the sum of normal stress σ and cohesion c , while $\tan \phi$ is the coefficient of plane sliding friction, which describes the surface roughness, and hardness of the materials constituting the slope. This means that cohesion of the material binds particles of the soil irrespective of the normal pressure, while particles of frictional masses can be held together only applying a normal pressure between them.

In Fig. 2.10, it is shown the Mohr-Coulomb failure criterion, where in the abscissa axis it is represented the normal pressure and in the ordinate axis it is shown the shear stress. So it is possible, for different state of stress, to draw different circles. These kind of circles are called Mohr's circles and each one of them is a geometric

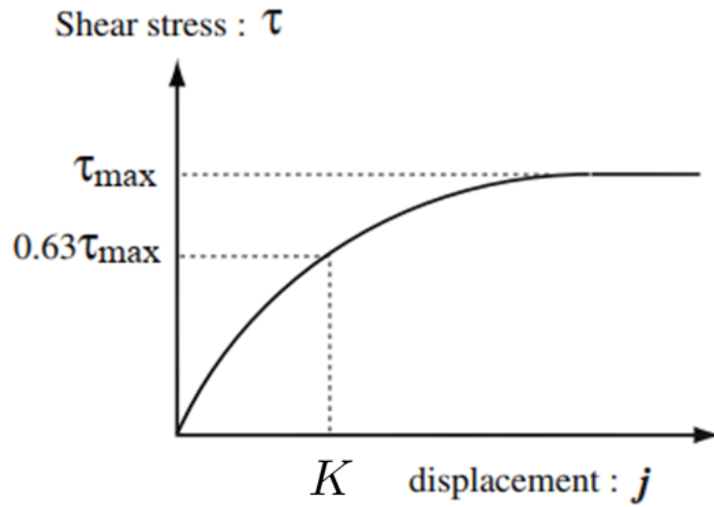


Figure 2.9: Shear stress-deformation curve [15]

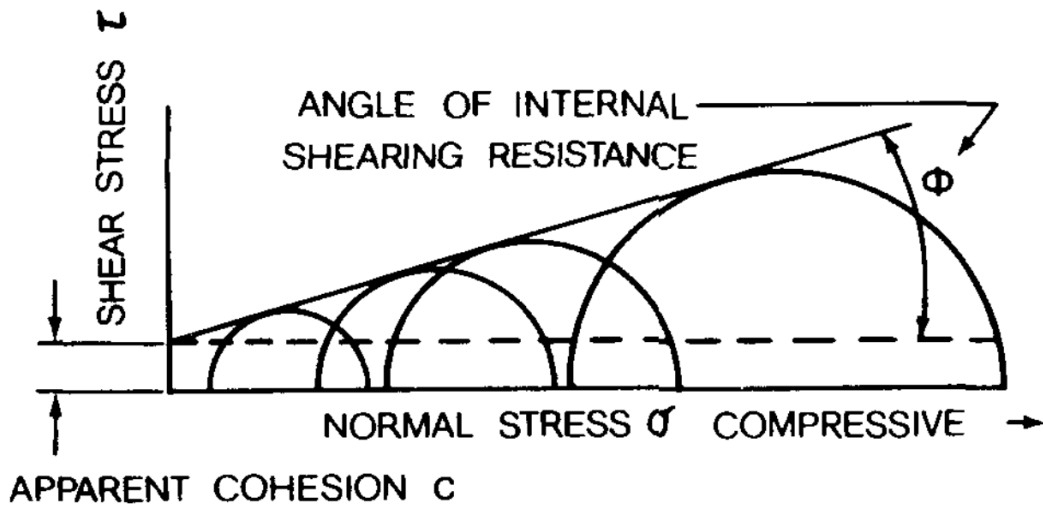


Figure 2.10: Mohr-Coulomb failure criterion [29]

representation of the 2-D transformation of stresses at a point in the soil. If a straight line envelope is drawn to the set of these circles, the formula (2.21) can be obtained, with the friction angle ϕ represented by its slope, and cohesion c obtained by the intercept of the envelope with ordinate axis.

If a Mohr circle touches the line envelope, terrain failure will take place at that point. Therefore, if the applied tractive pressure exceeds τ_{max} , terrain failure and

excessive wheel slip may occur, which will reduce wheel traction (Iagnemma et al. 2004 [21]).

Shear stress along longitudinal and lateral direction

As mentioned before, the shear stress τ is the overall magnitude of two components: tangential shear stress τ_t and lateral shear stress τ_l . On the basis of the isotropic shear stress assumption, tangential and lateral shear stress can be derived as:

$$\tau_i(\theta) = \tau(\theta) \frac{v_{ji}(\theta)}{\sqrt{v_{jt}(\theta)^2 + v_{jl}(\theta)^2}} \quad (i = t, l) \quad (2.22)$$

The direction of the shear stress at any point on the wheel–soil interface is always opposite to the shearing velocity at that point, which is more accurately modeled by the isotropic method [18].

Table 2.1: Soil parameters for different soil types [21]

Parameter [unit]	Description	Dry Sand	Sandy Loam	Clayey soil
n [-]	Sinkage exponent	1.1	0.7	0.5
c [kPa]	Cohesion	1.0	1.7	4.14
ϕ [deg]	Internal friction angle	30.0	29.0	13.0
k_c [kN/m ^{$n+1$}]	Cohesive modulus	0.9	5.3	13.2
k_ϕ [kN/m ^{$n+2$}]	Frictional modulus	1523.4	1515.0	692.2
K [m]	Shear modulus	0.025	0.025	0.01
γ [kN/m ³]	Specific weight of soil	16.18	15.20	13.24

Table 2.2: Smooth wheel parameters

Parameter [unit]	Description	Value
r [m]	Radius	0.092
b [m]	Wheel width	0.107

The stress graphs in Fig. 2.11 are obtained from Eqs. (2.17), (2.20), (2.22) by using as values the soil parameters, the wheel parameters and the operating conditions parameters given in Tables 2.1, 2.2, 2.3.

2.4 Forces/torques analysis

The forces and torques exerted on the wheel can be determined by integrating the corresponding stresses along the wheel–soil contact area as shown in Fig. 2.12.

Table 2.3: Operating conditions parameters

Parameter [unit]	Description	Value
s [-]	Slip ratio	0.3
ω [rad/s]	Angular velocity	4
β [deg]	Slip angle	12
θ_f [deg]	Entry angle	30
θ_r [deg]	Exit angle	0
θ_m [deg]	Maximum normal stress angle	15

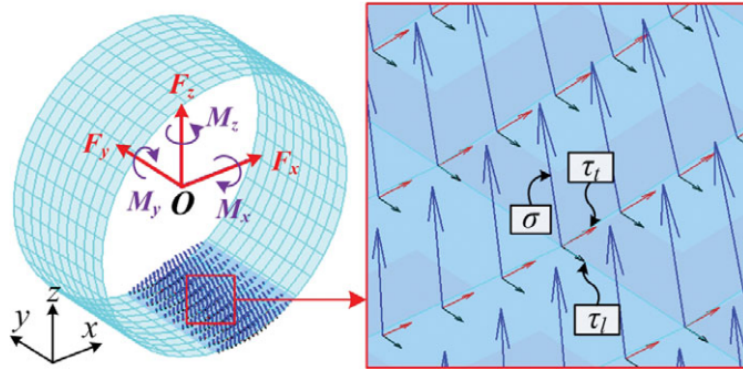


Figure 2.12: Forces and torques by integrating the stresses along the wheel-soil contact area [18]

2.4.1 Drawbar pull (F_x)

The drawbar pull F_x is the force exerted on the wheel from the soil along the longitudinal direction. It is meant as the difference between tractive effort available and tractive effort required to overcome resistance at a specified speed. These two last quantities are respectively given by the shear stress in the x direction and normal stress. Therefore, by subtracting $\sigma(\theta)$ from $\tau_t(\theta)$, F_x is then calculated by integrating this difference between stresses along the wheel-soil contact area from the entry angle θ_f to the exit angle θ_r .

$$F_x = r b \int_{\theta_r}^{\theta_f} (\tau_t(\theta) \cos \theta - \sigma(\theta) \sin \theta) d\theta \quad (2.23)$$

2.4.2 Side force (F_s)

The side force F_s acts along the y axis of the wheel when the vehicle performs steering maneuvers. In order to model this phenomenon, in this thesis F_s is considered

as the sum of two different forces: F_y , force beneath the wheel due to shear motion, and F_b , resistance force acting on the lateral face of the wheel.

Hence the side force F_s is modeled as shown in Fig. 2.13:

$$F_s = F_y + F_b \quad (2.24)$$

where F_y is obtained by integrating the lateral shear stress t_l along the contact patch as follows:

$$F_y = -r b \int_{\theta_r}^{\theta_f} \tau_l(\theta) d\theta \quad (2.25)$$

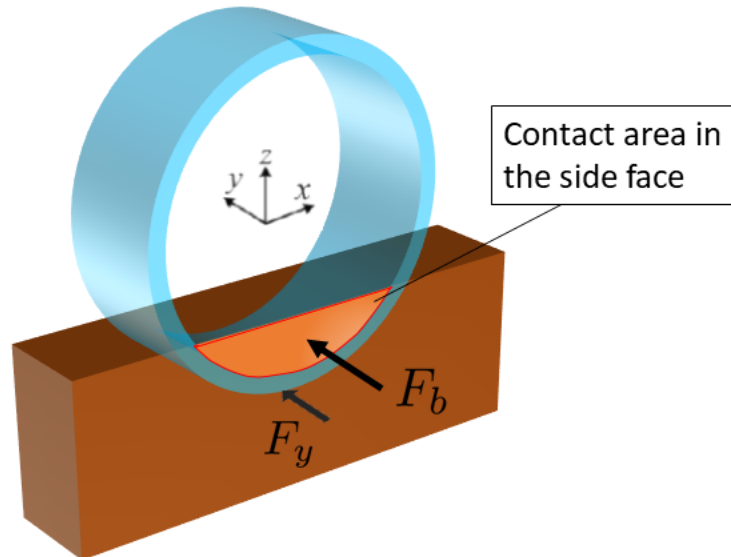


Figure 2.13: Side force model

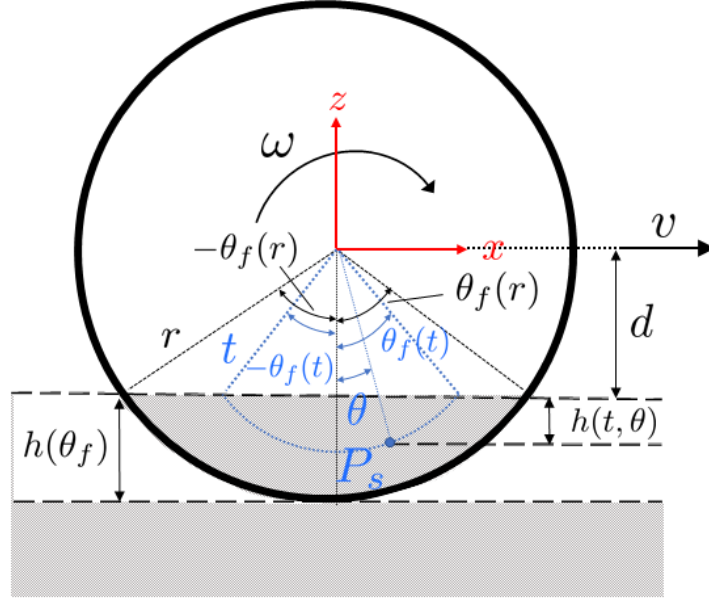


Figure 2.14: Identify the side surface contribution

Bulldozing resistance

In order to model the side surface contribution it is necessary to study the effect of bulldozing resistance F_b . For rigid wheels with sidewalls, bulldozing resistance from the side surfaces can contribute conspicuously to the side force during steering maneuvers.

To calculate F_b , Bekker [3] and Hegedus [11] equations are employed. As shown in Fig. 2.14, the normal stress corresponding to the point P_s on the side surface is expressed as follows:

$$\sigma(t, \theta) = a_s h(t, \theta) + b_s \quad (2.26)$$

$$: \begin{cases} a_s = \gamma c_s^2, & b_s = 2 c c_s & \text{Bekker [3]} \\ a_s = 2 \gamma c_s (c_s + c_s^2 \tan \phi), & b_s = 2 c c_s & \text{Hegedus [11]} \\ c_s = \tan\left(\frac{\pi}{4} + \frac{\phi}{2}\right) \end{cases} \quad (2.27)$$

where γ is the soil specific weight, and $h(t, \theta)$ is the corresponding underground depth and it can be calculated as:

$$h(t, \theta) = t(\cos \theta - \cos \theta_f(t)) \quad (2.28)$$

where t is the distance from point P_s to the wheel center.

Therefore, by integrating the normal pressure along the side surface contact area, the bulldozing resistance can be calculated as:

$$F_b = \int_d^r t \int_{-\theta_f}^{\theta_f} \sigma(t, \theta) d\theta dt \quad (2.29)$$

Finally, by solving equation (2.29), it is obtained the bulldozing resistance contribution in an explicit-form solution formulated as:

$$F_b = 2 a_s r \sqrt{1 - d^2/r^2} (r^2 - d^2)/3 + (a_s d + b)(r^2 \cos^{-1}(d/r) - r d \sqrt{1 - d^2/r^2}) \quad (2.30)$$

where $d = r - h$ is the distance between the wheel center and the lowest part of the wheel which has not sunk into the soil.

2.4.3 Vertical force (F_z)

The vertical force F_z acts from the soil to the wheel in vertical direction. It depends on wheel soil contact and it is opposite to the wheel load W . In equilibrium condition $F_z = W$.

Then, F_z is obtained by integrating shear stress and normal stress along the contact area as follows:

$$F_z = r b \int_{\theta_r}^{\theta_f} (\sigma(\theta) \cos \theta + \tau_t(\theta) \sin \theta) d\theta \quad (2.31)$$

2.4.4 Roll moment (M_x)

The roll moment M_x is a function of steering actions and it may cause roll motion around the x axis. It is calculated by integrating the lateral shear stress along the contact area and it is expressed as:

$$M_x = -r^2 b \int_{\theta_r}^{\theta_f} \tau_l(\theta) \cos(\theta) d\theta \quad (2.32)$$

2.4.5 Resistance torque (M_y)

The resistance torque M_y is the one that a wheel should overcome to rotate on a surface. If a wheel moving at constant velocity, driving torque and resistance

torque are equal due to the Newton's law for rotation:

$$\sum_i M_i = J \frac{d\omega}{dt} \quad (2.33)$$

where the sum of the torques (driving and resistance) on a rotating system about a fixed axis equals the product of the moment of inertia J and the derivative of angular velocity ω .

Then, M_y is obtained by integrating longitudinal shear stress along contact patch as follows:

$$M_y = r^2 b \int_{\theta_r}^{\theta_f} \tau_t(\theta) d\theta \quad (2.34)$$

2.4.6 Yaw moment (M_z)

The Yaw moment is due by steering maneuvers and it causes rotation around z axis. It is obtained by integrating lateral shear stress along the contact area as follows:

$$M_z = -r^2 b \int_{\theta_r}^{\theta_f} \tau_l(\theta) \sin(\theta) d\theta \quad (2.35)$$

2.5 Stress simplification

The integral equations presented in the previous section cannot be solved analytically due to the complexity of the stress equations. In order to prototype a closed-form wheel-soil interaction model capable of real-time implementation, a simplification of the stress distribution equations is required.

To simplify the wheel-soil interaction model, the stress distribution can be approximated as polynomials of θ . By using a linear approximation method it is possible to develop a closed-form solution for straight-line motion scenarios. However, as shown in Fig. 2.11, stresses are generally nonlinear, thus the linear approximation sometimes leads to large errors. This is particularly true if the soil's sinkage exponent n is small (e.g., clayey soil) [18]. Therefore, instead of linear approximation in this thesis it is used a quadratic approximation method. In fact, the model accuracy is improved significantly, while the increase in computational load is minimal. To accomplish this formulation, two new angles, i.e., the front medium angle θ_{fm} and the rear medium angle θ_{rm} , are introduced.

These angles can be computed as:

$$\begin{cases} \theta_{fm} = (\theta_f + \theta_m)/2 \\ \theta_{rm} = (\theta_r + \theta_m)/2 \end{cases} \quad (2.36)$$

Hence, the quadratic form of the stresses can be expressed as:

$$\tilde{p}(\theta) = a_i^p \theta^2 + b_i^p \theta + c_i^p \quad ({}^l\theta_i \leq \theta \leq {}^u\theta_i) \quad (2.37)$$

where:

- $i = f, r$ (front or rear region)
- $p = \sigma, \tau, \tau_l, \tau_t$ (stress type)
- ${}^l\theta_r = \theta_r$
- ${}^u\theta_r = {}^l\theta_f = \theta_m$
- ${}^u\theta_f = \theta_f$

At this point, it is possible to estimate the parameters of the second order polynomial by applying the least square method by means of Eq. (2.38).

$$\begin{bmatrix} a_i^p \\ b_i^p \\ c_i^p \end{bmatrix} = \begin{bmatrix} \theta_m^2 & \theta_m & 1 \\ \theta_{im}^2 & \theta_{im} & 1 \\ \theta_i^2 & \theta_i & 1 \end{bmatrix}^{-1} \begin{bmatrix} p_m \\ p_{im} \\ p_i \end{bmatrix} \quad (2.38)$$

In Fig. 2.16 are shown graphs that compare original stress distribution (continuous line) with quadratic stress distribution (dotted line).

The soil data, the wheel data and the operating conditions used for simulations are respectively given in tables 2.1, 2.2, 2.3.

In order to evaluate the goodness of fit of the quadratic model, both root-mean-square errors (RMSE) and mean-absolute errors (MAE) are respectively summarized in Tables 2.4, 2.5.

RMSE is calculated as:

$$\text{RMSE} = \sqrt{\frac{1}{n_{tot}} \sum_i^n (y_i - \hat{y}_i)^2} \quad (2.39)$$

MAE is calculated as:

$$\text{MAE} = \frac{1}{n_{tot}} \sum_i^n |y_i - \hat{y}_i| \quad (2.40)$$

where n_{tot} is the number of samples, y is the expected value and \hat{y} is the estimated one.

Root-mean-square error will always be larger or equal to the mean-absolute error as stated by theory [20]. It is notable that $\text{MAE} \leq \text{RMSE}$ is fully achieved by the performed simulation. As shown in Tables 2.4 and 2.5, the errors are quite small except for Clayey soil, in particular the normal stress is approximated with $\text{RMSE} \approx 6 \text{ kPa}$. As mentioned before, this is due to its small sinkage exponent n .

Table 2.4: Root-mean-square error (RMSE)

Soil type	RMSE [kPa]			
	σ	τ	τ_t	τ_l
Sandy loam	2.1623	0.4808	0.4315	0.2120
Dry sand	0.0680	0.0235	0.0220	0.0086
Clayey soil	6.3563	0.8712	0.7798	0.3883

Table 2.5: Mean-absolute error (MAE)

Soil type	MAE [kPa]			
	σ	τ	τ_t	τ_l
Sandy loam	1.7427	0.3558	0.3214	0.1524
Dry sand	0.0582	0.0203	0.0190	0.0074
Clayey soil	4.9637	0.5657	0.5072	0.2511

2.5.1 Closed-form solution

Once estimated the quadratic parameters of approximated stresses from Eq. (2.38), a closed-form solution of forces/torques in the 3-axes reference frame can be finally obtained.

The drawbar pull is calculated as follows:

$$\tilde{F}_x = rb \sum_{i=f,r} \left[(a_i^{\tau_t}(\theta^2 - 2) - 2a_i^\sigma \theta + b_i^{\tau_t} \theta - b_i^\sigma + c_i^{\tau_t}) \sin \theta + (a_i^\sigma(\theta^2 - 2) + 2a_i^{\tau_t} \theta + b_i^\sigma \theta + b_i^{\tau_t} + c_i^\sigma) \cos \theta \right] \Bigg|_{\theta=u_i}^{\theta=l_i} \quad (2.41)$$

The lateral force due to the shear stress is calculated as follows:

$$\tilde{F}_y = rb \sum_{i=f,r} \left[(a_i^{\tau_t}(\theta^2 - 2) - 2a_i^\sigma \theta + b_i^{\tau_t} \theta - b_i^\sigma + c_i^{\tau_t}) \sin \theta + (a_i^\sigma(\theta^2 - 2) + 2a_i^{\tau_t} \theta + b_i^\sigma \theta + b_i^{\tau_t} + c_i^\sigma) \cos \theta \right] \Bigg|_{\theta=u_i}^{\theta=l_i} \quad (2.42)$$

The vertical force is calculated as follows:

$$\tilde{F}_z = rb \sum_{i=f,r} \left[(a_i^\sigma(\theta^2 - 2) + 2a_i^{\tau_t} \theta + b_i^\sigma \theta + b_i^{\tau_t} + c_i^\sigma) \sin \theta + (-a_i^{\tau_t}(\theta^2 - 2) + 2a_i^\sigma \theta - b_i^{\tau_t} \theta + b_i^\sigma - c_i^{\tau_t}) \cos \theta \right] \Bigg|_{\theta=u_i}^{\theta=l_i} \quad (2.43)$$

The roll moment is calculated as follows:

$$\tilde{M}_x = -r^2 b \sum_{i=f,r} \left[a_i^{\tau_l} (\theta^2 - 2) \sin \theta + 2a_i^{\tau_l} \theta \cos \theta + b_i^{\tau_l} \theta \sin \theta + b_i^{\tau_l} \cos \theta + c_i^{\tau_l} \sin \theta \right] \Bigg|_{\theta=u\theta_i}^{\theta=l\theta_i} \quad (2.44)$$

The resistance torque is calculated as follows:

$$\tilde{M}_y = r^2 b \sum_{i=f,r} \left[a_i^{\tau_t} \theta^3 / 3 + b_i^{\tau_t} \theta^2 / 2 + c_i^{\tau_t} \right] \Bigg|_{\theta=u\theta_i}^{\theta=l\theta_i} \quad (2.45)$$

The yaw moment is calculated as follows:

$$\tilde{M}_z = -r^2 b \sum_{i=f,r} \left[-a_i^{\tau_l} (\theta^2 - 2) \cos \theta + 2a_i^{\tau_l} \theta \sin \theta - b_i^{\tau_l} \theta \cos \theta + b_i^{\tau_l} \sin \theta - c_i^{\tau_l} \cos \theta \right] \Bigg|_{\theta=u\theta_i}^{\theta=l\theta_i} \quad (2.46)$$

2.6 Terramechanics-based model

By solving Eqs. (2.41), (2.42), (2.41), (2.44), (2.45), (2.46) an evaluation of wheel-soil interaction mechanics can be performed. However, in order to obtain a realistic result, the wheel sinkage must be estimated.

Therefore, to realize a complete terramechanics-based model (TBM), two main blocks are needed. As shown in Fig. 2.1 on page 20, TBM is composed by the wheel-soil interaction model block connected to the entry angle estimator block. By providing them kinematic info (s , β) and wheel normal load W , these two blocks thus are able to calculate all forces/torques acting on the wheel.

Finally, TBM can be used to simulate several scenarios. Three typical soils with different sinkage exponents are chosen, their physical properties and the smooth wheel's geometry parameters are given in Tables 2.1 and 2.2.

Other parameters used in simulation are given instead in Table 2.6. The slip angle coefficient β used in this simulation is opposite to Eq. (2.2), and its simulated values spreading from 5 deg to 30 deg. Parameter j_{max1} is the shear deformation limit used for sandy loam and dry sand, while j_{max2} is referring to clayey soil.

2.6.1 Estimation of entry angle

As discussed before, wheel sinkage has a crucial role in the wheel-soil interaction mechanics, therefore it is needed a method able to estimate it for different operating conditions (slip ratio, wheel velocity).

The entry angle θ_f is geometrically related to wheel sinkage h_f from Eq. (2.12), hence for convenience, the estimation of θ_f is directly performed.

Table 2.6: Parameters used for simulation

Parameter [unit]	Description	Value
W [kg]	Wheel normal load	6
ω [rad/s]	Angular velocity	0.4
s [-]	Slip ratio	0 to 1
β [deg]	Slip angle	(5,10,15,20,25,30)
θ_r [deg]	Exit angle	0
θ_m [deg]	Maximum normal stress angle	$(a_0 + a_1 s) \theta_f$
a_0 [-]	Coefficient for θ_m	0.2
a_1 [-]	Coefficient for θ_m	0.3
j_{max1} [m]	Shear deformation limit	0.020
j_{max2} [m]	Shear deformation limit	0.009

Unfortunately, it is impossible to find an explicit-form solution of the entry angle by using the quadratic approximation model or the original nonlinear model [18]. In the following, it is introduced an algorithm to numerically evaluate θ_f .

The sequence of instructions performed by the entry angle estimator is given as follows:

1. Input soil data, wheel data and contact geometry data. (These values are maintained constant during the following procedure)
2. Input the normal load W of the wheel, slip ratio s , and slip angle β
3. Calculate the static sinkage as function of vertical load W by applying Bekker's formula (2.8)
4. Determine the static entry angle from Eq. (2.10)
5. Calculate \tilde{F}_z by applying (2.43)
6. Equation $W = \tilde{F}_z$ is satisfied?
 - Yes. Then go to the next step
 - No. Then:
 - (a) If $\tilde{F}_z < W$. Increase θ_f until $W = \tilde{F}_z$ is satisfied
 - (b) If $\tilde{F}_z > W$. Decrease θ_f until $W = \tilde{F}_z$ is satisfied
7. Output the evaluated θ_f

In Fig. 2.18 are shown the estimated entry angles θ_f against wheel slip for three different soil types calculated by means of the procedure illustrated in Fig. 2.17. The slip angle is keeping as a constant value ($\beta = 15 \text{ deg}$).

Numerical evaluation is performed by means of MATLAB/Simulink[®] software, where *fit()* function has been used to obtain an interpolation of simulated data. Notice that θ_f decreases along with the slip ratio; this is expected because entry angle and therefore wheel sinkage has its minimum at $s = 1$ (wheel stopped condition). In fact, from Eq. (2.1), when slip ratio is equal to 1, the longitudinal velocity v_x is equal to zero.

2.6.2 Drawbar pull results

Simulation results of the drawbar pull are given for six different slip angles and three different soil types. However no changes in curve slopes has been detected by varying the slip angle. Therefore, as shown in Figs. 2.19, graphs are referring to drawbar pull only for a slip angle ($\beta = 15 \text{ deg}$).

Notice that the drawbar pull increases with the slip ratio, due to the increasing shear deformation in the longitudinal direction. However, it stops to increase once the wheel slip ratio exceeds a certain limit, because of the saturation of the shear deformation. This phenomenon is well-represented by the proposed model, in which the shear deformation is constrained within $(j(\theta), j_{max})$ by Eq. (2.16).

As defined in Eq. (2.23), the drawbar pull is a net traction force, which is a force generated by shearing motion minus a traction load due to normal stress. Therefore, by increasing the slip angle, the shearing motion in the longitudinal direction should decrease. However, as detected from simulations, drawbar pull is not greatly affected by slip angle variation. This means that when F_x is less than zero, shear stress contribution is irrelevant respect than normal stress contribution.

Drawbar pull results in dry sand soil show that the wheel is not able to produce a positive net traction force. This happens because of the high wheel sinkage estimated at this condition. Therefore, this suggests that the chosen wheel is not correctly sized and that its weight is too heavy to traverse this kind of soil.

2.6.3 Side force results

In this simulation, both the bulldozing resistance and the lateral force due to shear stress are evaluated to calculate the side force. F_y graphs are given for six different slip angles and three different soil types as shown in Figs. 2.20, 2.21 and 2.22. Bekker [3] formula (2.26) to calculate bulldozing resistance is used.

Notice that the side force decreases along with the slip ratio and increases according to the slip angle. This happens because the lateral force is dependent on the lateral shear deformation. In fact, the larger the slip angle, the larger is the lateral velocity on the wheel; this leads then to a larger lateral force.

Lateral force has its maximum value at $s = 0$; this is because the lateral shear deformation, expressed in Eq. 2.14, is function of slip ratio and it decreases when slip ratio increases.

While lateral force is function of τ_l and β , bulldozing resistance is strictly dependent on wheel sinkage and it is not sensitive to slip angle change. Therefore, when wheel sinkage is relatively small respect than wheel radius, the bulldozing resistance contribute to the side force is irrelevant. However, as in F_x results, wheel sinkage greatly affects the side force results in dry sand soil. As shown in Fig. 2.21, the bulldozing resistance is too high, thus wheel at this condition is not able to perform steering maneuvers.

2.6.4 Other forces/torques estimation

For completeness are illustrated and discussed the other forces and torques which contribute to the motion of a wheel on a deformable soil. As discussed before, the slip angle does not affect the longitudinal motion of the wheel, hence the simulation values refer only to a single angle ($\beta = 15$).

The vertical force F_z is function of both normal pressure that soil applies toward wheel and shear stress caused by the wheel rotation. As discussed in section 2.6.1, F_z must be set equal to wheel normal load in order to evaluate θ_f . Anyway, the vertical force calculated by iterations presents fluctuations around the mean value due to the tolerance of the model. In Fig. 2.21 are plotted results obtained from iterations, while in Table 2.7 are given root-square-mean errors and mean-absolute errors by considering the wheel weight W as reference. To perform the iterative research a `while()` cycle is used with absolute tolerance of 0.05 Newton.

Table 2.7: F_z mean errors

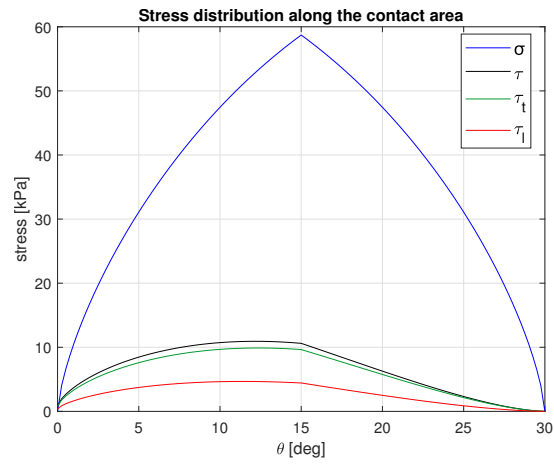
Soil type	F_z [N]	
	RMSE	MAE
Sandy loam	0.0254	0.0177
Dry sand	0.0172	0.0082
Clayey soil	0.0252	0.0196

The resistance torque M_y is a function of longitudinal shear stress only, therefore it is not affected by slip angle changes. As shown in Fig. 2.24, resistance torque is growing along with the slip ratio.

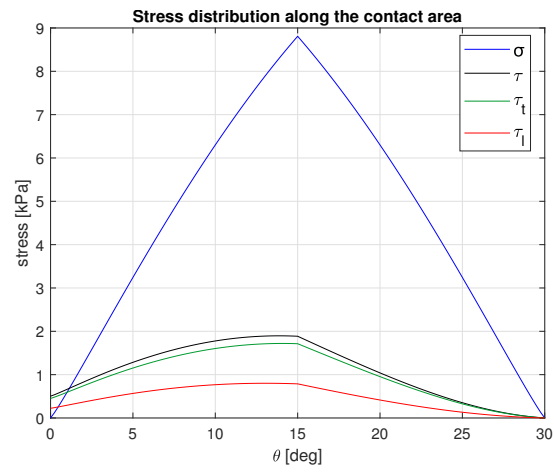
The roll moment M_x depends on lateral shear stress only, therefore is influenced by slip angle. This moment does not have any effect on this simulation because of the assumptions made at the beginning of the chapter. However, it can be useful for a 4-DOF vehicle dynamics simulation. In Fig. 2.25 is shown the roll moment

against wheel slip on sandy loam with slip angle equal to 15 deg.

The yaw moment M_z also depends only on lateral shear stress. Notice that, as in side force case, yaw moment increases in line with slip angle and decreases by increasing slip ratio. In Fig. 2.26 are shown graphs of simulated results of M_z for different slip angles.



(a) Sandy loam



(b) Dry sand



(c) Clayey soil

Figure 2.11: Stress distribution for smooth wheel traveling on different soil types

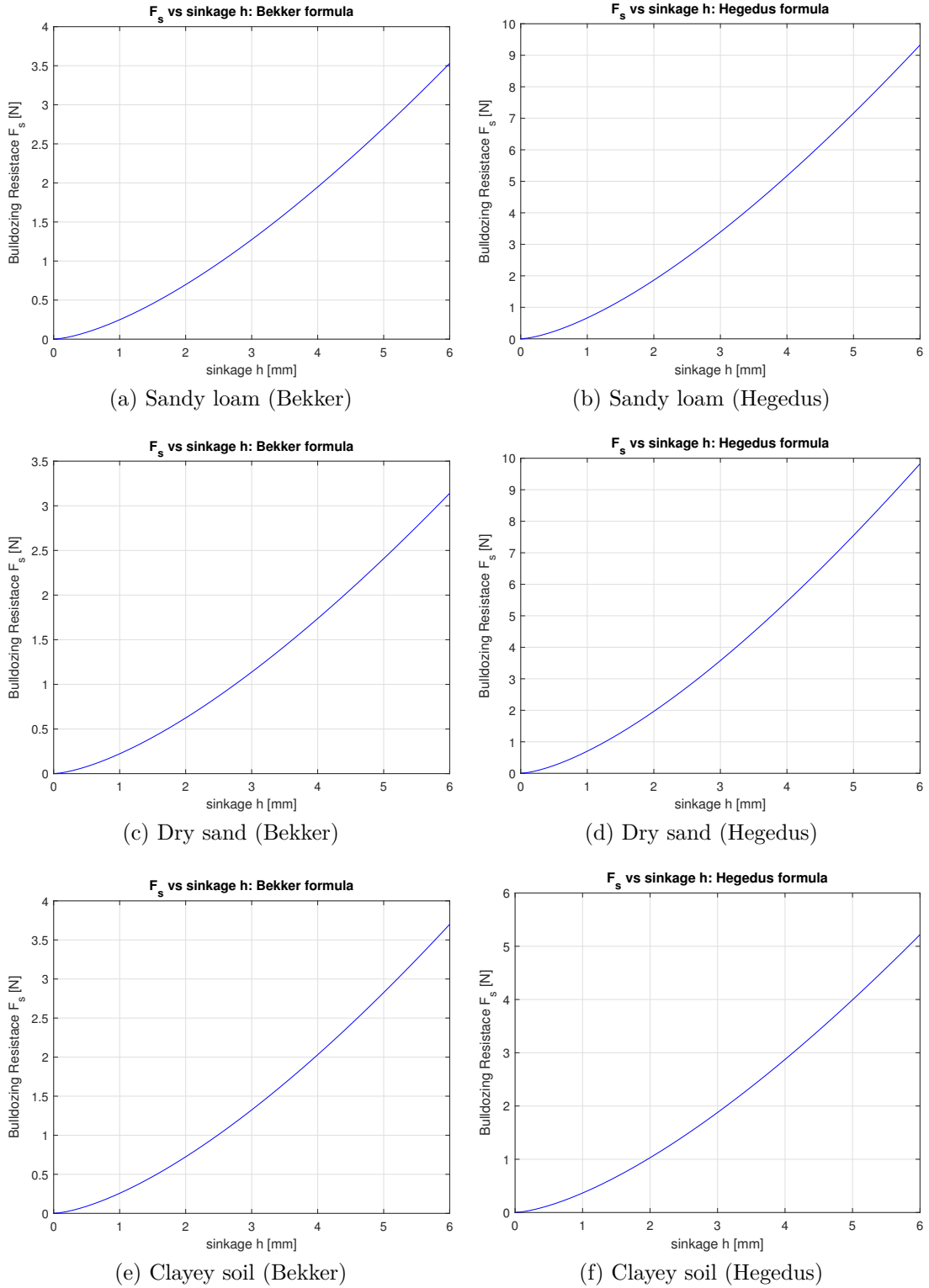


Figure 2.15: Bulldozing resistance vs wheel sinkage for three different soil types ($r=92$ mm; $b=107$ mm)

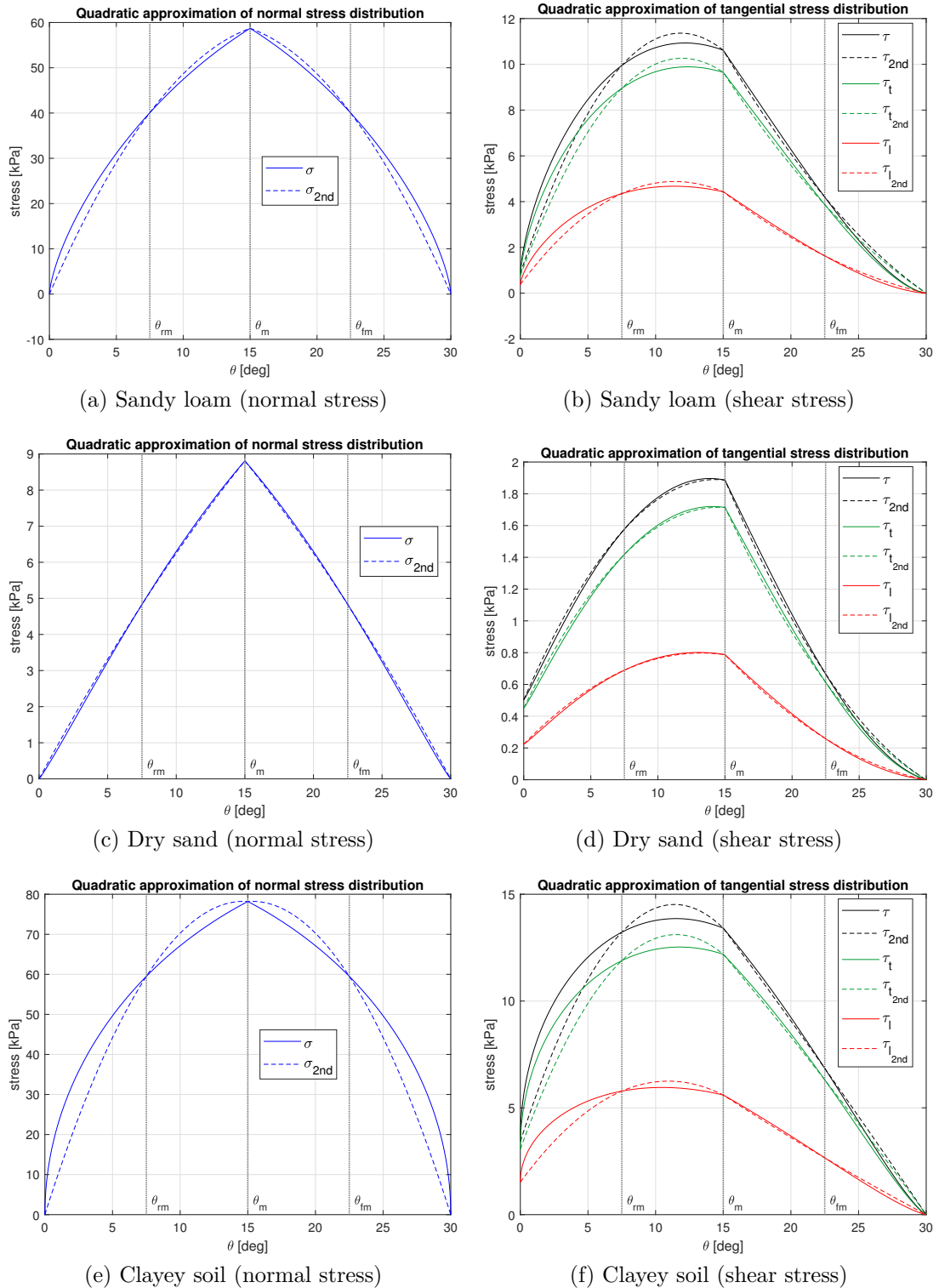


Figure 2.16: Quadratic approximation of stresses along the contact area

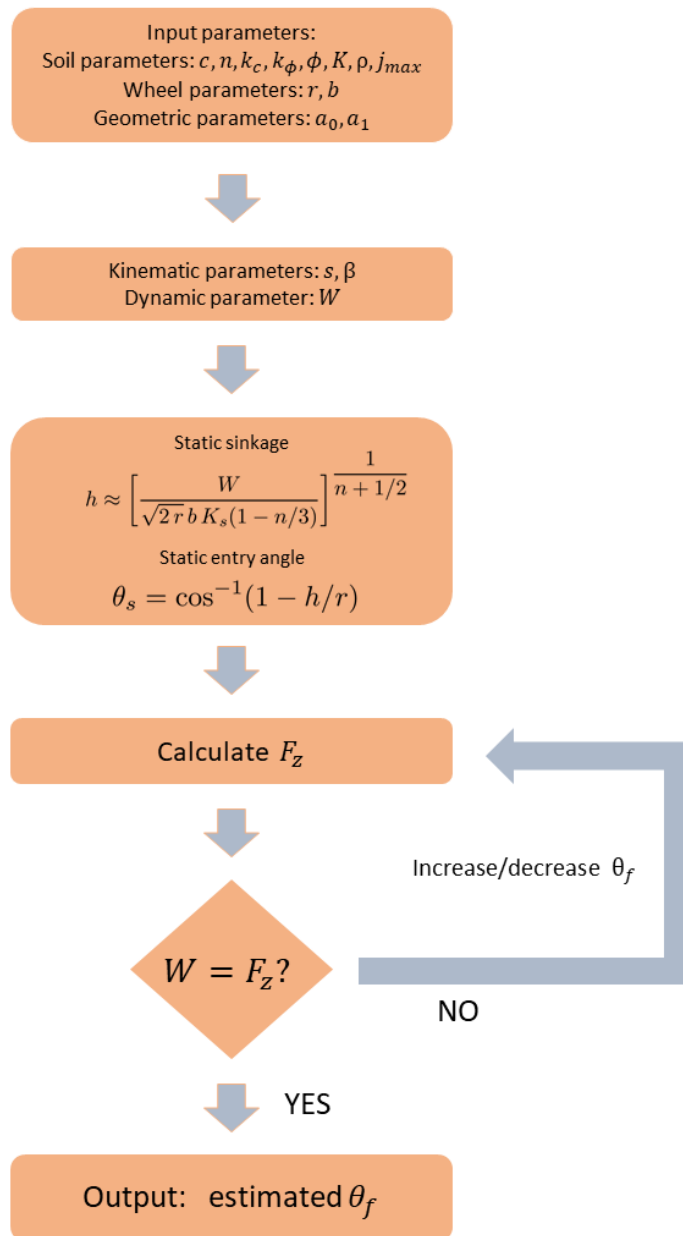
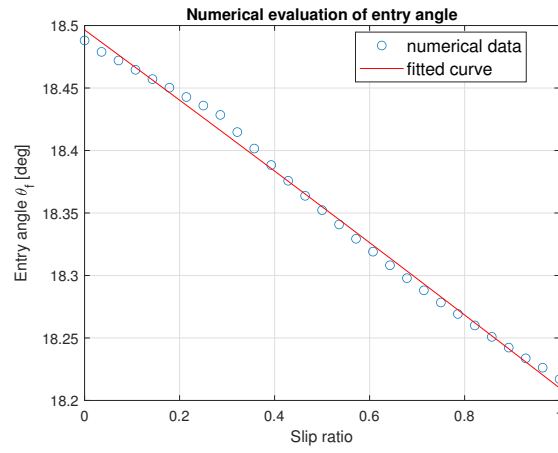
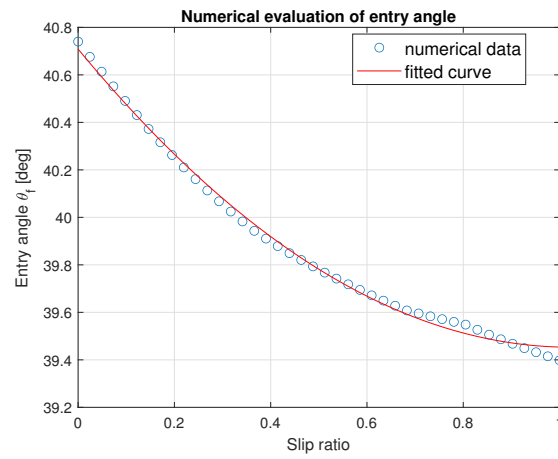


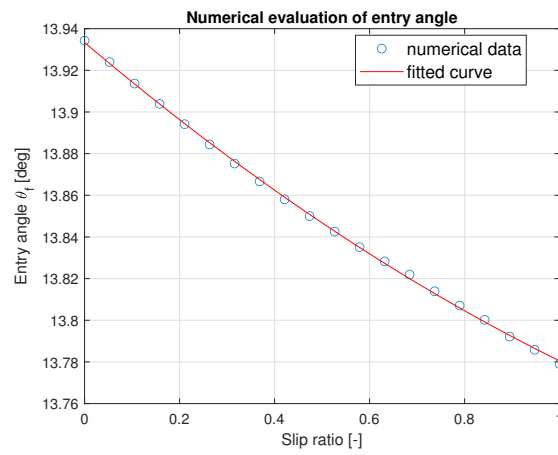
Figure 2.17: Flowchart of entry angle estimation algorithm



(a) Sandy loam

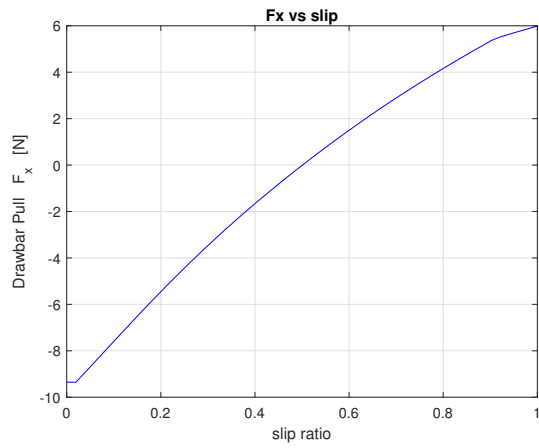


(b) Dry sand

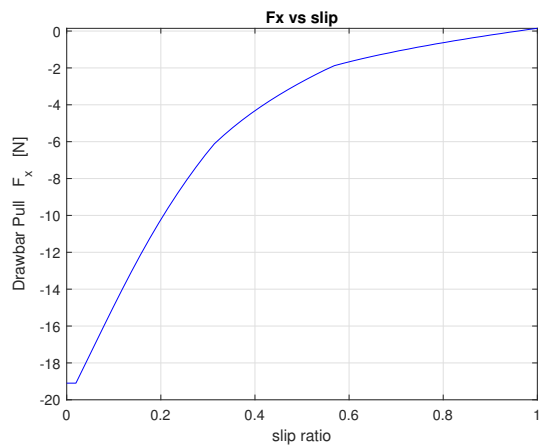


(c) Clayey soil

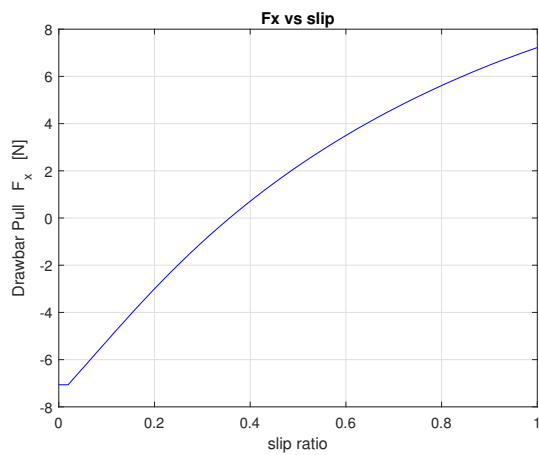
Figure 2.18: Computed entry angle vs slip ratio



(a) Sandy loam

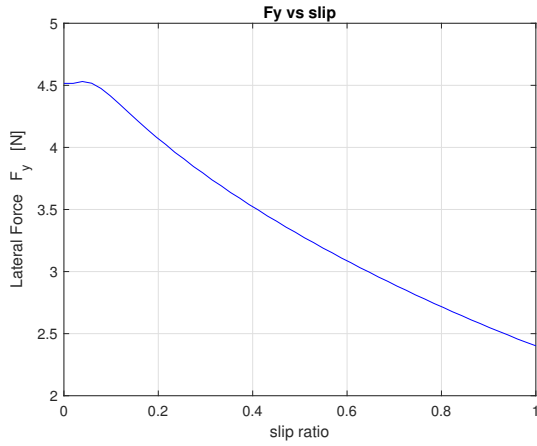


(b) Dry sand

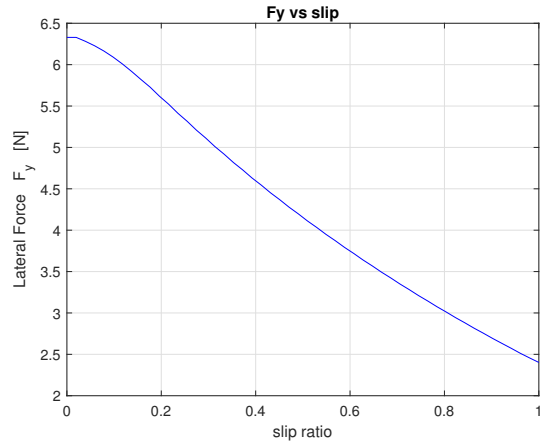


(c) Clayey soil

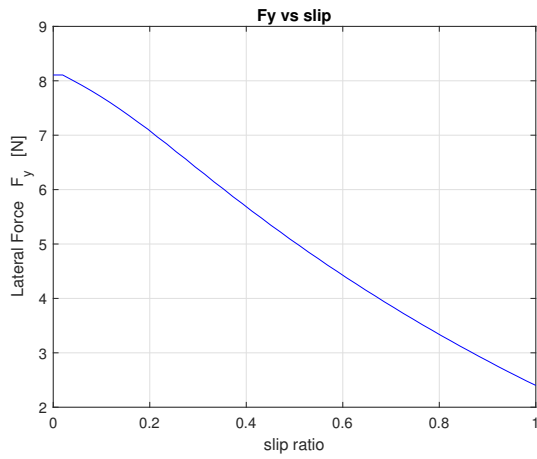
Figure 2.19: Drawbar pull along the slip ratio for three different soil



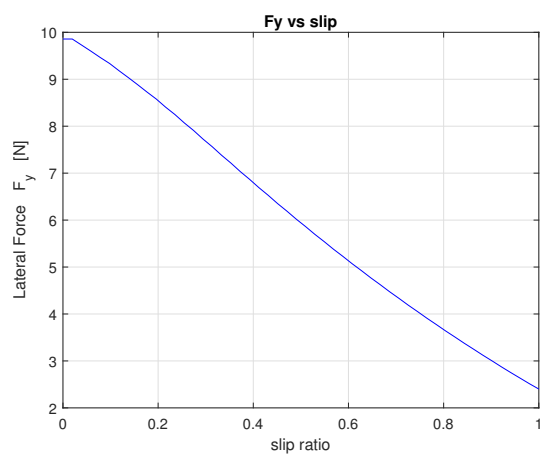
(a) Slip angle = 5 deg



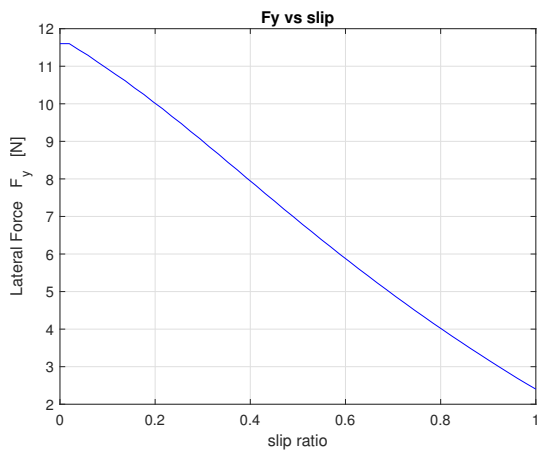
(b) Slip angle = 10 deg



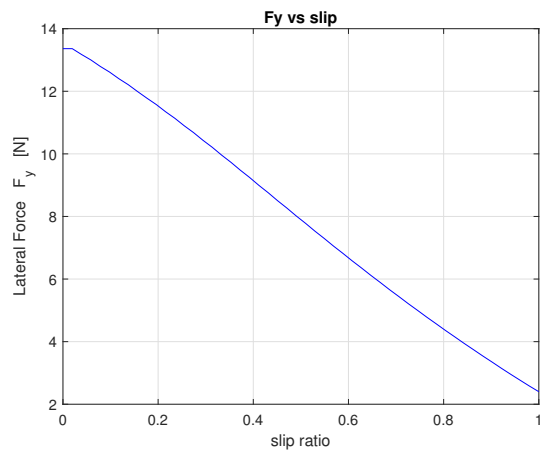
(c) Slip angle = 15 deg



(d) Slip angle = 20 deg

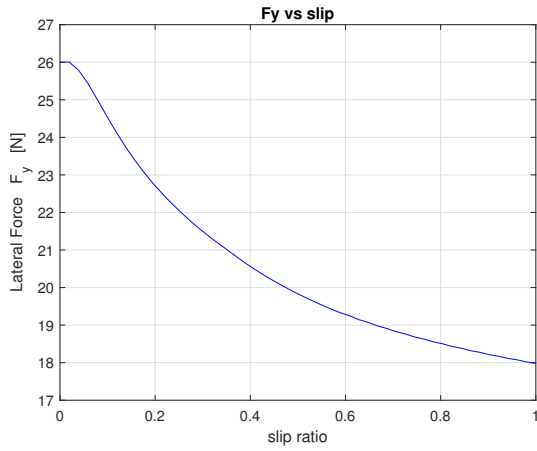


(e) Slip angle = 25 deg

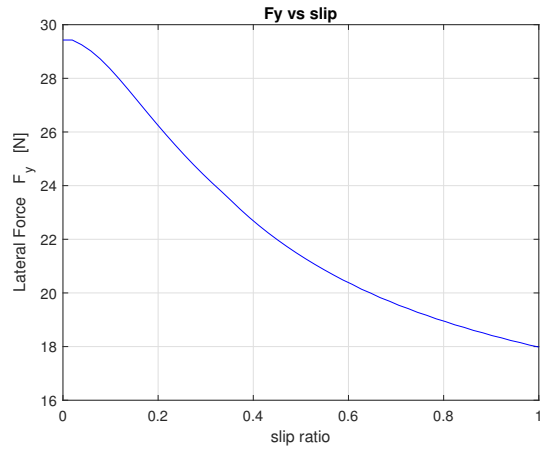


(f) Slip angle = 30 deg

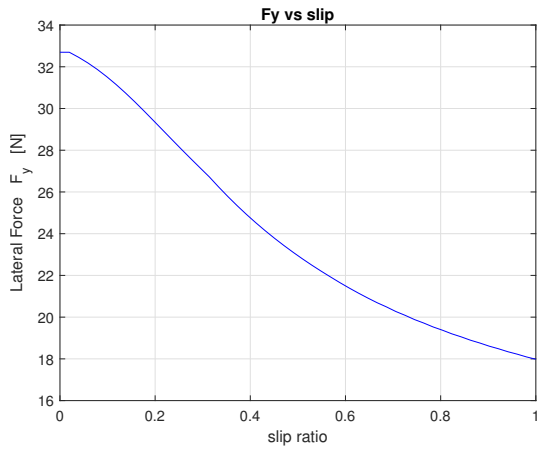
Figure 2.20: Sandy loam: lateral force vs slip ratio simulated at different slip angles



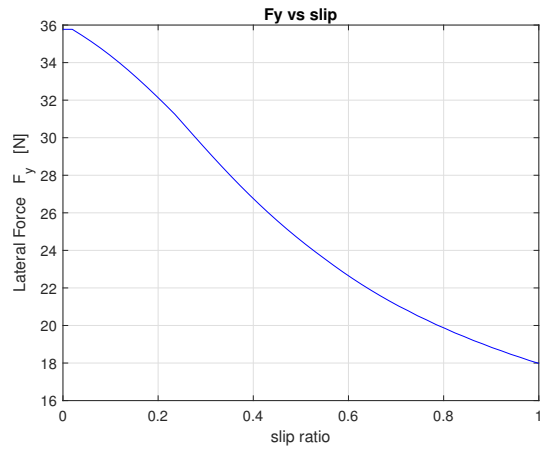
(a) Slip angle = 5 deg



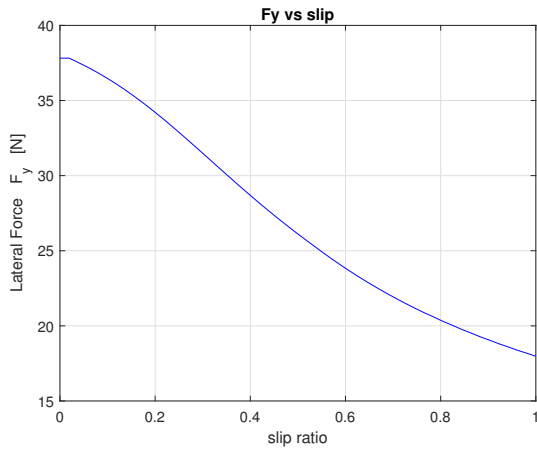
(b) Slip angle = 10 deg



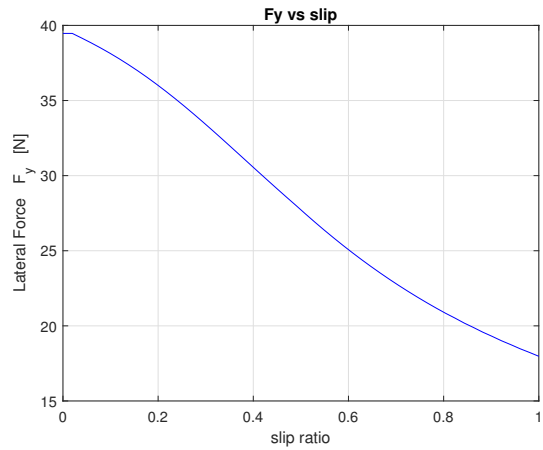
(c) Slip angle = 15 deg



(d) Slip angle = 20 deg

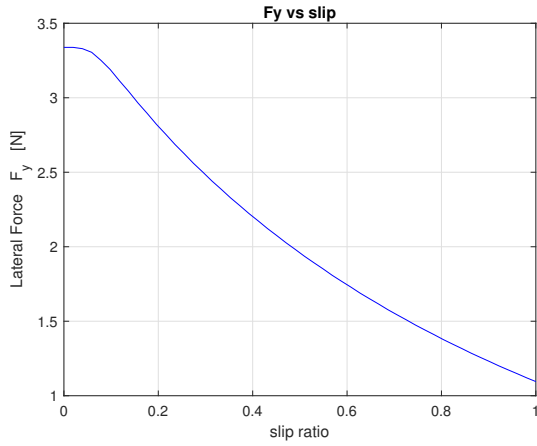


(e) Slip angle = 25 deg

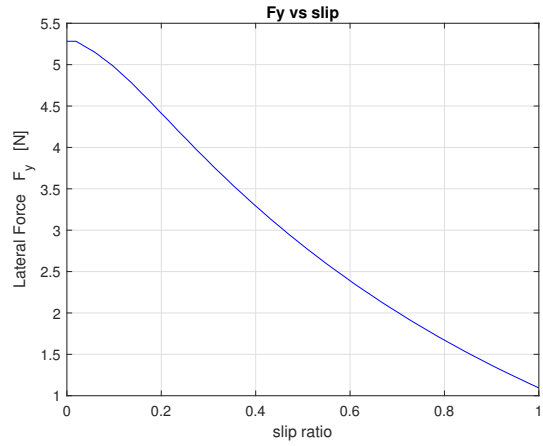


(f) Slip angle = 30 deg

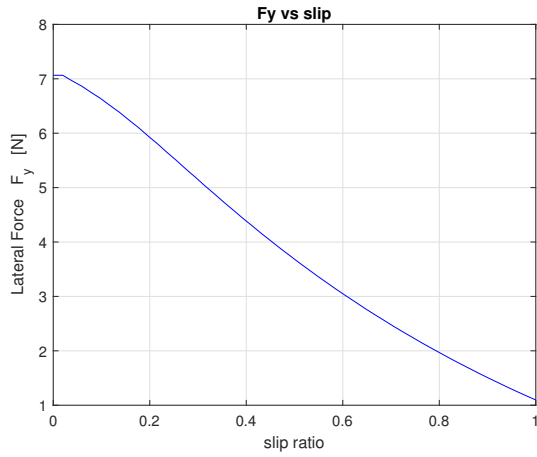
Figure 2.21: Dry sand: lateral force vs slip ratio simulated at different slip angles



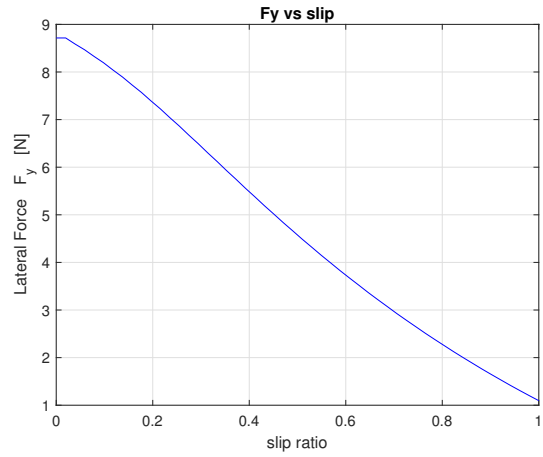
(a) Slip angle = 5 deg



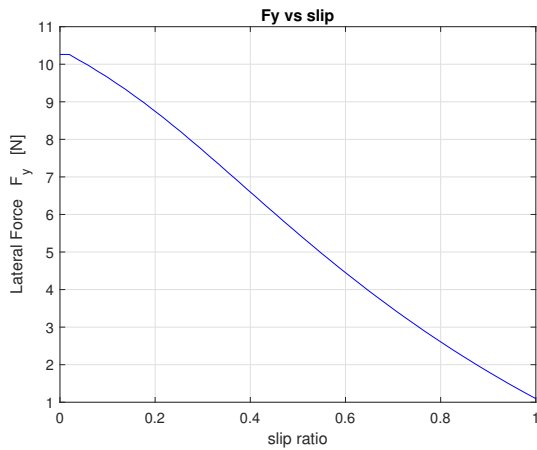
(b) Slip angle = 10 deg



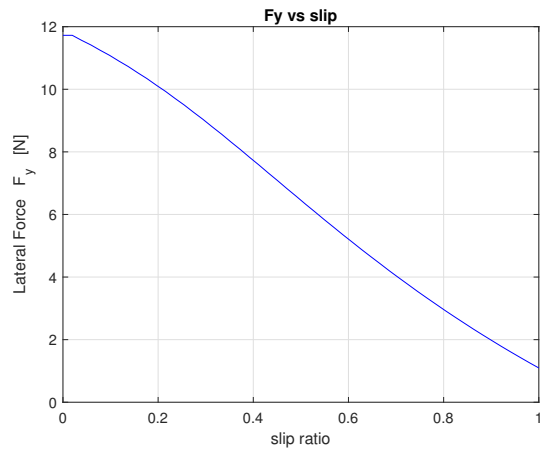
(c) Slip angle = 15 deg



(d) Slip angle = 20 deg



(e) Slip angle = 25 deg



(f) Slip angle = 30 deg

Figure 2.22: Clayey soil: lateral force vs slip ratio simulated at different slip angles

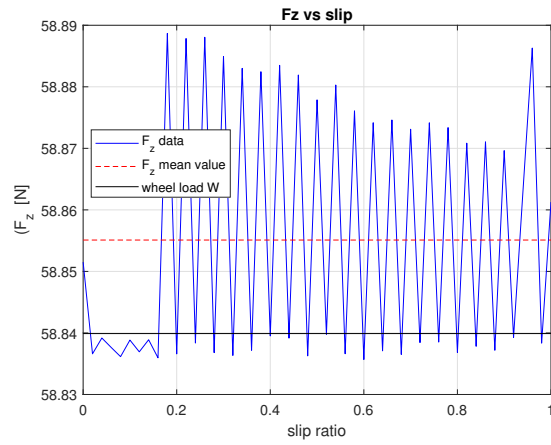


Figure 2.23: Results of vertical force for sandy loam terrain

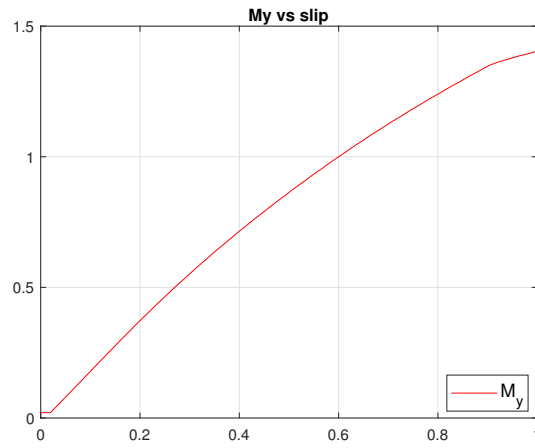


Figure 2.24: Resistance torque results for sandy loam terrain

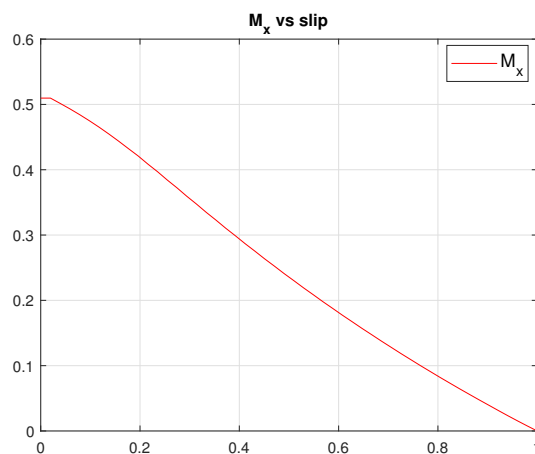


Figure 2.25: Roll moment results for sandy loam terrain

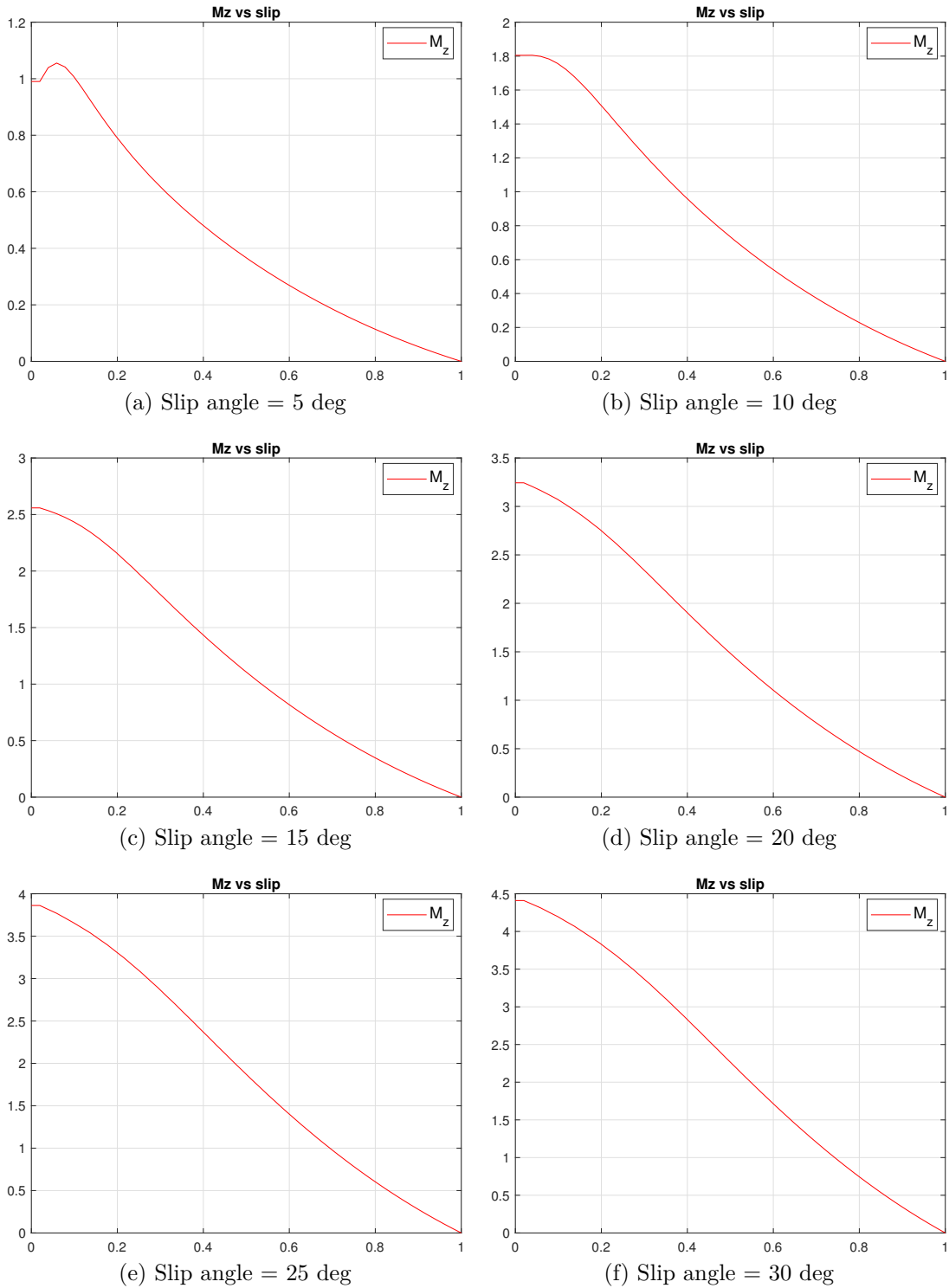


Figure 2.26: Sandy loam: yaw moment vs slip ratio simulated at different slip angles

Chapter 3

Vehicle Dynamics

3.1 Introduction

In this chapter, the motion dynamics of the vehicle is investigated, hence a simplified vehicle model by means of multibody system approach (MBS) is developed. The motion dynamics of the vehicle consists of two models. One is the terramechanics-based model described in chapter 2 to calculate contact forces and torques exchanged by each wheel and the robot. The other one is the vehicle dynamics model able to calculate motion dynamics of its chassis due to the wheel-soil interaction.

Firstly, a brief introduction of the target modeled vehicle is given. Then, the MBS approach is defined and the vehicle's chassis used in simulation is described specifying its own dynamical parameters.

Further, the simulation procedure is explained for different cases. In particular, two typical scenarios are analyzed: straight line motion and turning motion on horizontal plane.

Finally, the dynamics simulations results using the proposed model are discussed.

3.2 Target vehicle

As discussed in chapter 1, the target vehicles of this thesis are UGVs used in agricultural applications. However, these kind of robots can be differently designed on the basis of their specific application. Unfortunately, it has not been possible to perform experiments using a test bed vehicle. Therefore, a four-wheel-drive (4WD), four-wheel-steering (4WS) mobile robot, as illustrated in Fig. 3.1, is arbitrarily chosen as an example that can be applied in agricultural operations.

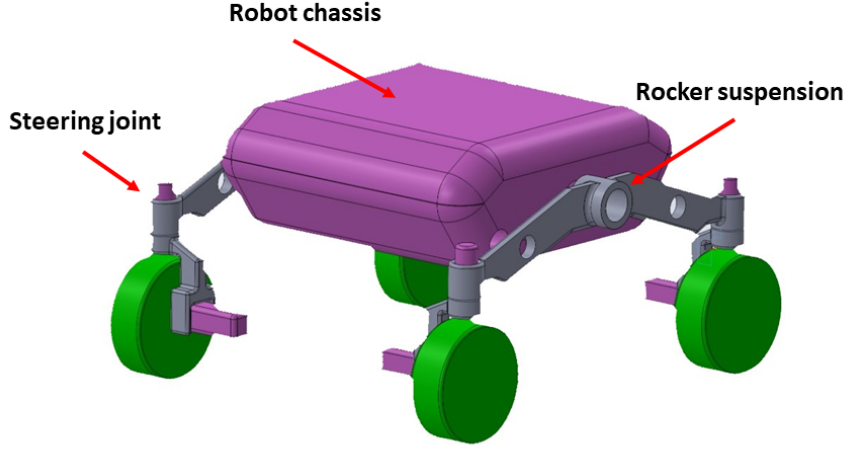


Figure 3.1: Simplified CAD model of a 4WD/4WS mobile robot

3.3 Wheeled-mobile robot dynamics model

In this section, the mobile robot mechanics is considered as similar to the test bed rovers used in [15, 18].

The vehicle is a four-wheeled mobile robot, where each wheel is powered by a motor and has active steering degree of freedom (DOF). It has a differential mechanism, which is connected to two free-pivot rocker suspensions. The rocker suspension is a non-spring passive suspension mechanism that connects the wheels by free-pivot links. This differential mechanism is used to keep the pitch angle of the robot body in the middle of the left and right rocker angles.

As shown in Fig. 3.2, the wheeled robot coordinate system (Σ_0) is defined as a right-hand frame, where the longitudinal direction of vehicle is denoted by x_0 , the lateral direction by y_0 , and the vertical direction by z_0 .

Multibody system approach is used to model the vehicle dynamics. It allows the study of the dynamic behavior of linked rigid bodies [26]. Therefore, the wheeled-mobile robot (WMR) can be modeled as an articulated multibody system.

The motion dynamical equation of the WMR is derived as following:

$$\mathbf{H} \begin{bmatrix} \dot{\mathbf{v}}_0 \\ \dot{\boldsymbol{\omega}}_0 \\ \ddot{\mathbf{q}} \end{bmatrix} + \mathbf{C} + \mathbf{G} = \begin{bmatrix} \mathbf{F}_0 \\ \mathbf{M}_0 \\ \boldsymbol{\tau} \end{bmatrix} + \mathbf{J}^T \begin{bmatrix} \mathbf{F}_e \\ \mathbf{M}_e \end{bmatrix} \quad (3.1)$$

where:

- \mathbf{H} is the inertia matrix of the wheeled-mobile robot;
- \mathbf{C} is the velocity depending term;

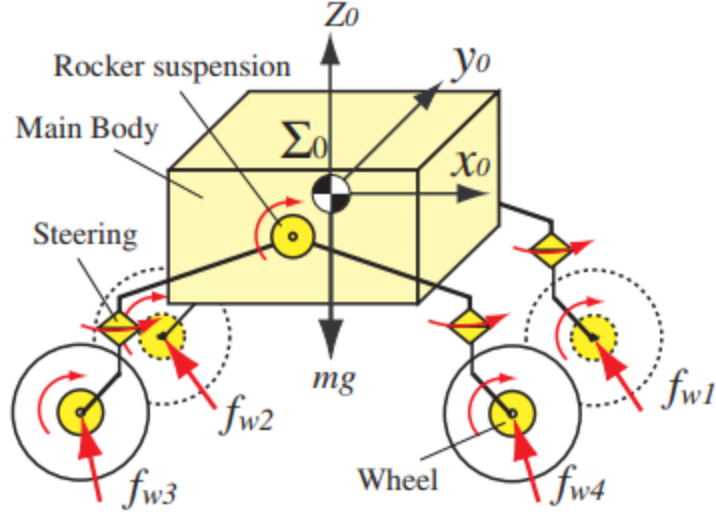


Figure 3.2: Model dynamics of a mobile robot [15]

- \mathbf{G} is the gravity term;
- \mathbf{v}_0 is the translational velocity of the main body;
- $\boldsymbol{\omega}_0$ is the angular velocity of the main body;
- \mathbf{q} is the angle of each joint of the rover;
- $\mathbf{F}_0 = [0,0,0]^T$ are the external forces acting at the center of the main body
- $\mathbf{M}_0 = [0,0,0]^T$ are the external moments acting at the center of the main body
- $\boldsymbol{\tau}$ are the torques acting at each joint of the wheeled-mobile robot;
- \mathbf{J} is the Jacobian matrix
- $\mathbf{F}_e = [f_{w1}, f_{w2}, f_{w3}, f_{w4}]$ are the external forces due to wheel-soil interaction acting at the center of each wheel;
- $\mathbf{M}_e = [M_x, M_y, M_z]$ are the external moments due to wheel-soil interaction acting at the center of each wheel.

3.3.1 Simplified vehicle model

Notice that Eq. (3.1) is a general equation and can be applied to a vehicle with any configuration. Therefore, by using vehicle parameters obtained by means of a 3D-CAD application, it is possible to solve the vehicle equation of motion.

The robot is modeled as a rigid body with 3 degrees of freedom (DOF) where the forces derived from the terramechanics model are applied.

The multibody-system approach is used to perform the vehicle's dynamics simulation by means of the SimMechanics toolbox in MATLAB/Simulink®. The related Simulink project is depicted in Figs. 3.4, and 3.5.

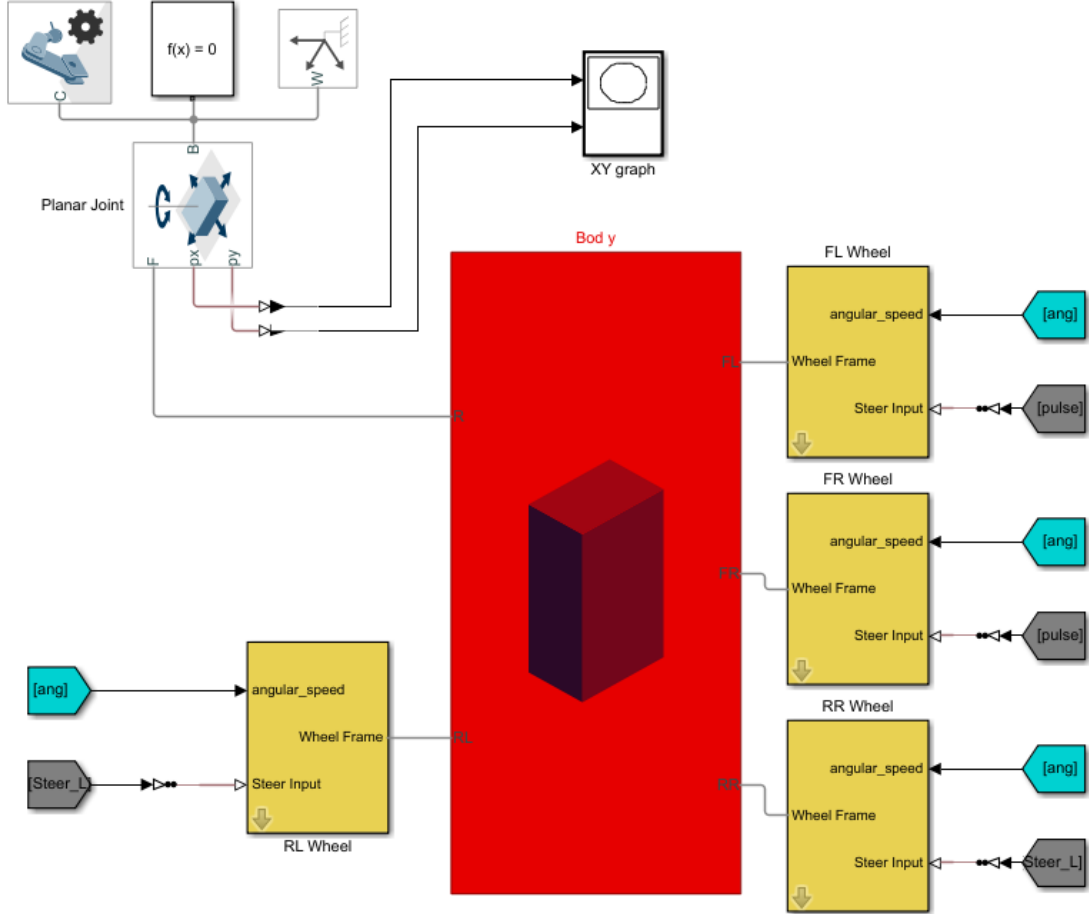


Figure 3.4: SimMechanics vehicle dynamics model

The simulation procedure can be summarized as follows:

1. Initialize the vehicle dynamics model and the terramechanics-based model and set the robot's initial acceleration to zero.
2. Determine the normal load of each wheel by Eq. 3.2.
3. Provide in input the steering angles δ_{ij} and the rotational angular velocities ω_{ij} for each wheel ($i = L, R; j = F, R$). Angular velocity is considered as constant and steering angles are supplied as a pulse signal.

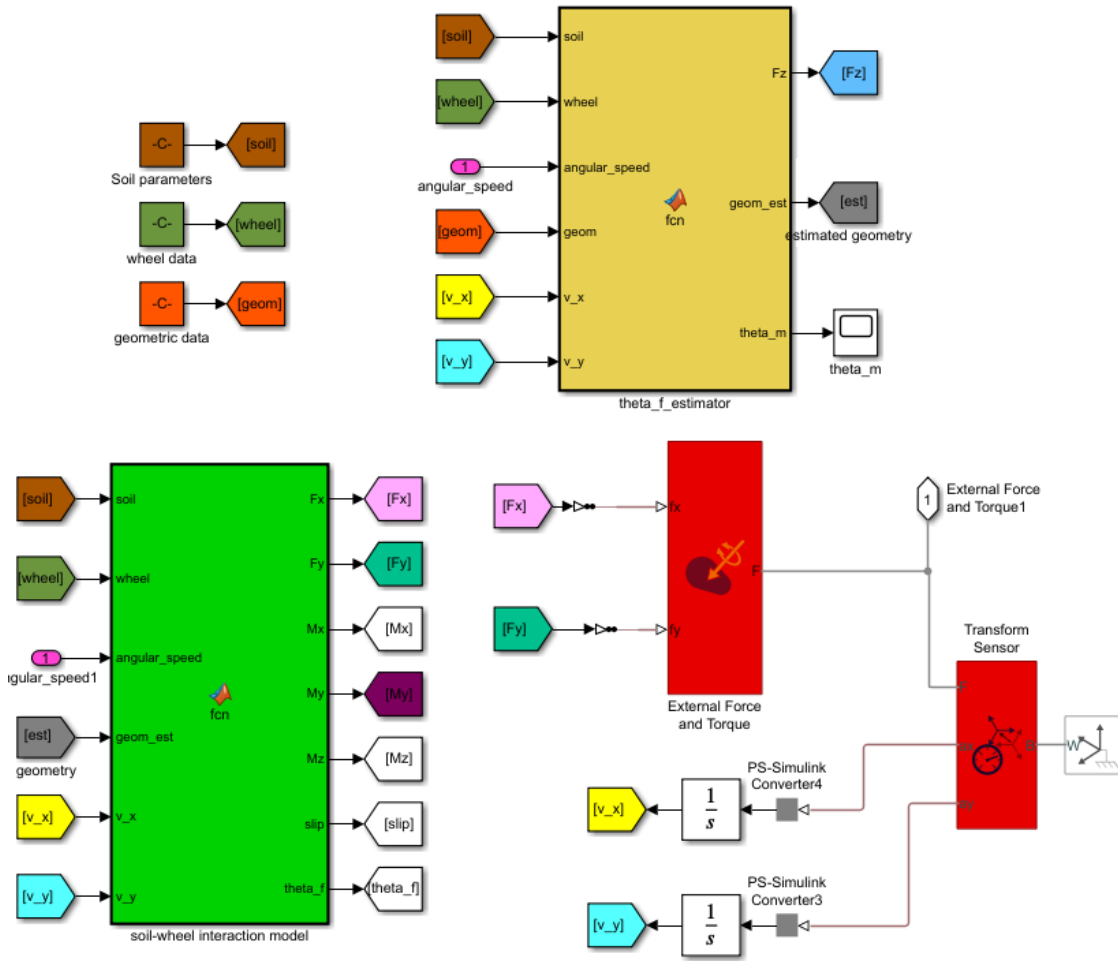


Figure 3.5: Terramechanics-based model

4. Calculate the slip ratios and slip angles and derive the entry angle θ_f by using the entry angle estimator.
5. Derive the forces/torques for each wheel by using the TBM block.
6. Solve Eq. 3.1 to obtain the vehicle's position, orientation, and velocities, then return to step 4.

3.3.3 Simulation results

As mentioned before, two vehicle's motion scenarios are simulated. During the simulation time, vehicle's position, orientation and velocities are analyzed and an

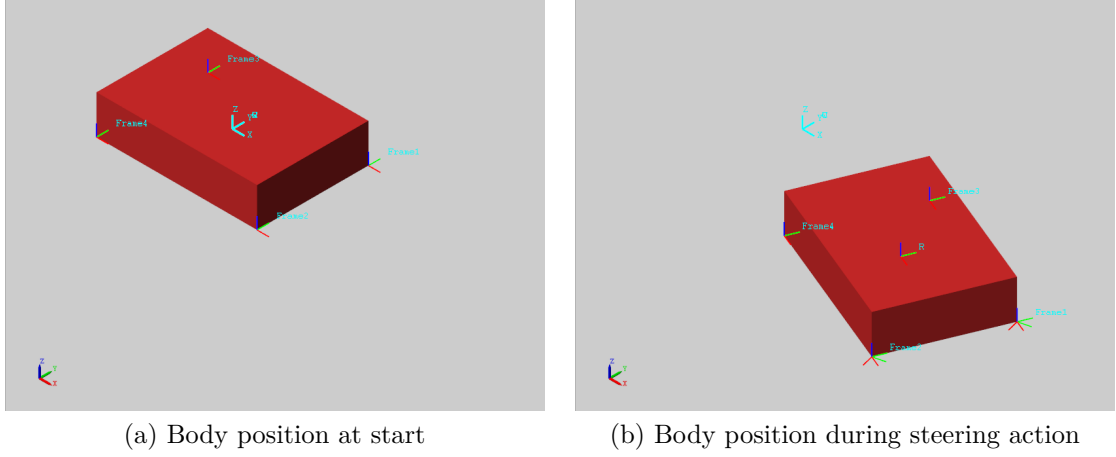


Figure 3.6: Motion simulation of a simplified vehicle model during steering maneuvers (SimMechanics toolbox)

evaluation has been performed in order to verify if they are consistent with provided inputs. The duration time of the simulation is 60 seconds.

The sandy loam parameters of soil, given in Table 2.1, are chosen to reproduce the terrain type where the robot is traveling on, while the operating conditions are given in Table 2.6.

Straight line motion scenario

In Fig. 3.7, the robot position on a plane, where x-axis denotes the longitudinal direction and y-axis denotes the lateral one, is illustrated. As expected, the position of the robot during time simulation is a straight line along with x-axis.

The orientation of the robot is given by the yaw angle (rotation angle around z-axis) of the body reference frame. In this case, it has not been plotted because it is evident that it is equal to zero during the whole simulation, as Fig. 3.7 suggests.

By providing constant angular velocity to each wheel, thus a constant longitudinal velocity of the robot is expected. As shown in Fig. 3.8, except for the transitory phase due to the preset initial conditions, the longitudinal velocity is constant and it is also consistent with the wheel slip ratio displayed in Fig. 3.9.

As shown in Fig. 3.8, the lateral velocity is null.

Steering motion scenario

In this case, a steering motion is performed by providing to the front wheels only an active steering angle. As shown in Fig. 3.10, the input steering angles applied to the four wheels of the vehicle are illustrated.

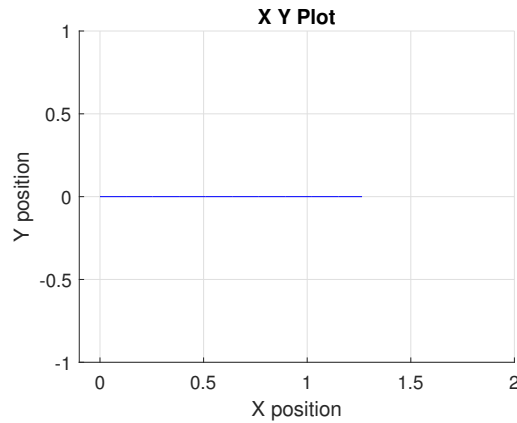


Figure 3.7: Vehicle position in straight line motion scenario

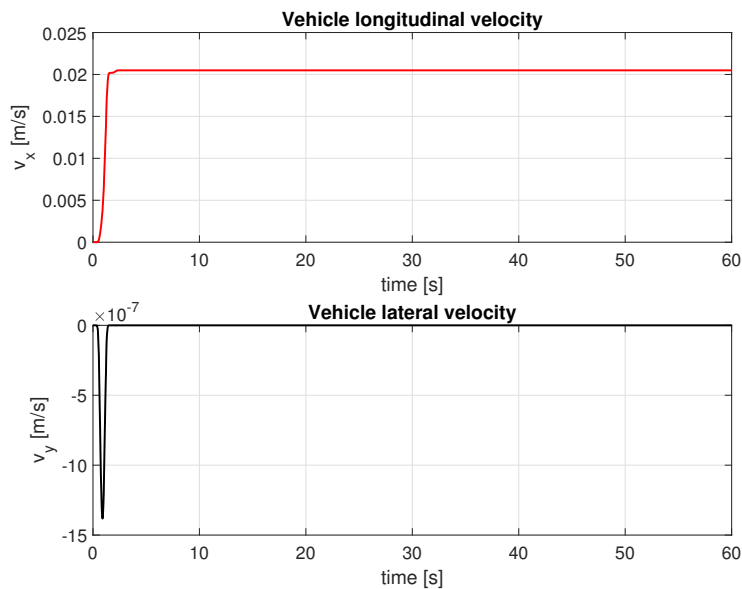


Figure 3.8: Vehicle velocities in straight line motion scenario

On the basis of the provided inputs, the position and orientation of the robot are obtained as shown in Fig. 3.11. Notice that both vehicle position and orientation are consistent with the provided steering angles during simulation.

In order to analyze the kinematic behavior of the simulated model the longitudinal velocity and lateral velocity of each wheel are compared with the respective slip ratios calculated from TBM block as shown in Figs. 3.12, 3.13, ??.

Then, as shown in Fig. 3.15, the vehicle's chassis velocities are obtained on the basis of the forces due to the wheel-soil interaction acting on each wheel.

Notice that lateral velocity is negative because the steering angles are intended as opposite to the body system reference frame.

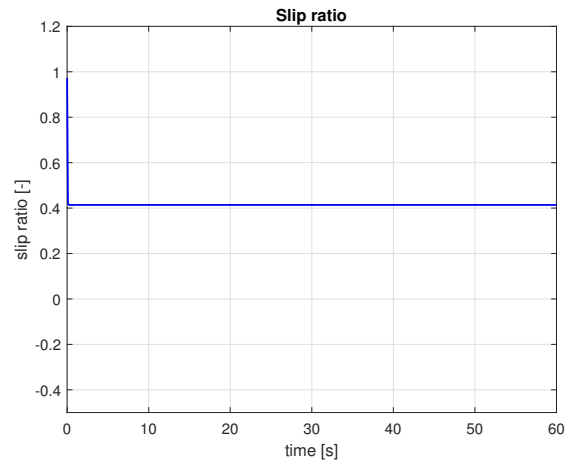


Figure 3.9: Wheel slip ratio in straight line motion scenario

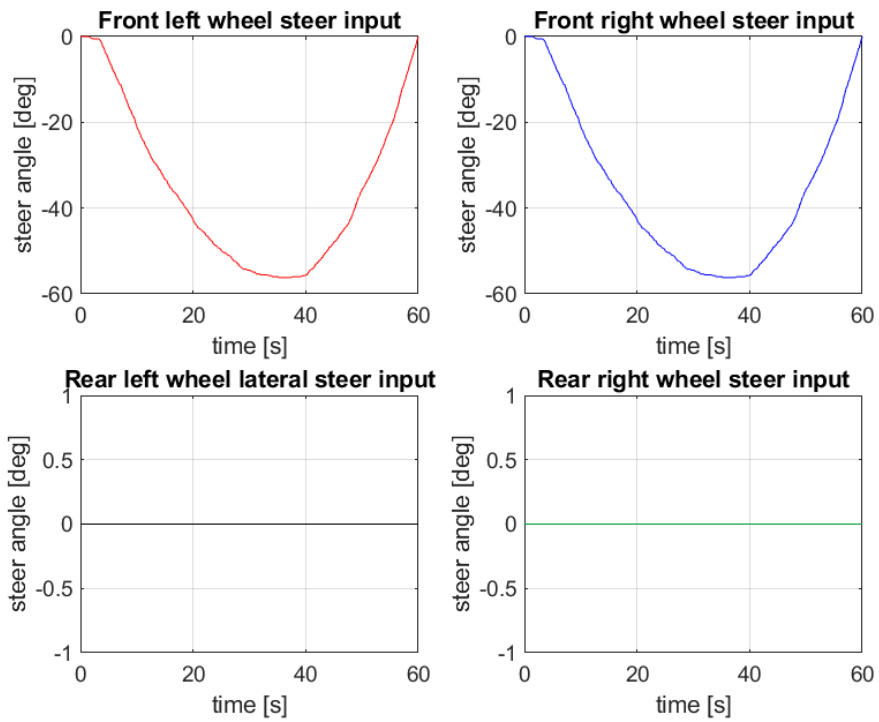
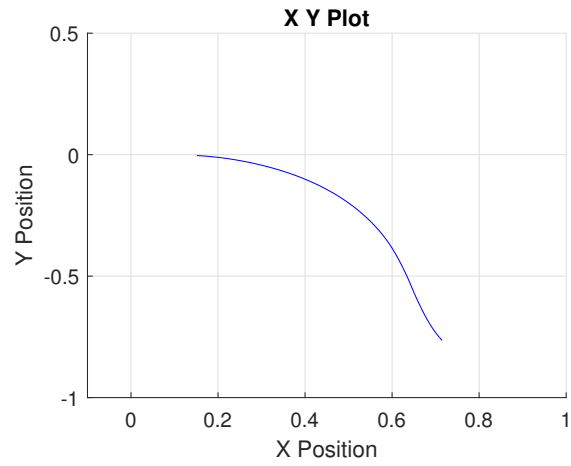
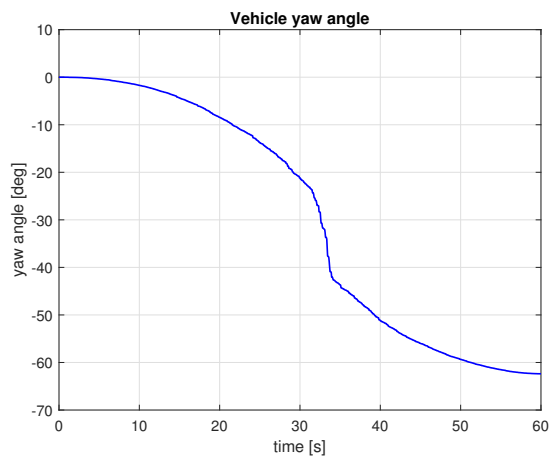


Figure 3.10: Input steering angles applied on each wheel in steering motion scenario



(a) Position



(b) Yaw angle

Figure 3.11: Vehicle position and orientation in steering motion scenario

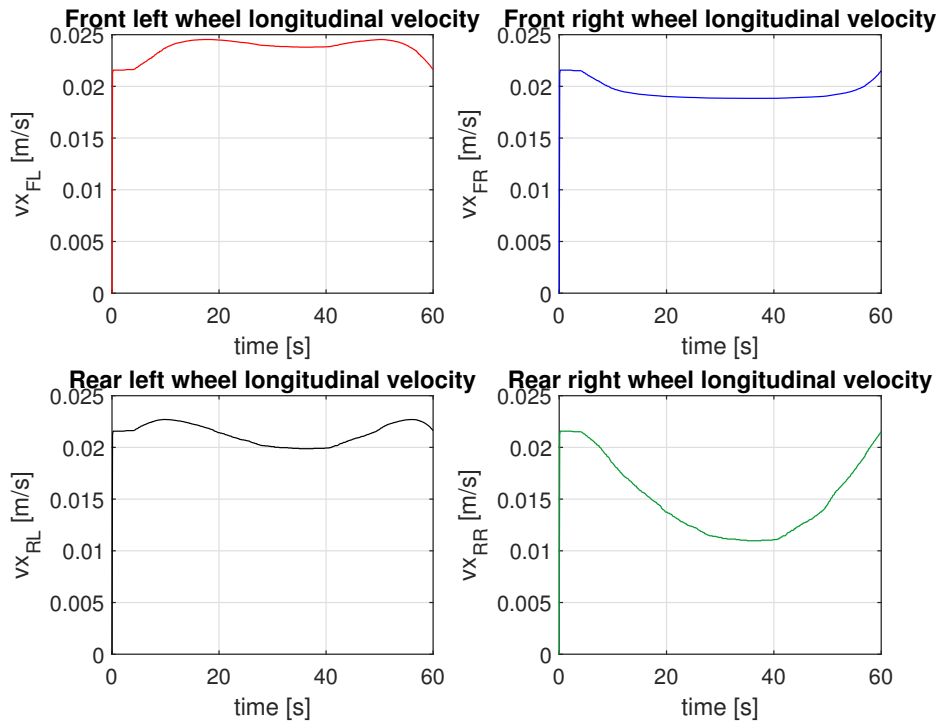


Figure 3.12: Wheel's longitudinal velocities in steering motion scenario

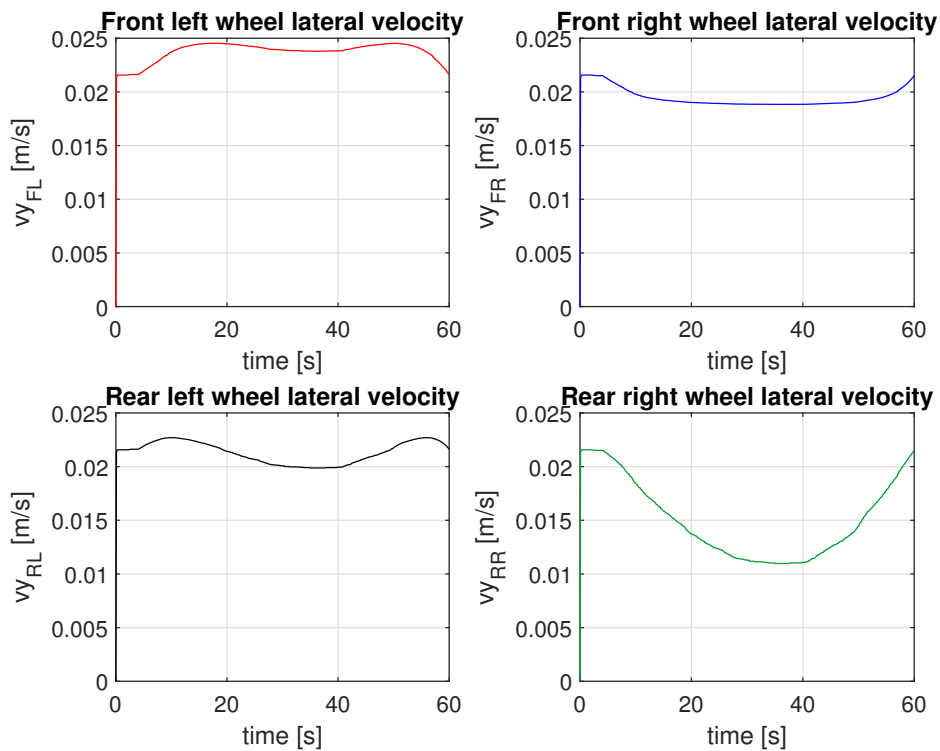


Figure 3.13: Wheel's lateral velocities in steering motion scenario

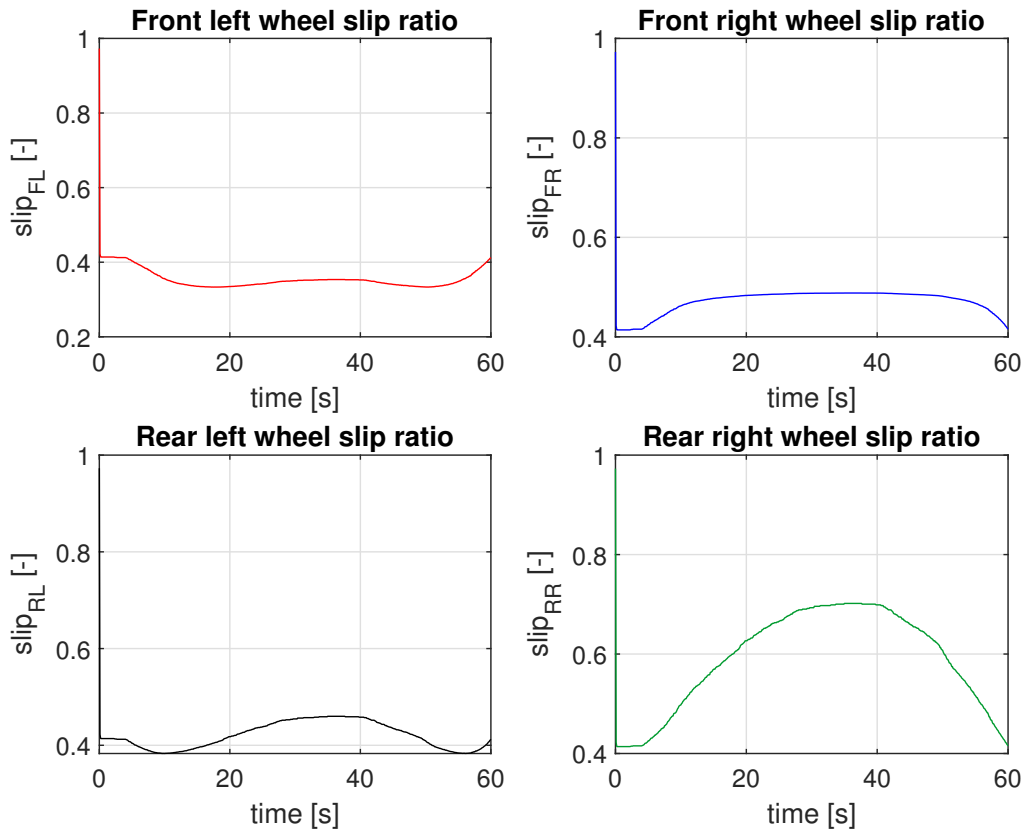


Figure 3.14: Wheel slip ratios in steering motion scenario

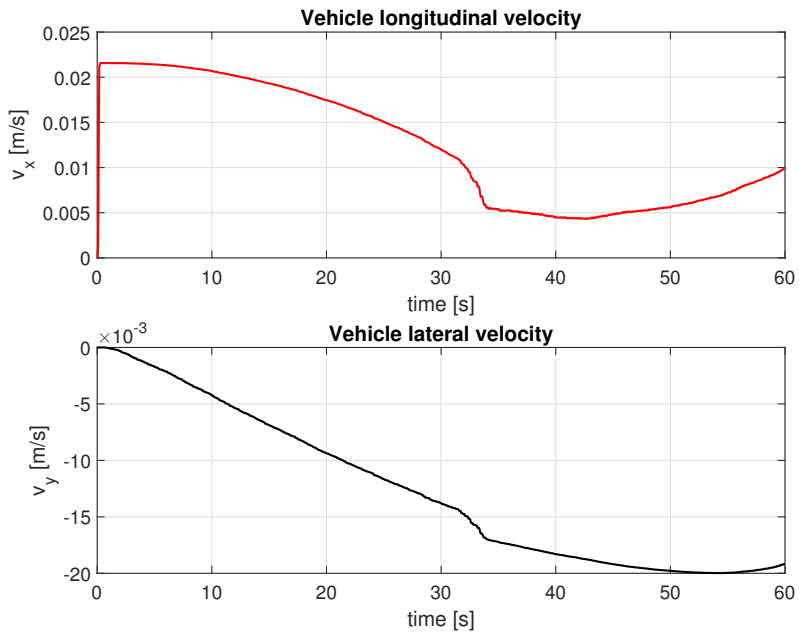


Figure 3.15: Vehicle's velocities in steering motion scenario

Chapter 4

Soil parameters identification

4.1 Introduction

In this chapter an analysis on the model sensitivity to parameters of soil and then a method able to identify them are outlined.

Since the wheel-soil interaction model is highly non-linear and has multi-coupling equations, the control of the vehicle motion encounters difficulties in applying this model in realistic scenarios.

One of the main limitations to the effective use of WMR in agricultural application is their poor performance in terms of traction control, considering also the rough nature of the involved terrains. In this vein, the identification of the terrain characteristics is key to develop the next generation of intelligent WMRs.

In fact, the agricultural terrains have disparate physical characteristics, hence terrain classification using on-board sensors can provide important information regarding tractive efficiency, traction control, traversability prediction and performance optimization of a WMR traveling on unknown terrains.

As explained in chapter 2, from the wheel-soil interaction dynamics, the drawbar pull F_x is strictly affected by the soil parameters.

The drawbar pull is the net force acting on the vehicle's wheels that is required to develop traction control algorithms. Hence, estimating in real time the soil parameters of unknown terrain can be crucial for controlling the vehicle navigation.

Therefore, the soil parameters identification has significantly attracted the interest of many researchers. [25].

The majority of published researches are related to the planetary rover control, because the lack of terrain sampled parameters obtained from the return missions has required soil recognition to be conducted remotely. Nevertheless, on-line estimation of soil parameters is also suitable for WMRs applied in agricultural field.

For the actual requirements of motion control, it is necessary to develop a fast identification method for the unknown terrain parameters.

The methods used by Iagnemma [14] and Hutankabodee [13] have proved their effectiveness in estimating parameters of simplified Bekker-Wong traction models, and they are widely used.

For example, Iagnemma et al. developed a method for on-line estimation of terrain cohesion c and internal friction angle ϕ using on-board rover sensors. The algorithm is based on a simplified model of classical terramechanics equations, and uses a linear least-squares estimator to calculate soil parameters in real time by setting the shearing deformation modulus K to a typical value.

Instead, Hutangkabodee et al. developed a method to identify the internal friction angle ϕ , shearing deformation modulus K , and lumped pressure sinkage coefficient K_s , by keeping the internal cohesion c as constant value. The composite Simpson's rule was applied to achieve an approximated model.

However, wheel-soil interaction models consist of other parameters too, such as sinkage exponent n and geometric parameters a_0 and a_1 used to identify where is located the maximum normal stress along the wheel-soil contact patch as expressed in Eq. (2.18).

In this thesis, a method that relies on L. Ding research [4], suitable for on-line identification of terrain parameters, is developed.

Thus, the algorithm must identify parameters of the terrain which robot is currently traversing. This makes it possible to characterize agricultural soil by estimating terrain parameters according to the forces and moments that act upon the wheel. In this way, the algorithm allows the robot to recognize the variations in soil parameters in time to optimize its control and planning strategy, for example by minimizing power consumption.

In order to achieve a closed-form solution of the model, it is necessary to simplify the complex coupled non-linear integrated equations. Therefore, a decoupled analysis on relevant equations is performed in details in section 4.3.

Instead, in section 4.2, a discussion on terramechanics model sensitivity to soil parameters affecting traction is addressed.

4.2 Soil parameters analysis

In this section, the sensitivity of the wheel-soil contact model to soil parameter variations is analyzed. The sensitivity of drawbar pull and side force due to the parameter variations is simulated by means of TBM model.

A wheel on a sandy loam terrain is employed in this model analysis. The wheel's dimension are given in Table 2.2, while the parameters of sandy loam are given in Table 2.1 on page 32. The operating conditions are equal to those used in simulation performed in Chapter 2, and they are given in Table. 2.6.

The evaluation of the drawbar pull and side force sensitivity has been performed by changing one of the soil parameters while the other ones are maintained constant. The values of soil parameters that varies during the simulation are listed in Table 4.1.

Table 4.1: Soil parameter variations for model sensitivity analysis

Parameter [unit]	Description	Fixed value	Variation
n [-]	Sinkage exponent	0.7	[0.6; 0.8; 1; 1.2]
c [kPa]	Cohesion	1.7	[0.0; 1.5; 3.0; 4.5]
ϕ [deg]	Internal friction angle	29.0	[25.0; 30.0; 35.0; 40.0]
k_c [kN/m ^{$n+1$}]	Cohesive modulus	5.3	[0; 5; 10; 20]
k_ϕ [kN/m ^{$n+2$}]	Frictional modulus	1515.0	[900; 1200; 1600; 2000]
K [m]	Shear modulus	0.025	[0.01; 0.02; 0.03; 0.04]

4.2.1 Discussion and results

Sinkage exponent (n)

The sinkage exponent specify the soil soil-sinkage properties. A wheel on a terrain with the sinkage exponent less than 1.0 sinks relatively easy, while a larger sinkage exponent tends to inhibit the wheel sinkage.

As shown in Fig. 4.1, the drawbar pull decreases along with sinkage exponent increase, whereas the side force increases together with the sinkage exponent.

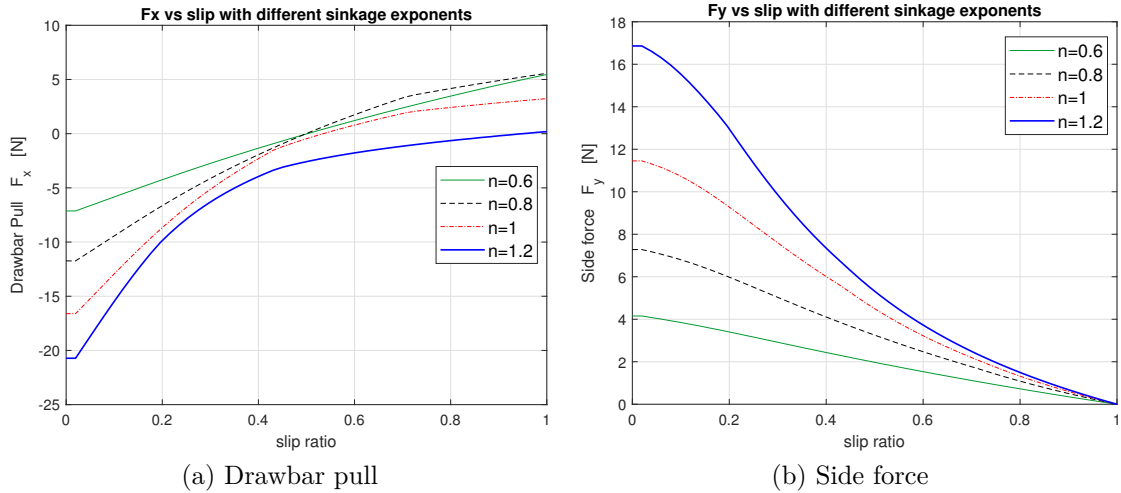


Figure 4.1: Model sensitivity to sinkage exponent (n)

Cohesion stress (c)

The results for cohesion stress are shown in Fig. 4.2. It can be seen that the drawbar pull increases as increasing cohesion stress. This is due to the fact that cohesion stress contributes to the shear stress as expressed in Eq. (2.20). Thus, the larger the cohesion stress is, the larger the drawbar pull becomes.

However, cohesion is relatively insensitive to drawbar pull, because increasing cohesion by a large margin will hardly change drawbar pull. On the other hand, by slightly varying the drawbar pull will greatly change the cohesion stress parameter value (Hutangkabodee [13]).

Even the side force increases as increasing cohesion stress. This is because the side force is a function of only lateral shear stress and thereby of cohesion stress, too.

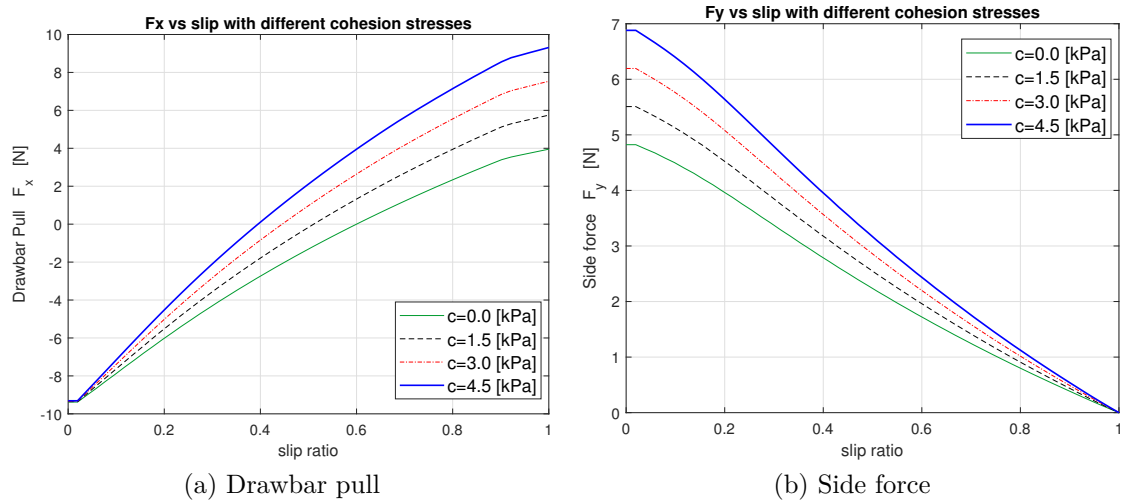


Figure 4.2: Model sensitivity to cohesion stress (c)

Internal friction angle (ϕ)

The friction angle results are shown in Fig. 4.3. Both drawbar pull and side force increase along with the friction angle. The behavior of forces is as expected, because the friction angle affects the shear stress as expressed in Eq. (2.20).

Pressure-sinkage moduli (k_c , k_ϕ)

The results for pressure-sinkage moduli are shown in Fig. 4.4 and Fig. 4.5.

As illustrated, the cohesive modulus does not significantly affect wheel forces.

Regarding to frictional modulus, larger k_ϕ is, the smaller the wheel forces become. This is because the normal stress is proportional to k_ϕ , therefore an increment

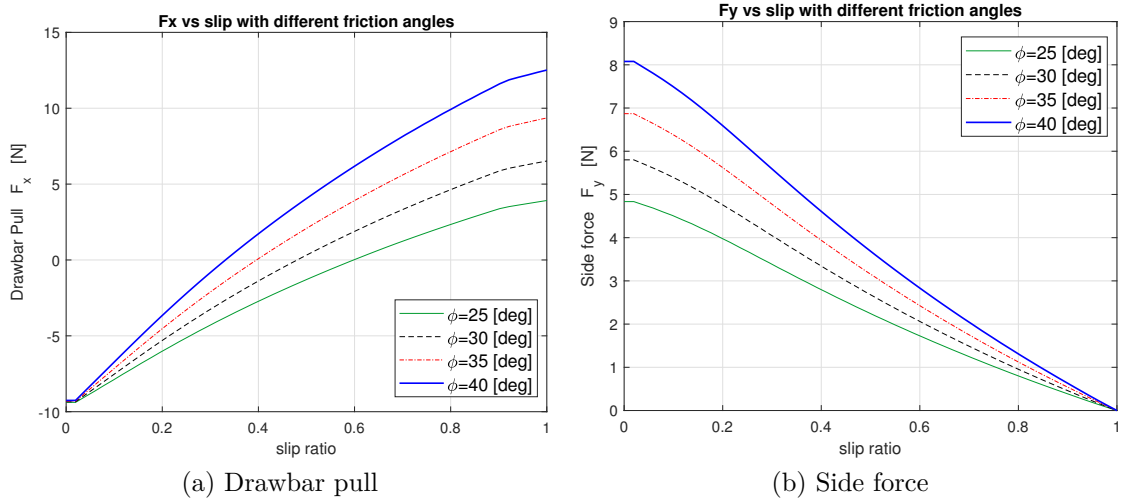


Figure 4.3: Model sensitivity to internal friction angle (ϕ)

of the frictional modulus will increase also the resistance force due to normal stress.

For the same reason, lateral force decreases when the frictional modulus increases.

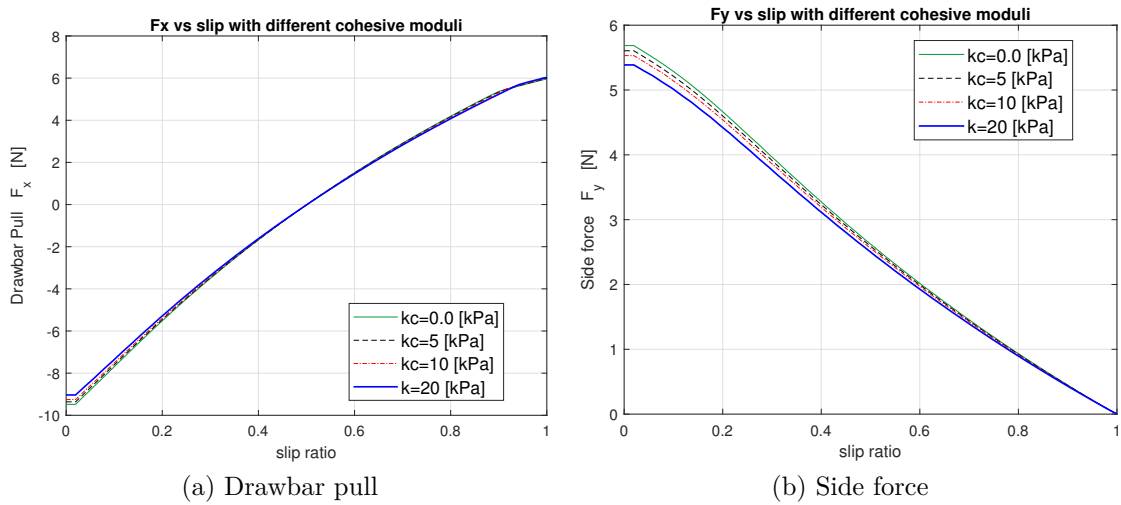


Figure 4.4: Model sensitivity to cohesive modulus (k_c)

Shear modulus (K)

As shown in Fig. 4.6, the model is very sensitive to the shear modulus variations.

Both wheel forces decrease when shear modulus increases. This is due to Eq. (2.20),

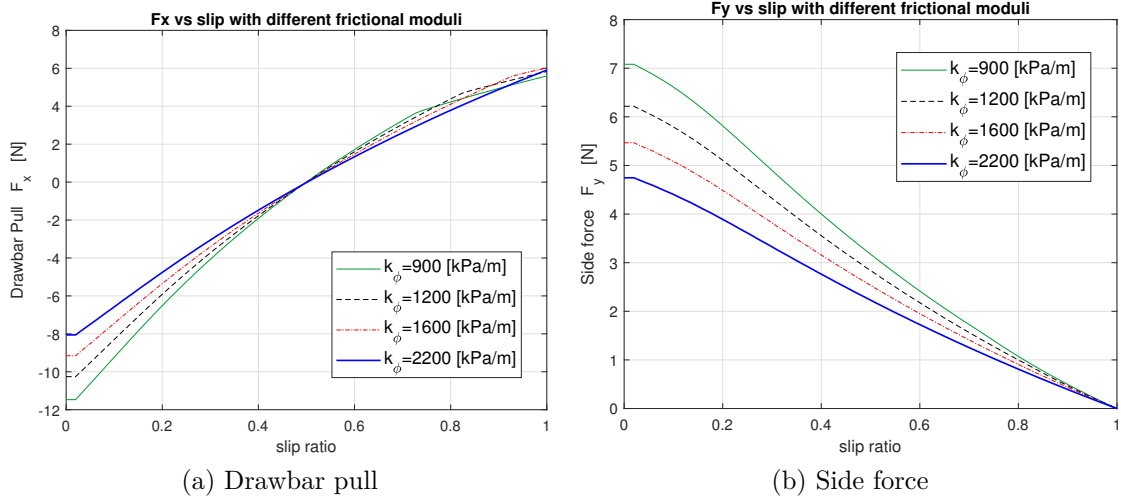


Figure 4.5: Model sensitivity to frictional modulus (K)

in fact by increasing K will decrease the shear stress. It can be seen that varying K may cause significant changes in drawbar pull and side force because the model is largely affected by this parameter.

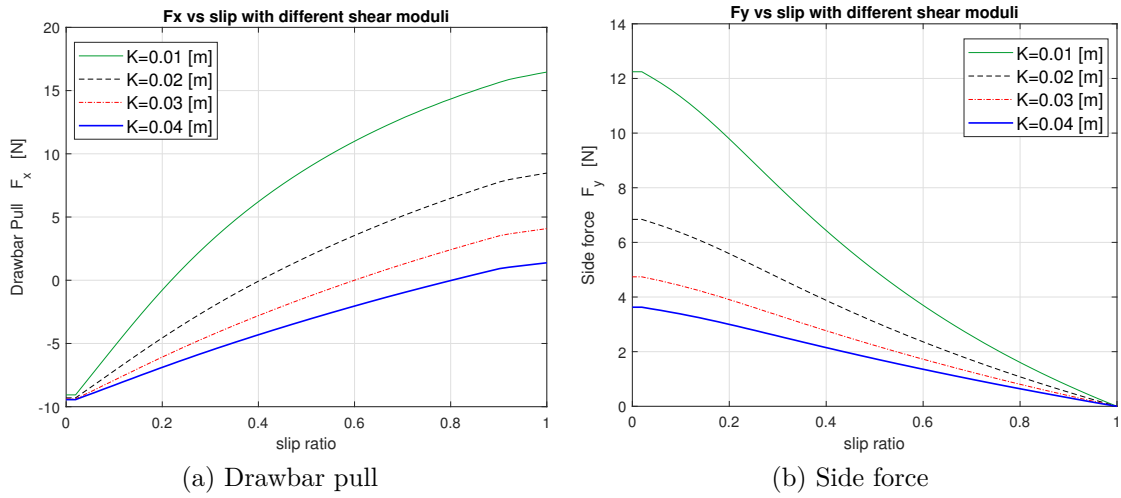


Figure 4.6: Model sensitivity to shear modulus (k_ϕ)

4.3 Identification algorithm

As discussed in section 4.1, the on-line identification of the soil parameters is crucial to predict the tractive force required on the wheels of the WMR operating on

unknown terrains.

To accomplish the identification is used a decoupled analytical wheel-soil interaction terramechanics model proposed by literature [4].

This method is able to identify unknown soil parameters by means of the data fitting method, so it must be assumed that there are available data measured by on-board sensors. In this case, it was not possible to acquire experimental measurements, therefore the identification process has been performed by using as input the simulated data obtained from the proposed TBM model.

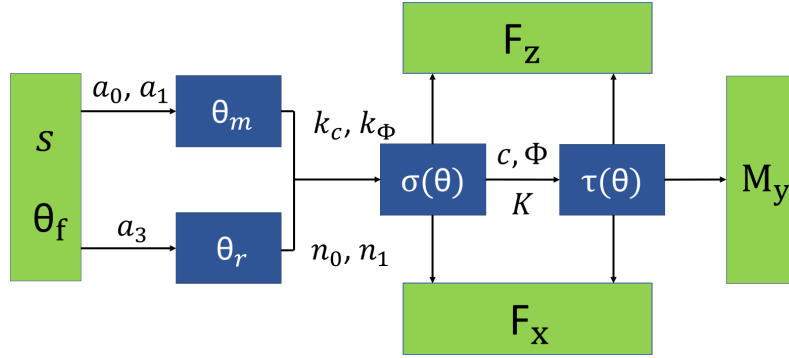


Figure 4.7: Diagram of coupled wheel-soil interaction model

By ignoring the lateral contribute owing to the side force generated during steering maneuvers, the wheel-soil interaction model can be resumed with three main equations used to calculate the drawbar pull, the vertical force and the resistance torque expressed in Eqs. (2.23), (2.31) and (2.34).

In Fig. 4.7 is shown the procedure to calculate F_x , F_z and M_y if the soil parameters values are available.

Conversely, it can be possible identifying the unknown soil parameters if values of F_x , F_z , M_y , s and θ_f are available.

However, the equations are highly coupled, and each of them contains all the unknown parameters. Thus, a simultaneous identification of all the soil parameters is infeasible.

In fact, because of the complexity and non-linearity of the model, the identification process can likely lead to local convergence.

Consequently, in order to make feasible the identification process of the unknown parameters, the equations must be decoupled by splitting up the variables into three groups declared as follows:

- $\mathbf{P}_I = \{a_0, a_1\}$: Soil parameters used to estimate the maximum stress angle according to Eq. (2.18).
- $\mathbf{P}_{II} = \{K_s, n_0, n_1\}$: K_s is the lumped pressure-sinkage coefficient, as expressed in Eq. 2.9, while n_0 and n_1 are parameters of the improved sinkage exponent N reformulated as linear function of slip: $N = n_0 + n_1 s$ (L. Ding [4]).

- $P_{III} = \{c, \phi, K\}$: Cohesion stress, internal friction angle and shear modulus.

In this manner, the parameters can be identified separately one group at a time, making feasible the identification process.

4.3.1 Stress simplification

In order to obtain decoupled equations, it is needed a closed-form solution; this can be achieved, firstly, by simplifying the model.

A linear approximation is used, and the literature [4, 14] has verified the linearized method for soils with a sinkage exponent in the range of 0.5 to 1.6.

Let define the maximum normal stress σ_m and the maximum shear stress τ_m :

$$\sigma_m = K_s r^N (\cos \theta_m - \cos \theta_f)^N \quad (4.1)$$

$$\tau_m = (c + \sigma_m \tan \phi) (1 - \exp\{-|r [(\theta_f - \theta_m) - (1 - s)(\sin \theta_f - \sin \theta_m)]|/K\}) \quad (4.2)$$

The normal and shear stresses can be approximated by means of the linearized method:

$$\hat{p}(\theta) = \begin{cases} p_m \frac{\theta_f - \theta}{\theta_f - \theta_m} & (\theta_m \leq \theta \leq \theta_f) \\ p_m \frac{\theta - \theta_r}{\theta_m - \theta_r} & (\theta_r \leq \theta < \theta_m) \end{cases} \quad (4.3)$$

where:

$$p = \sigma, \tau, \tau_t, \tau_l$$

Hence, a closed form solution, expressed in Eq. 4.4, can be obtained by substituting Eq. (4.3) with Eqs. (2.23), (2.31) and (2.34) and then integrating.

$$\begin{bmatrix} F_z \\ F_x \\ M_y \end{bmatrix} = \begin{bmatrix} A & B \\ -B & A \\ 0 & rC \end{bmatrix} \begin{bmatrix} X \\ Y \end{bmatrix} \quad (4.4)$$

where:

$$A = \frac{\cos \theta_m - \cos \theta_r}{\theta_m - \theta_r} + \frac{\cos \theta_m - \cos \theta_f}{\theta_f - \theta_m} \quad (4.5)$$

$$B = \frac{\sin \theta_m - \cos \theta_r}{\theta_m - \theta_r} + \frac{\sin \theta_m - \sin \theta_f}{\theta_f - \theta_m} \quad (4.6)$$

$$C = \frac{\theta_f - \theta_r}{2} \quad (4.7)$$

$$X = r b \sigma_m \quad (4.8)$$

$$Y = r b \tau_m \quad (4.9)$$

A , B and, C are functions of entrance angle θ_f and of \mathbf{P}_I parameters.

X is related to parameters of \mathbf{P}_I and \mathbf{P}_{II} groups, while Y is related to all three parameters groups.

4.3.2 Decoupling of equations

Finally, the decoupled analysis of equation can be accomplished. The strategy adopted is based on decoupling Eq. (4.4), knowing that F_x , F_z and M_y are functions of all the soil parameters.

According to Eq. (4.4), X and Y can be rearranged in this manner:

$$X = \frac{F_z - B Y}{A} = \frac{A Y - F_x}{B} \quad (4.10)$$

$$Y = \frac{M_y}{r C} \quad (4.11)$$

Thereafter, by substituting Eqs. (4.10) and (4.11) with Eq. (4.4), decoupled equations of drawbar pull and vertical force can be obtained as follows:

$$F_x = A Y - B \frac{F_z - B Y}{A} = \frac{A^2 + B^2}{r A C} M_y - \frac{B}{A} F_z \quad (4.12)$$

$$F_z = \frac{A X + B M_y}{r C} = r B A \sigma_m + \frac{B M_y}{r C} \quad (4.13)$$

Maximum normal stress σ_m can be rewritten according to Eq. (4.13) as follows:

$$\sigma_m = \frac{F_z}{r b A} - \frac{B M_y}{r^2 b A C} \quad (4.14)$$

Let define D as:

$$D = 1 - \exp\{-|r[(\theta_f - \theta_m) - (1 - s)(\sin \theta_f - \sin \theta_m)]|/K\} \quad (4.15)$$

Then, by substituting Eqs. (4.9), (4.14) and (4.15) in Eq. (4.4), the decoupled equation of resistance torque can be finally obtained as:

$$M_y = r^2 C D \frac{b c + \frac{F_z \tan \phi}{r A}}{1 + \frac{r B D \tan \phi}{r A}} \quad (4.16)$$

Notice that, from Eq. 4.12, F_x is function of the parameters in \mathbf{P}_I , F_z is function of the parameters in \mathbf{P}_I and \mathbf{P}_{II} , while M_y is function of the parameters in \mathbf{P}_I and \mathbf{P}_{III} .

4.3.3 Identification method

Identifying a_0 and a_1

The first parameters to be identified are a_0 and a_1 used to estimate θ_m as function of slip.

According to Eq. 4.12, the drawbar pull is function of M_y , F_z , θ_f , s and the unknown parameters of group \mathbf{P}_I .

In order to calculate the drawbar pull, the decoupled equation that is function of entry angle θ_f , slip ratio s , vertical force F_z and torque M_y must be acquired as input.

Therefore, the two unknown parameters can be identified if the other ones have been measured or, like in this case, simulated.

In Fig. 4.8 is shown the procedure to perform the first identification by using the decoupled Eq. 4.12.

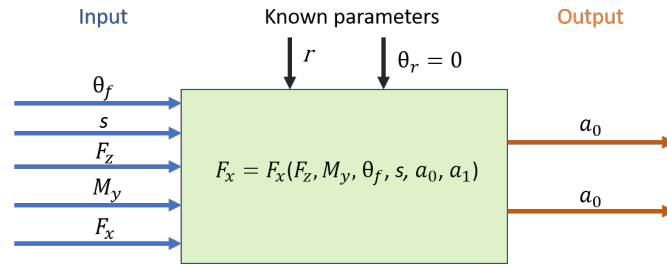


Figure 4.8: Identification diagram of a_0 , a_1

Identifying K_s , n_0 and n_1

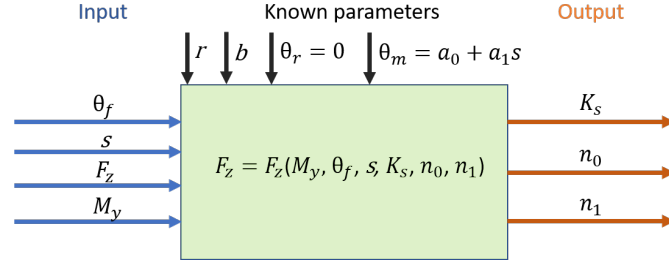
Once a_0 and a_1 have been identified, they can be used to perform the second identification step by applying Eq. (4.17) as shown in Fig. 4.9.

According to Eqs. (4.1) and (4.13), the explicit form of the vertical force decoupled equation is expressed as:

$$F_z = r b A [K_s r^{(n_0+n_1 s)} (\cos \theta_m - \cos \theta_f)^{(n_0+n_1 s)}] + \frac{B}{r C} M_y \quad (4.17)$$

In this case, the parameters to be identified are K_s , n_0 and n_1 .

Although the model uses during the simulation the constant value of sinkage exponent given in Table 2.1, the parameters n_0 and n_1 are referred to the improved sinkage exponent N . This value takes into account the dynamic sinkage variation due to wheel slip and then give more accurately results respect than the constant one.

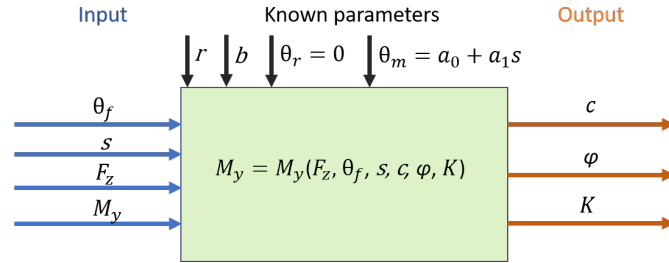

 Figure 4.9: Identification diagram of K_s , n_0 , n_1

Identifying c , ϕ and K

The parameters of third group are identified by means of the procedure shown in Fig 4.10.

By substituting the values of D in Eq. 4.16, the explicit decoupled equation is obtained as:

$$M_y = \frac{r^2 C (b c + F_z \frac{\tan \phi}{r A}) (1 - \exp\{-|r[(\theta_f - \theta_m) - (1 - s)(\sin \theta_f - \sin \theta_m)]|/K\})}{1 + (\frac{r B \tan \phi}{r A}) (1 - \exp\{-|r[(\theta_f - \theta_m) - (1 - s)(\sin \theta_f - \sin \theta_m)]|/K\})} \quad (4.18)$$


 Figure 4.10: Identification diagram of c , ϕ , K

In the third identification problem, by using the decoupled Eq. (4.18), cohesion stress, internal friction angle and shear modulus are identified by providing θ_f , s , F_z and M_y as input and in addition by knowing in advance the parameters of group P_I .

4.3.4 Implementation of identification algorithm

The implementation of soil parameters identification takes place by means of least square method.

The *lsqcurvefit()* MATLAB function has been used to solve the non-linear model.

The non-linear least-squares solver finds coefficients x that solve the problem:

$$\min_x \frac{1}{2} \|F(x, xdata) - ydata\|^2 = \frac{1}{2} \sum_{i=1}^m [F(x, xdata_i) - ydata_i]^2 \quad (4.19)$$

where x denotes the vector of identified parameters, while $xdata$ are the input data, $ydata$ are the output data, m denotes the length of $xdata$ and $ydata$, and F denotes the decoupled function expressed in Eqs. (4.12), (4.17) and (4.18).

Chapter 5

Identification results

5.1 Introduction

In this chapter the soil parameters identification has been performed and a discussion of the results has been also addressed.

The identification process has been carried out by using as data sets the time-series arrays obtained from simulations of the TBM model.

The data acquired from simulations have been processed for three types of soil (sandy loam, dry sand and clayey soil) and for two kind of wheel.

The soil type parameters are given in Table 2.1 on page 32, while the sizes of the chosen wheels are given in Table 5.1.

While, the operating conditions used for the wheel-soil interaction simulation are summarized in Table 5.2.

Table 5.1: Parameters of wheels

Wheel type	Radius (r)	Width (b)
Wheel-A	0.092	0.107
Wheel-B	0.135	0.165

The values of entrance angle θ_f are obtained from the numerical method as described in Section 2.6.1.

In case of the values are measured from experiments, θ_f can be obtained by visual means or by mounting a F/T sensor along the wheel axle with a slip ring developed by J. Guo, L. Ding and L. Guangjun [9]. Otherwise, the wheel sinkage h_f can be measured by a high precision sliding resistance displacement sensor [4] and then θ_f can be calculated.

The vertical load F_z is also obtained as a result of numerical iteration.

The torque M_y is calculated from the wheel-soil interaction model, while, in case

Table 5.2: Parameters used for simulation

Parameter [unit]	Description	Value
W [kg]	Wheel normal load	6
s [-]	Slip ratio	0 to 1
β [deg]	Slip angle	0
θ_r [deg]	Exit angle	0
θ_m [deg]	Maximum normal stress angle	$(a_0 + a_1 s) \theta_f$
a_0 [-]	Coefficient for θ_m	0.2
a_1 [-]	Coefficient for θ_m	0.3
j_{max1} [m]	Sandy loam/dry sand shear deformation limit	0.020
j_{max2} [m]	Clayey soil shear deformation limit	0.009

of experimental measurements can be estimated by reference to the current of the wheel motor.

The wheel angular speed ω can be estimated using Eq. (2.1), using the slip ratio as input of TBM model. Otherwise, it can be measured with an encoder.

The wheel longitudinal velocity v_x is calculated from the wheel-soil interaction model block. While during experiments it can be measured from inertial measurement units (IMU) or visual odometry.

The drawbar pull F_x , in case of simulation, is calculated also with wheel-soil interaction model. Otherwise in real world experiments can be measured by installing a force sensor on the wheel.

5.2 Fitting graphs and errors

The graphs in this section show the fitting results of identification process.

The values of $\tilde{y}data_i$ are obtained as the sum of the output data $ydata_i$ acquired from the TBM model and the normally distributed random noise as expressed here below:

$$\tilde{y}data_i = ydata_i + e \quad (5.1)$$

where e is the error noise used to simulate the instrument error when data are acquired with experimental measurements.

As shown in below graphs, the output values obtained by simulations and corrupted by noise are indicated with the continuous blue line, while the values obtained by fitting process are illustrated with the dashed red line.

In Figs. 5.1 and 5.2 are shown the three steps of the soil parameters identification for sandy loam terrain by using wheel-A and wheel-B.

The initial guess and the bound limits of the parameters used during the decoupled fitting process are shown here below:

- $P_I : P_0 = [0.01 \ 0.03]$; no bounds delimiter.
- $P_{II} : P_0 = [1400 \ 0.1 \ 0]$; $P_{lb} = [300 \ 0.01 \ -0.5]$; $P_{ub} = [5000 \ 1.5 \ 1]$.
- $P_{III} : P_0 = [3.5 \ 23 \ 0.2]$; $P_{lb} = [0.3 \ 10 \ 0.001]$; $P_{ub} = [5 \ 58 \ 0.5]$.

In Fig. 5.3 and 5.4 are shown the three steps of the soil parameters identification for dry sand terrain by using wheel-A and wheel-B.

The initial guess and the bound limits of the parameters used during the decoupled fitting process are shown here below:

- $P_I : P_0 = [0.01 \ 0.03]$; no bounds delimiter.
- $P_{II} : P_0 = [1500 \ 0.3 \ 0.1]$; $P_{lb} = [300 \ 0.01 \ -0.5]$; $P_{ub} = [5000 \ 1.5 \ 1]$.
- $P_{III} : P_0 = [3.5 \ 28 \ 0.2]$; $P_{lb} = [0.2 \ 10 \ 0.001]$; $P_{ub} = [5 \ 58 \ 0.5]$.

In Fig. 5.5 and 5.6 are shown the three steps of the soil parameters identification for clayey soil terrain by using wheel-A and wheel-B.

The initial guess and the bound limits of the parameters used during the decoupled fitting process are shown here below:

- $P_I : P_0 = [0.01 \ 0.03]$; no bounds delimiter.
- $P_{II} : P_0 = [900 \ 0.1 \ 0.01]$; $P_{lb} = [300 \ 0.01 \ -0.5]$; $P_{ub} = [5000 \ 1.5 \ 1]$.
- $P_{III} : P_0 = [3.5 \ 16 \ 0.04]$; $P_{lb} = [1 \ 7 \ 0.001]$; $P_{ub} = [6.5 \ 45 \ 0.5]$.

In Tables 5.3 and 5.4 are given the results of the identified parameters obtained for both wheels used in simulations.

Table 5.3: Identified soil parameters for wheel-A

Soil parameters	Wheel-A		
	Sandy loam	Dry sand	Clayey soil
a_0	0.2813	0.2390	0.2907
a_1	0.2116	0.2589	0.2131
K_s [kPa/m ^N]	1400.2	1378.9	879.467
n_0	0.6235	0.047	0.356
n_1	0.0214	0.015	0.0295
c [kPa]	2.1	1.35	3.5
ϕ [deg]	30.2	26.7	17.6
K [m]	0.03	0.0187	0.014

Table 5.4: Identified soil parameters for wheel-B

Soil parameters	Wheel-B		
	Sandy loam	Dry sand	Clayey soil
a_0	0.2576	0.2442	0.2850
a_1	0.2571	0.2461	0.2129
K_s [kPa/m ^N]	1711.7	1508.9	816.8425
n_0	0.6657	0.047	0.4519
n_1	0.0133	0.015	0.0124
c [kPa]	2.05	0.874	9.42
ϕ [deg]	35.7	27.6	14.1
K [m]	0.028	0.034	0.0169

By comparing the identified values with the soil parameters values used for simulations and given in Table 2.1 on page 32, it is possible to evaluate the identification quality of the results.

Notice that the largest error for the identified ϕ is 6.7deg when wheel-B travel on sandy loam.

The largest error of c is 5.28 kPa, when wheel-B travel on clayey soil. But, as mentioned in section 4.2, cohesion stress does not greatly affect the traction, therefore this error results small compared to the shearing stress.

The maximum error of the parameter K is around 0.09 m when wheel-B travel on dry sand. This error is small enough to say that the identification of shear deformation gives acceptable results.

The parameter K_s is sensitive to the guess value used during the identification process and the identified results are quite close to the preset initial values.

This means that only n_0 and n_1 are sufficient for fitting the vertical load. Thus, K_s could be keep fixed to the value of estimated soil frictional modulus k_ϕ , as k_c can be neglected because is too small respect than k_ϕ [4].

The range of ($N = n_0 + n_1 s$) is well matched for each soil by the identified values.

Parameters a_0 and a_1 are quite close to the target ones specified in Table 5.2.

However, during the identification procedure the other parameters are not greatly influenced by their values.

This means that wheel-soil interaction mechanics is not sensitive to a_0 and a_1 . Therefore, it can be possible to assign them typical values of a_0 and a_1 to the soil even if the values of F_x are unknown.

In Tables 5.5 and 5.6 are given the squared norms of the residual values and they are used to evaluate the goodness of fit of the identification process.

As shown in Table 5.6, the maximum error occurs for the estimated drawbar pull

during the motion of wheel-B on the dry sand soil. Anyway, the error is expressed in Newton, this means that the predicted F_x has inaccuracies around 0.4 N at most, which are acceptable results for the traction prediction.

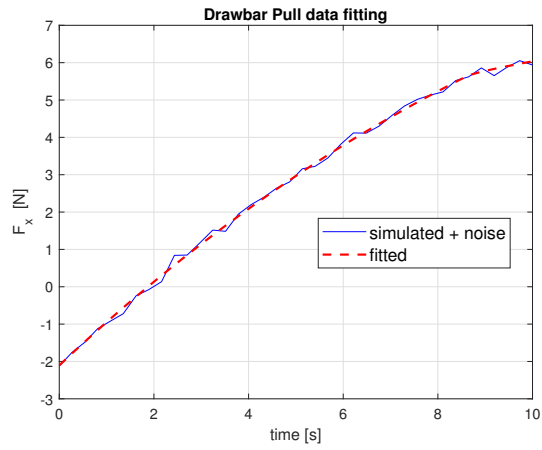
Finally, as shown in graphs and then as confirmed by the obtained values, it is possible to affirm that the forces/torques estimation algorithm provides satisfactory performance and the obtained identified parameters values are quite close to the expected ones.

Table 5.5: Squared norm of the residual for wheel-A

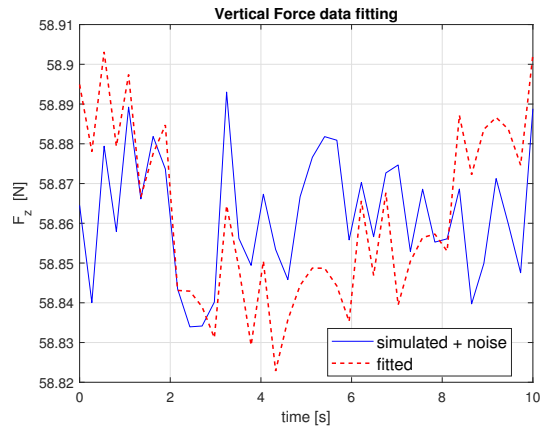
Fit results	Wheel-A		
	Sandy loam	Dry sand	Clayey soil
F_x [N]	0.3371	0.2859	0.3162
F_z [N]	0.2719	0.0891	0.1220
M_y [N]	0.0114	0.0143	0.0036

Table 5.6: Squared norm of the residual for wheel-B

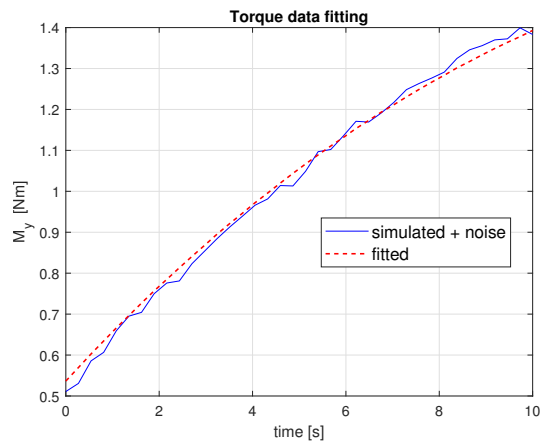
Fit results	Wheel-B		
	Sandy loam	Dry sand	Clayey soil
F_x [N]	0.3733	0.4643	0.2341
F_z [N]	0.0272	0.1710	0.1494
M_y [N]	0.0975	0.0567	0.0029



(a) Drawbar pull

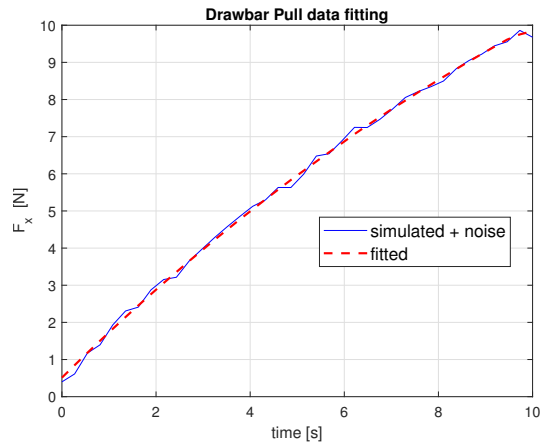


(b) Vertical force

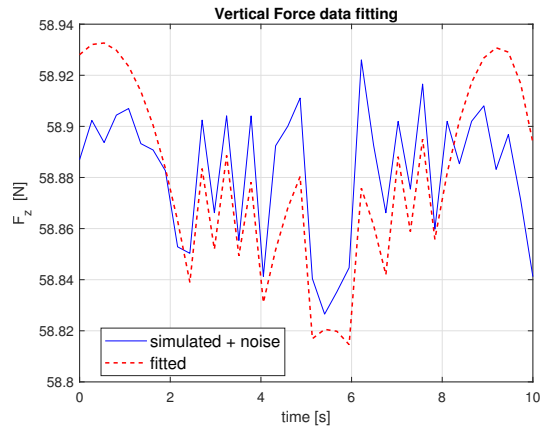


(c) Torque

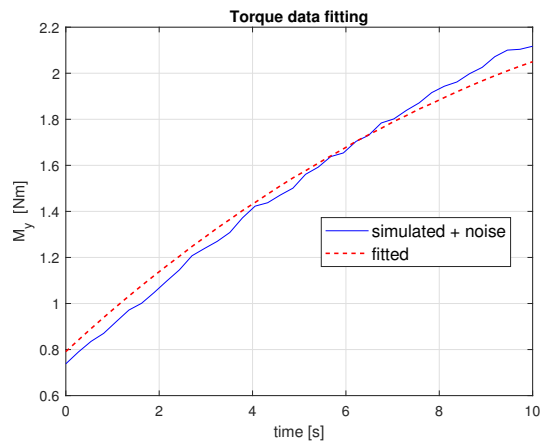
Figure 5.1: Fitting graphs for wheel-A on sandy loam



(a) Drawbar pull

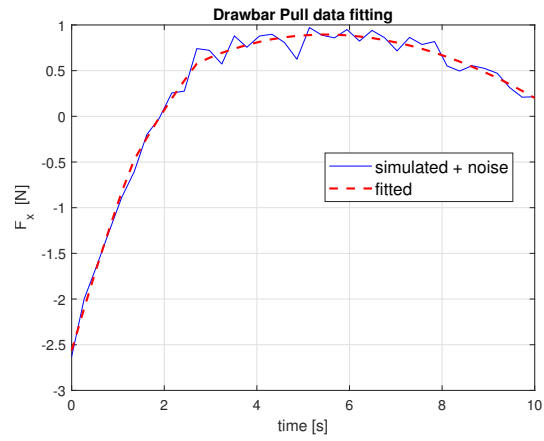


(b) Vertical force

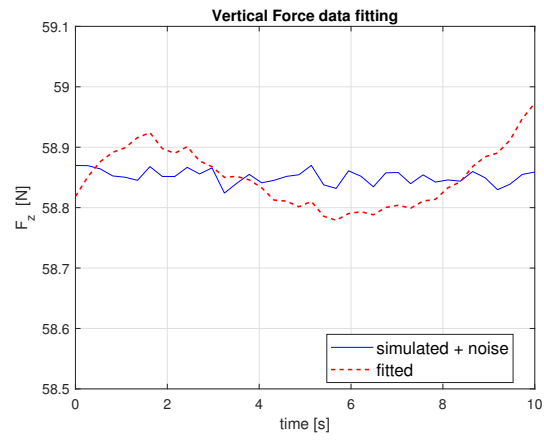


(c) Torque

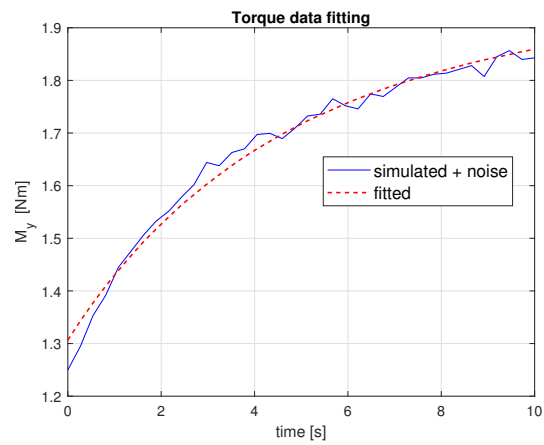
Figure 5.2: Fitting graphs for wheel-B on sandy loam



(a) Drawbar pull

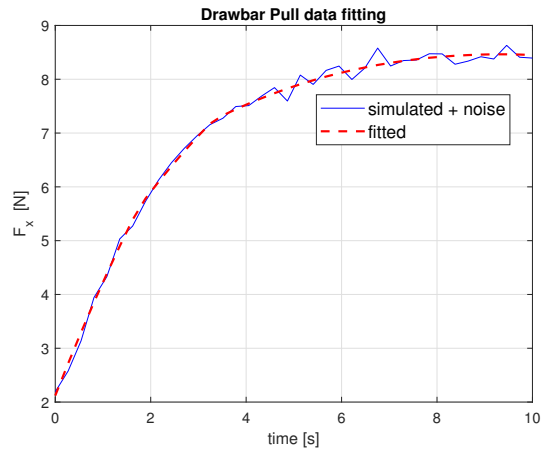


(b) Vertical force

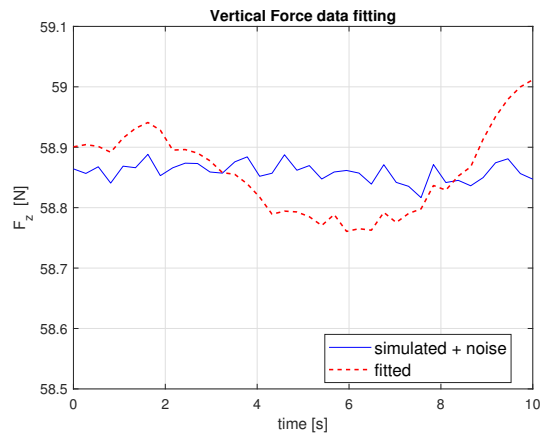


(c) Torque

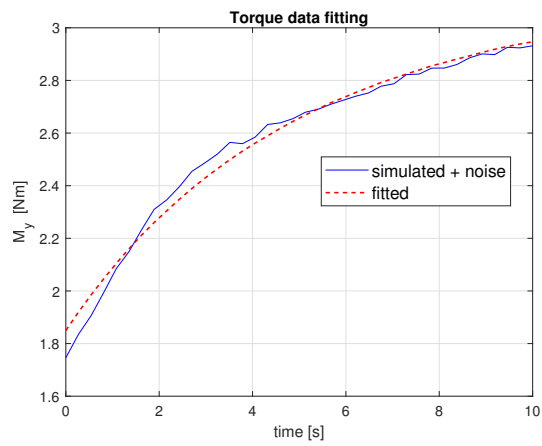
Figure 5.3: Fitting graphs for wheel-A on dry sand



(a) Drawbar pull

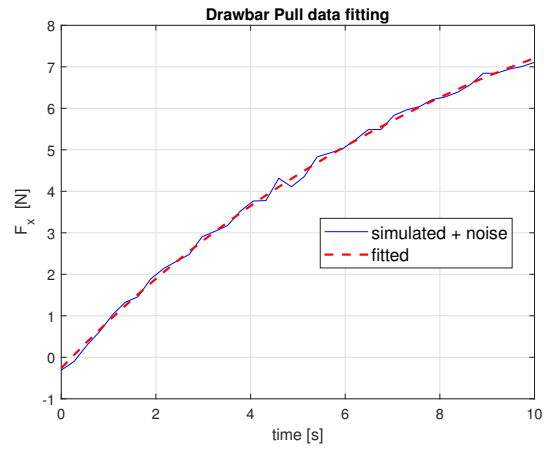


(b) Vertical force

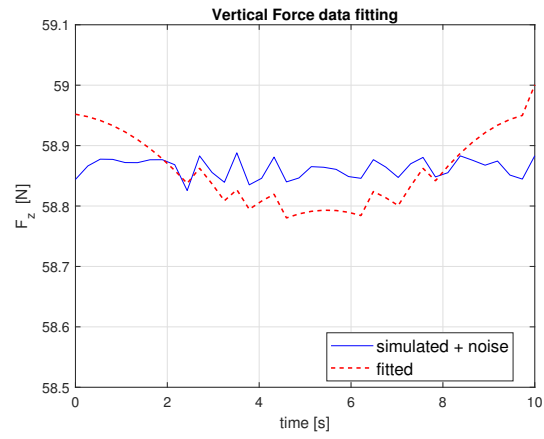


(c) Torque

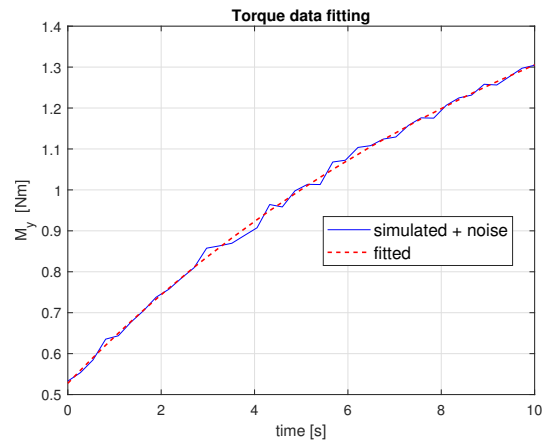
Figure 5.4: Fitting graphs for wheel-B on dry sand



(a) Drawbar pull

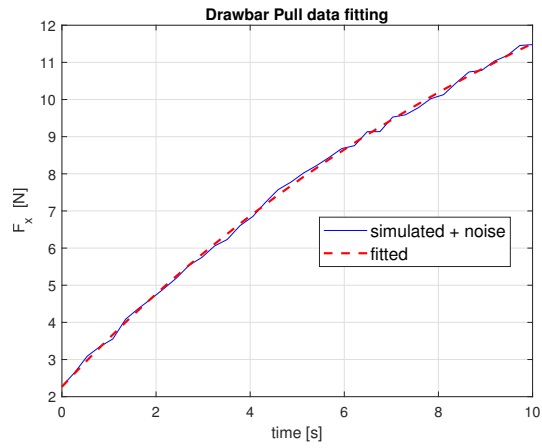


(b) Vertical force

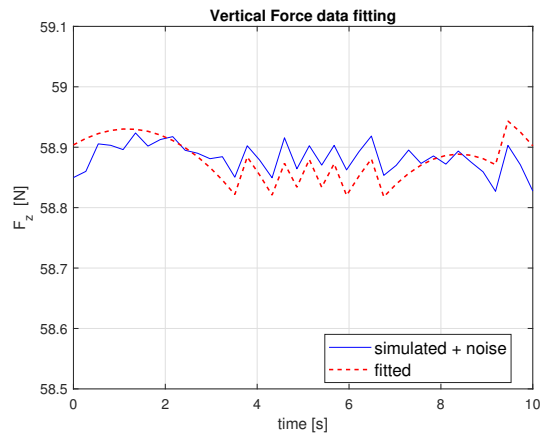


(c) Torque

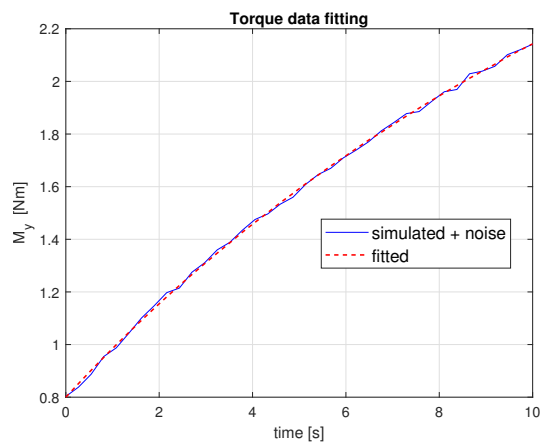
Figure 5.5: Fitting graphs for wheel-A on clayey soil



(a) Drawbar pull



(b) Vertical force



(c) Torque

Figure 5.6: Fitting graphs for wheel-B on clayey soil

Chapter 6

Conclusion

The prediction of wheel-soil interaction mechanics by means of the identified parameters can be applied to wheeled mobile robot design, control strategy optimization, and dynamics simulation

The algorithm provides satisfactory performance and the computational time for fitting drawbar pull, vertical force and torque is very short, mean value around 50-100 ms, as confirmed by literature [4].

Therefore, it can be concluded that this method is suitable for on-line identification of parameters of unknown agricultural terrains.

The thesis revolves around the development of a wheel-soil interaction model based on terramechanics theory, which is able to make up for those investigations where field experimental data are not available.

Nevertheless, the wheel-soil interaction model, used to provide simulated data for parameter identification, must be compared with experimental results. The measured data can be acquired by using a wheel-soil interaction test bed consisting of a experimental wheel traveling on a simulant soil with already well known soil parameters.

The obtained results also suggest that the soil parameters measurements based on the decoupled analysis of the wheel-soil interaction mechanics should be combined with new kind of identification methods, for example, by using neural networks or by visual means to quickly obtain the convergence of the identified parameters without the need of initial guess.

Future work will deal with optimal control algorithms based on the online recognition of soil parameters.

Bibliography

- [1] *Agriculture Robots Market report explored in latest research*. 2019. URL: <https://www.whatech.com/markets-research/agriculture/569108-agriculture-robots-market-demand-for-automating-routine-and-specialized-farming-tasks-bolster-uptake> (visited on 02/11/2020).
- [2] Mieczyslaw Gregory Bekker. *Introduction to terrain-vehicle systems. part i: The terrain. part ii: The vehicle*. Tech. rep. MICHIGAN UNIV ANN ARBOR, 1969.
- [3] Mieczyslaw Gregory Bekker. “Theory of land locomotion”. In: (1956).
- [4] L. Ding et al. “Parameter identification for planetary soil based on a decoupled analytical wheel-soil interaction terramechanics model”. In: *2009 IEEE/RSJ International Conference on Intelligent Robots and Systems*. 2009, pp. 4122–4127.
- [5] Liang Ding et al. “Improved explicit-form equations for estimating dynamic wheel sinkage and compaction resistance on deformable terrain”. In: *Mechanism and Machine Theory* 86 (2015), pp. 235–264. ISSN: 0094-114X. DOI: <https://doi.org/10.1016/j.mechmachtheory.2014.12.011>. URL: <http://www.sciencedirect.com/science/article/pii/S0094114X14003243>.
- [6] Liang Ding et al. “Planetary rovers’ wheel–soil interaction mechanics: new challenges and applications for wheeled mobile robots”. In: *Intelligent Service Robotics* 4.1 (2011), pp. 17–38.
- [7] Liang Ding et al. “Terramechanics-based high-fidelity dynamics simulation for wheeled mobile robot on deformable rough terrain”. In: *2010 IEEE International Conference on Robotics and Automation*. IEEE. 2010, pp. 4922–4927.
- [8] Liang Ding et al. “Terramechanics-based modeling of sinkage and moment for in-situ steering wheels of mobile robots on deformable terrain”. In: *Mechanism and Machine Theory* 116 (2017), pp. 14–33. ISSN: 0094-114X. DOI: <https://doi.org/10.1016/j.mechmachtheory.2017.05.011>. URL: <http://www.sciencedirect.com/science/article/pii/S0094114X16302968>.

- [9] J. Guo et al. “An Apparatus to Measure Wheel–Soil Interactions on Sandy Terrains”. In: *IEEE/ASME Transactions on Mechatronics* 23.1 (2018), pp. 352–363. DOI: [10.1109/TMECH.2018.2790986](https://doi.org/10.1109/TMECH.2018.2790986).
- [10] Junlong Guo et al. “Longitudinal skid model for wheels of planetary rovers based on improved wheel sinkage considering soil bulldozing effect”. In: *Journal of Terramechanics* 74 (2017), pp. 45–56. ISSN: 0022-4898. DOI: <https://doi.org/10.1016/j.jterra.2017.10.004>. URL: <http://www.sciencedirect.com/science/article/pii/S0022489816301148>.
- [11] E. Hegedus. *A Simplified Method for the Determination of Bulldozing Resistance*. Ordnance Tank Automotive Command, Research Division, Research and Engineering Directorate, Detroit Arsenal, Land Locomotion Laboratory Report. U.S. Army Ordnance Tank–Automotive Command, 1960. URL: <https://books.google.it/books?id=EEZqGwAACAAJ>.
- [12] T. Hertz. 2019. URL: <https://www.ers.usda.gov/topics/farm-economy/farm-labor> (visited on 02/11/2020).
- [13] Suksun Hutangkabodee et al. “Model-Based Soil Parameter Identification for Wheel-Terrain Interaction Dynamics”. In: *IFAC Proceedings Volumes* 40.20 (2007), pp. 578–583.
- [14] K. Iagnemma, H. Shibly, and S. Dubowsky. “On-line terrain parameter estimation for planetary rovers”. In: *Proceedings 2002 IEEE International Conference on Robotics and Automation (Cat. No.02CH37292)*. Vol. 3. 2002, 3142–3147 vol.3. DOI: [10.1109/ROBOT.2002.1013710](https://doi.org/10.1109/ROBOT.2002.1013710).
- [15] Genya Ishigami. “Terramechanics-based analysis and control for lunar/planetary exploration robots”. PhD thesis. 2008.
- [16] Genya Ishigami and Kazuya Yoshida. “Steering characteristics of an exploration rover on loose soil based on all-wheel dynamics model”. In: *2005 IEEE/RSJ International Conference on Intelligent Robots and Systems*. IEEE. 2005, pp. 3099–3104.
- [17] Z. Janosi, B. Hanamoto, and Istituto elettrotecnico nazionale Galileo Ferraris. “The analytical determination of drawbar pull as a function of slip for tracked vehicles in deformable soils”. In: 1961.
- [18] Zhenzhong Jia, William Smith, and Huei Peng. “Fast analytical models of wheeled locomotion in deformable terrain for mobile robots”. In: *Robotica* 31.1 (2013), pp. 35–53.
- [19] Zhenzhong Jia, William Smith, and Huei Peng. “Terramechanics-based wheel–terrain interaction model and its applications to off-road wheeled mobile robots”. In: *Robotica* 30 (May 2012). DOI: [10.1017/S0263574711000798](https://doi.org/10.1017/S0263574711000798).

-
- [20] JJ. *MAE and RMSE — Which Metric is Better?* Mar. 23, 2016. URL: <https://medium.com/human-in-a-machine-world/mae-and-rmse-which-metric-is-better-e60ac3bde13d> (visited on 11/20/2020).
- [21] Steven Dubowsky Karl Iagnemma. *Mobile Robots in Rough Terrain*. 2004.
- [22] “Prediction of wheel performance based on the analysis of soil-wheel stresses. Part I. Performance of driven rigid wheels: J. Wong and A. R. Reece. *J. Terramechanics*, 4, (1), 81 (1967)”. In: *Journal of Terramechanics* 4.2 (1967), p. 80. ISSN: 0022-4898. DOI: [https://doi.org/10.1016/0022-4898\(67\)90080-8](https://doi.org/10.1016/0022-4898(67)90080-8). URL: <http://www.sciencedirect.com/science/article/pii/S0022489867900808>.
- [23] Giulio Reina, Matilde Paiano, and Jose-Luis Blanco-Claraco. “Vehicle parameter estimation using a model-based estimator”. In: *Mechanical Systems and Signal Processing* 87 (2017), pp. 227–241.
- [24] William Smith et al. “Comparison of discrete element method and traditional modeling methods for steady-state wheel-terrain interaction of small vehicles”. In: *Journal of Terramechanics* 56 (2014), pp. 61–75.
- [25] Idris Idris Sunusi et al. “Intelligent tractors: Review of online traction control process”. In: *Computers and Electronics in Agriculture* 170 (Mar. 2020), p. 105176. DOI: [10.1016/j.compag.2019.105176](https://doi.org/10.1016/j.compag.2019.105176).
- [26] Wikipedia. *Multibody system — Wikipedia, the free encyclopedia*. [Online; visited on 27-november-2020]. 2020. URL: https://en.wikipedia.org/wiki/Multibody_system.
- [27] J.Y. Wong. “Chapter 2 - Modelling of Terrain Behaviour”. In: *Terramechanics and Off-Road Vehicle Engineering (Second Edition)*. Ed. by J.Y. Wong. Second Edition. Oxford: Butterworth-Heinemann, 2010, pp. 21–63. ISBN: 978-0-7506-8561-0. DOI: <https://doi.org/10.1016/B978-0-7506-8561-0.00002-6>. URL: <http://www.sciencedirect.com/science/article/pii/B9780750685610000026>.
- [28] J.Y. Wong. “Chapter 3 - Measurement of Terrain Properties”. In: *Terramechanics and Off-Road Vehicle Engineering (Second Edition)*. Ed. by J.Y. Wong. Second Edition. Oxford: Butterworth-Heinemann, 2010, pp. 65–74. ISBN: 978-0-7506-8561-0. DOI: <https://doi.org/10.1016/B978-0-7506-8561-0.00003-8>. URL: <http://www.sciencedirect.com/science/article/pii/B9780750685610000038>.
- [29] Jo Yung Wong. *Theory of ground vehicles*. John Wiley and Sons, 2008.